Cell

IRGQ-mediated autophagy in MHC class I quality control promotes tumor immune evasion

Graphical abstract

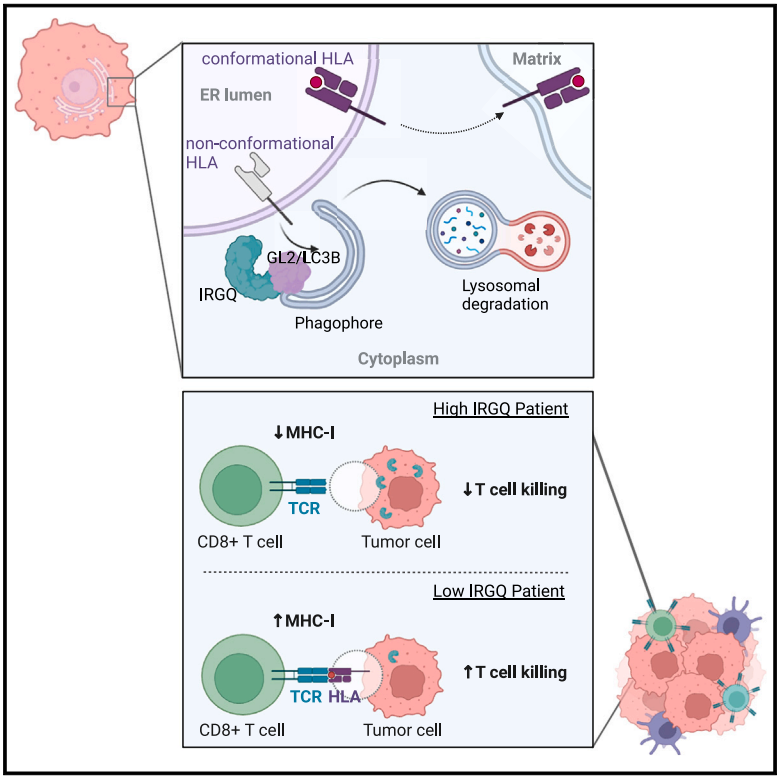

Highlights

- IRGQ is identified as a novel autophagy receptor
- Structures of IRGQ in complex with GABARAPL2 or LC3B show distinct binding modes
- IRGQ acts in the quality control of misfolded MHC class I to degrade it through autophagy
- IRGQ impacts CD8+ T cell immunity in human and murine hepatocellular carcinoma

Authors

Lina Herhaus, Uxía Gestal-Mato, Vinay V. Eapen, ..., J. Wade Harper, Joseph D. Mancias, Ivan Dikic

Correspondence

lina.herhaus@gmail.com (L.H.), dikic@biochem2.uni-frankfurt.de (I.D.)

In brief

IRGQ acts in the quality control of MHC class I molecules through autophagy, mediating tumor immune evasion.

Herhaus et al., 2024, Cell *187*, 7285–7302
December 12, 2024
https://doi.org/10.1016/j.cell.2024.09.048

CellPress

Cell

CellPress
OPEN ACCESS

Article

IRGQ-mediated autophagy in MHC class I quality control promotes tumor immune evasion

Lina Herhaus,[1,9,10,*] Uxía Gestal-Mato,[1,9] Vinay V. Eapen,[2,3] Igor Mačinković,[1,4] Henry J. Bailey,[1,5] Cristian Prieto-Garcia,[1] Mohit Misra,[1,5] Anne-Claire Jacomin,[1] Aparna Viswanathan Ammanath,[1] Ivan Bagarić,[1] Jolina Michaelis,[1] Joshua Vollrath,[1,5,6] Ramachandra M. Bhaskara,[1,5] Georg Bündgen,[7] Adriana Covarrubias-Pinto,[1] Koraljka Husnjak,[1] Jonathan Zöller,[6] Ajami Gikandi,[2] Sara Ribičić,[1] Tobias Bopp,[7] Gerbrand J. van der Heden van Noort,[8] Julian D. Langer,[6] Andreas Weigert,[4] J. Wade Harper,[3] Joseph D. Mancias,[2] and Ivan Dikic[1,5,6,10,11,*]

[1]Institute of Biochemistry II, Goethe University Frankfurt, Medical Faculty, Theodor-Stern-Kai 7, 60590 Frankfurt am Main, Germany
[2]Division of Radiation and Genome Stability, Department of Radiation Oncology, Dana-Farber Cancer Institute, Harvard Institutes of Medicine, 450 Brookline Avenue, Boston, MA 02215, USA
[3]Department of Cell Biology, Harvard Medical School, 240 Longwood Avenue, Boston, MA 02115, USA
[4]Institute of Biochemistry I, Goethe University School of Medicine, Theodor-Stern-Kai 7, 60590 Frankfurt am Main, Germany
[5]Buchmann Institute for Molecular Life Sciences, Goethe University Frankfurt, Riedberg Campus, Max-von-Laue-Straße 15, 60438 Frankfurt am Main, Germany
[6]Max Planck Institute of Biophysics, Goethe University Frankfurt, Riedberg Campus, 60438 Frankfurt am Main, Germany
[7]Institute for Immunology, University Medical Center, Johannes Gutenberg University Mainz, Mainz, Germany
[8]Department of Cell and Chemical Biology, Leiden University Medical Center, Leiden, the Netherlands
[9]These authors contributed equally
[10]Senior author
[11]Lead contact
*Correspondence: lina.herhaus@gmail.com (L.H.), dikic@biochem2.uni-frankfurt.de (I.D.)
https://doi.org/10.1016/j.cell.2024.09.048

SUMMARY

The autophagy-lysosome system directs the degradation of a wide variety of cargo and is also involved in tumor progression. Here, we show that the immunity-related GTPase family Q protein (IRGQ), an uncharacterized protein to date, acts in the quality control of major histocompatibility complex class I (MHC class I) molecules. IRGQ directs misfolded MHC class I toward lysosomal degradation through its binding mode to GABARAPL2 and LC3B. In the absence of IRGQ, free MHC class I heavy chains do not only accumulate in the cell but are also transported to the cell surface, thereby promoting an immune response. Mice and human patients suffering from hepatocellular carcinoma show improved survival rates with reduced IRGQ levels due to increased reactivity of CD8+ T cells toward IRGQ knockout tumor cells. Thus, we reveal IRGQ as a regulator of MHC class I quality control, mediating tumor immune evasion.

INTRODUCTION

The major histocompatibility complex class I (MHC class1) proteins are pivotal mediators of the adaptive immune response. By displaying antigenic peptides they activate CD8+ T cells, which eliminate cells with foreign peptides.[1] MHC class I molecules are heterodimers formed by a heavy chain, the transmembrane glycoprotein human leukocyte antigen (HLA), and a light chain, β_2-microglobulin (B2M).[2] MHC class I heterodimers are loaded with 8–12 amino acid peptides derived from proteasomal degradation. Assembly, quality control, and trafficking of MHC class I molecules are coordinated processes that occur in the endoplasmic reticulum (ER) and involve multiple modifying enzymes and chaperones, such as the peptide-loading complex (PLC).[3,4] When the MHC class I molecule is loaded with a high-affinity peptide, its conformation is stabilized and it can be released from the PLC to be trafficked to the plasma membrane.

Various forms of MHC class I molecules may be present in cells: kinetically stable trimers consisting of heavy chain, B2M, and high-affinity peptides (later referred to as "conformational HLA") or heavy chain, B2M, and low-affinity peptides; dimers without peptides; or free heavy chains (these forms together are referred to as "non-conformational HLA"). MHC class I molecules are continuously removed from the cellular surface and degraded or recycled intracellularly. Non-conformational HLA molecules are retained inside the cell through quality control mechanisms and can be degraded through the ER-associated degradation (ERAD) pathway or via autophagy.[5–8]

Autophagy is a tightly regulated process responsible for lysosomal degradation of nonfunctional cellular components, maintaining energy balance during starvation and protecting against harmful material. It also plays a key role in immunity by clearing intracellular microbes.[9–12] During autophagy, a double-membrane structure, the phagophore, forms and expands to

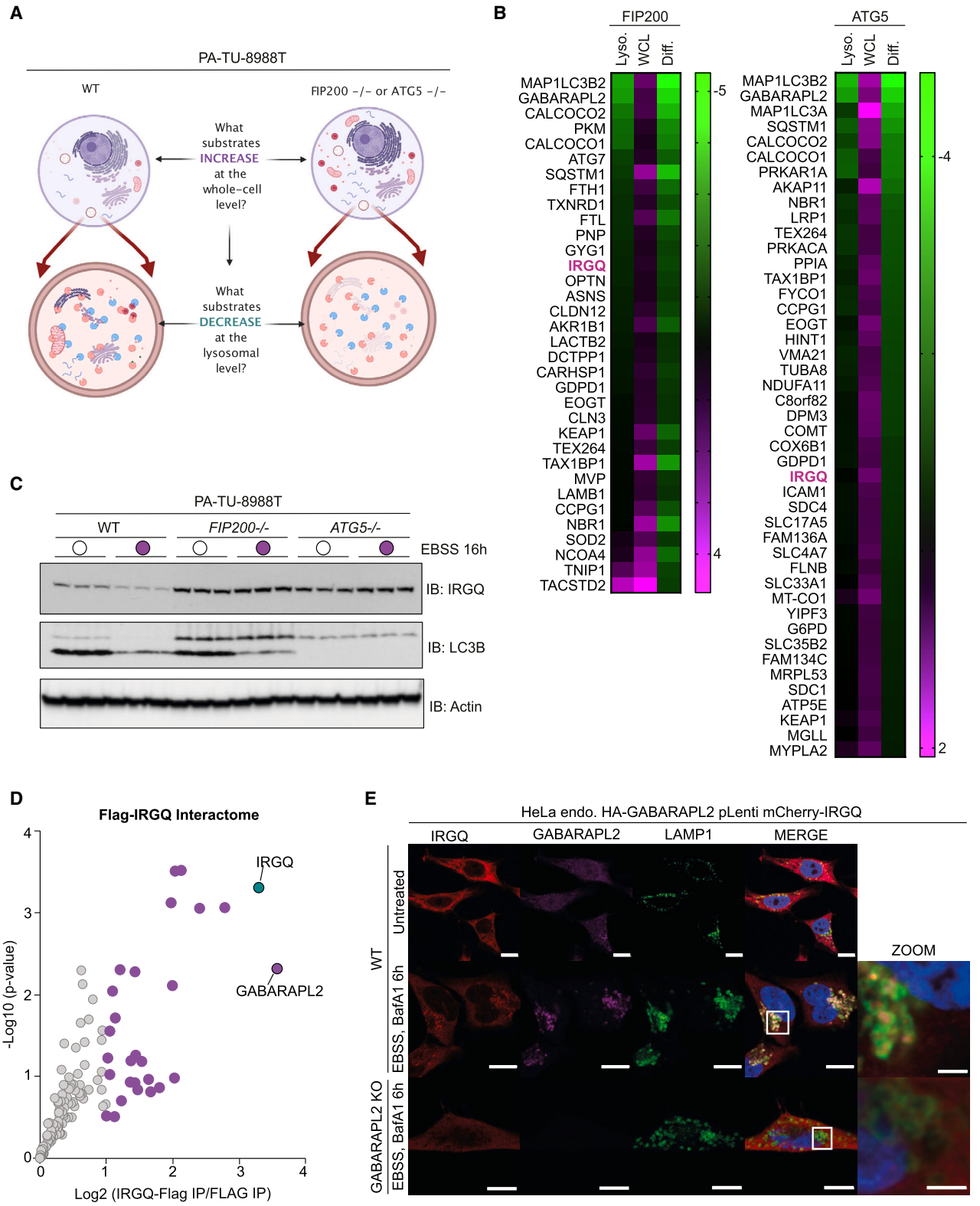

Figure 1. IRGQ is an autophagy receptor

(A) Schematic showing the process of identification of autophagy receptors and cargo proteins in the lysosome.

(B) Heatmap of protein abundances and differences of a list of representative high-confidence autophagy substrate proteins.

(legend continued on next page)

encapsulate cargo, creating an autophagosome. Phagophore formation is governed by a multiprotein complex composed of ULK1/2, ATG13, FIP200, and ATG101. Additionally, there are two systems involving the LC3/ATG8 family (MAP1LC3A, MAP1LC3B, MAP1LC3C, GABARAP, GABARAPL1, and GABARAPL2/GATE-16) that contribute to the expansion of the phagophore, the fusion of the autophagosome with the lysosome, and cargo sequestration in selective autophagy: the ATG12-ATG7-ATG5 conjugation pathway and the ATG4-mediated processing of LC3 proteins with subsequent conjugation to phosphatidylethanolamine (PE) in the membrane of the phagophore.[13,14] Selective autophagy uses receptors with LC3-interacting regions (LIRs) to recognize cargo.[15,16] We identified immunity-related GTPase family Q (IRGQ) as an autophagy receptor and key regulator of MHC class I quality control using quantitative proteomics.

IRGQ belongs to the family of immunity-related GTPases (IRGs), which play an essential role in the defense against intracellular pathogens.[17] There are 24 IRG genes in mice, but only three are conserved in humans (IRGC, IRGM, and IRGQ).[18] IRGC has been linked to sperm motility.[19,20] IRGM regulates the interferon (IFN) response and promotes intracellular pathogen clearance through autophagy.[21–30] IRGQ has been described as a possible oncogene in human hepatocellular carcinoma (HCC).[31] HCC is a malignant tumor with poor prognosis that accounts for 85% of all liver cancer cases.[32] High expression of IRGQ in HCC tissues correlates with higher expression of circular RNA circ_0000854, which accelerates HCC progression. IRGQ might be regulated by microRNA miR-1294,[31] but functional mechanisms or properties are unknown.

Here, we unveil that IRGQ is an immunity modulator that impacts MHC class I molecule presentation. We identify IRGQ as an autophagy receptor that interacts with GABARAPL2 and LC3B and is trafficked to lysosomes in an autophagy-dependent manner, thereby acting as a key regulator of MHC class I quality control. HCC patients and mice suffering from liver cancer have a better overall survival rate when expression of IRGQ is low because then MHC class I presentation is higher and the immune response is stronger.

RESULTS

IRGQ as an autophagy receptor

PA-TU-8988T are human pancreas adenocarcinoma cells with a high basal level of autophagy.[33] To query the autophagic cargo receptor network, we disrupted autophagy flux to the lysosomes by generating ATG5 and FIP200 CRISPR-Cas9 knockout (KO) cells and compared the lysosomal contents of wild-type (WT) cells with those lacking either ATG5 or FIP200. In cells with defective autophagy, autophagic cargoes should decrease, along with autophagy receptors in the lysosomal compartments, while accumulating at the whole-cell level (Figure 1A). We therefore performed a multiplexed TMT (tandem mass tag) LysoIP[34–37] in bafilomycin-treated WT, ATG5−/−, FIP200−/−, and whole-cell proteomics in the same cohort but unperturbed, compared the changes in protein abundances at both the lysosomal and whole-cell levels, respectively, and generated a list of high-confidence autophagy-associated factors (Figure 1B). Deletion of either ATG5 or FIP200 significantly reduced the capture of model autophagy substrates (e.g., MAP1LC3B2, GABARAPL2, CALCOCO2, and SQSTM1/p62); (Figures 1B and S1A–S1C). We identified IRGQ among them (Figure 1B). To corroborate that IRGQ is an autophagy receptor, we monitored IRGQ levels upon autophagy induction by EBSS-induced starvation. IRGQ levels decreased upon EBSS treatment in a manner that is dependent on ATG5 or FIP200 (Figure 1C) and were rescued by BafA1 treatment (Figure S1D).

Because IRG genes in mice are IFN-inducible GTPases, we tested whether IRGQ is IFN-inducible or can bind guanosine triphosphate (GTP). In accordance with previous studies[18] that report a missing promoter sequence in the human IRGQ gene, IRGQ was not IFN-inducible (Figure S1E). Furthermore, IRGQ did not bind GTP (Figure S1F), as all key residues mediating GTP binding are missing in IRGQ (Figure S1G). To determine the role of IRGQ in cells, we transiently transfected and immunoprecipitated FLAG-IRGQ from HeLa cells (Figure 1D). The most highly enriched protein in FLAG-IRGQ eluates was GABARAPL2, a member of the mammalian ATG8 family of autophagy modifiers that are critical for autophagosome formation, cargo recruitment, and autophagosome-lysosome fusion.[38,39]

In order to confirm that IRGQ is trafficked to lysosomes via autophagy, we performed immunofluorescence with cells expressing exogenous mCherry-IRGQ (Figure 1E). Under basal conditions, mCherry-IRGQ appeared diffuse throughout the cytosol. However, nutrient starvation induced by EBSS resulted in the accumulation of mCherry-IRGQ in LAMP-1-positive lysosomes (Figure S1H) along with endogenous GABARAPL2. Because GABARAPL2 is the most prominent binding partner of IRGQ and its degradation in lysosomes is starvation induced, we tested whether GABARAPL2 is required for its trafficking to the lysosome. Indeed, in GABARAPL2-KO cells, IRGQ no longer accumulated in lysosomes upon induction of bulk autophagy, indicating that the translocation of IRGQ from the cytosol to lysosomes depends on the core ATG8 machinery (Figures S1H and S1I). The trafficking of IRGQ to lysosomes and its co-localization with endogenous LAMP1 and LC3B under starvation conditions was confirmed in HeLa cells with endogenously mCherry-tagged IRGQ (Figures S1J and S1K).

(C) SDS-PAGE and western blot of PA-TU-8998T (WT, FIP200$^{-/-}$, and ATG-5$^{-/-}$) cells starved for 16 h with EBSS. Protein lysates were analyzed by western blot with the indicated antibodies.

(D) HEK293T cells were transfected with FLAG-IRGQ, lysates used for immunoprecipitations (IPs), and processed for MS. Data were analyzed with MaxQuant and Perseus; $n = 3$. The volcano plot represents the Student's t test difference from FLAG-IRGQ over control IPs and −log Student's t test p value from FLAG-IRGQ over control IPs. The bait IRGQ is marked in green, and the most significant interaction partner is GABARAPL2, marked in purple. All other proteins identified as significant interaction partners are represented by purple dots.

(E) Immunofluorescence of endogenously HA-tagged GABARAPL2 or GABARAPL2 KO HeLa cells, expressing mCherry-IRGQ. Cells were treated for 6 h in EBSS, with BafA1 (200 nM). Fixed cells were probed with endogenous LAMP1 and HA antibodies. ImageJ plots and quantification: Figures S1H and S1I. Scale bar: 10 and 2 μm in zoom images.

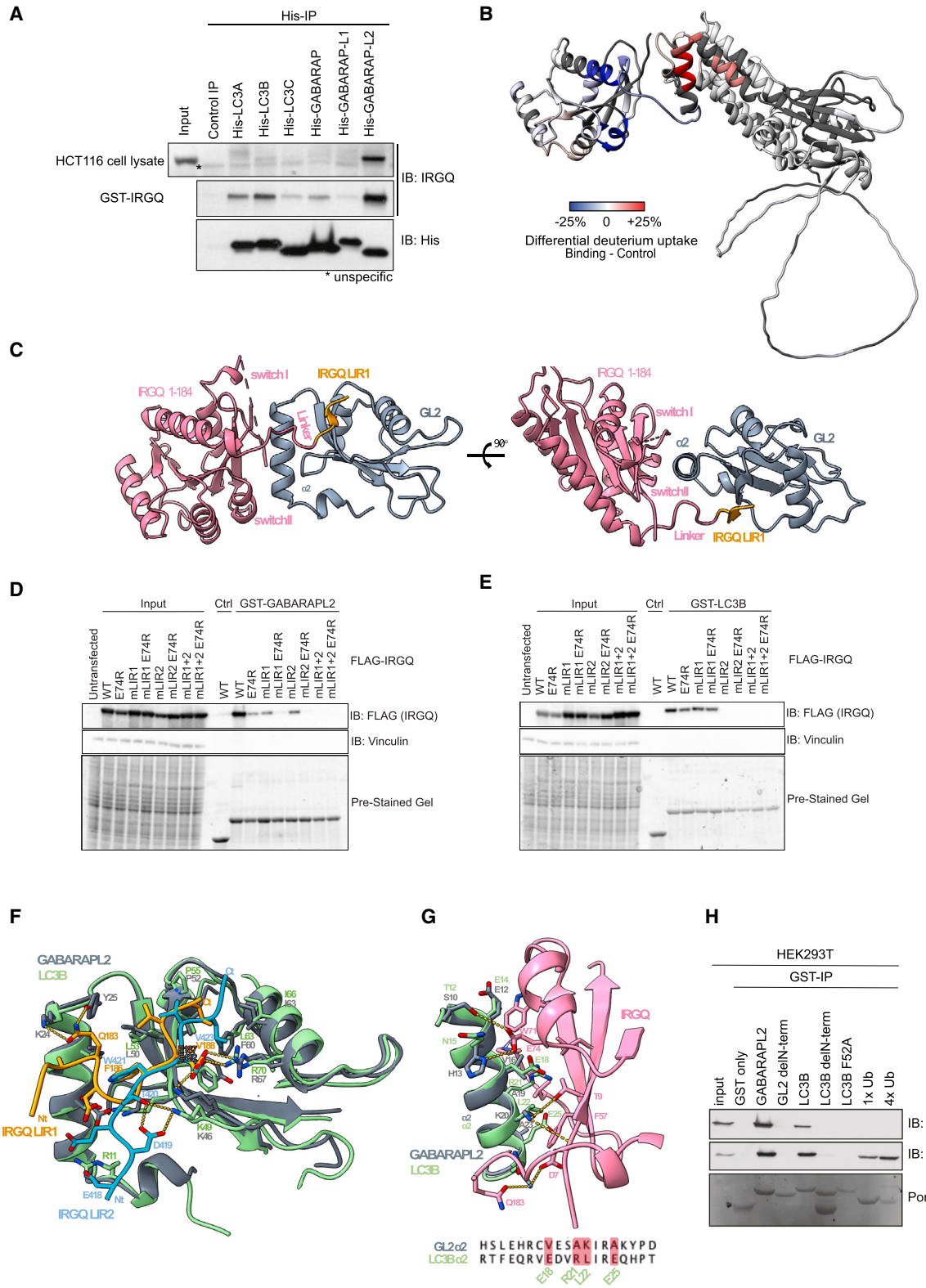

(legend on next page)

IRGQ interacts with the autophagy machinery

To check whether IRGQ also interacts with other hATG8 family members,[40,41] Histidine-tagged hATG8 proteins (LC3A, LC3B, LC3C, GABARAP, GABARAPL1, and GABARAPL2) were either incubated with HCT116 cell lysate or with purified GST-IRGQ and immunoprecipitated using anti-histidine beads (Figure 2A). We found that IRGQ from cell lysate bound strongly to GABARAPL2 and weakly to LC3B, whereas purified GST-IRGQ bound to all hATG8 proteins, with GABARAPL2 being the strongest interaction partner.

Protein sequence analysis of IRGQ using iLIR (http://ilir.warwick.ac.uk)[42] identified two canonical LC3-interacting regions (LIR): one in the N-terminal region of the protein (residues 186–189; LIR1) and one in the C-terminal of the protein (residues 421–424; LIR2). Both LIR sequences are highly conserved across different species (Figures S2A and S2B) and are similar to the canonical—[W/F/Y]xxL—LIR motif in other Atg8-interacting proteins.[43] Interestingly, the other family members of IRG in humans, IRGM and IRGC, lack these LIR sequences (Figure S2C). The interaction of IRGM with human ATG8 family members is LIR independent[44] and we verified that IRGQ KO cells do not have altered IRGM protein levels (Figure S2D).

We made use of hydrogen-deuterium exchange (HDX) mass spectrometry (MS) to investigate the *in vitro* binding modes and associated conformational dynamics of IRGQ upon binding to GABARAPL2 and LC3B (Figures S3A and S3B). We incubated GST-IRGQ with GABARAPL2 (Figures 2B and S3C) or LC3B (Figure S3D) and recorded deuterium uptake over time. In the presence of GABARAPL2, we observed decreased deuterium uptake in three sequence loci of IRGQ, including the predicted LIR1 motif (R176-A191) and two adjacent helices within the N-terminal domain (S62-A75 and L168-L175), indicating a putative binding site for GABARAPL2. To test whether the suggested fragment of IRGQ predicted by HDX binds to the LIR-docking site (LDS) (LC3 docking site) of hATG8 proteins, we crystallized an N-terminal fragment of IRGQ (1–192) in complex with GABARAPL2. The resulting crystals diffracted to 1.8 Å resolution, and we could solve the structure of this complex (Table S1). The structure showed the canonical binding mode of the LIR1 of IRGQ buried into the LDS of GABARAPL2, where F186 and L189 occupy the HP1 and HP2 of LDS (Figure 2C). Interestingly, the N-terminal domain of IRGQ (1–184), which shares structural similarity with the G-protein fold, makes extensive interactions with GABARAPL2. Specifically, the helix 2 (α-2) of GABARAPL2 binds with the pocket formed by the switch I (partially disordered), switch II G-protein region, and the linker between LIR1 and N-terminal G-domain (Figure 2C). This additional interaction of α-2 confers the functional consequence of specificity in binding of IRGQ to GABARAPL2.

To validate this interface, we generated an E74R mutation of IRGQ to disrupt the interaction with the α-2 of GABARAPL2. In addition, we tested the individual contribution of LIR1 and LIR2 motifs to bind GABARAPL2 and LC3B individually. Immunoprecipitation experiments confirmed that LIR1 and E74 of IRGQ were required for binding to GABARAPL2 but were not essential for the interaction with LC3B (Figures 2D and 2E). On the other hand, the LIR2 motif in IRGQ was not the preferential binding site of GABARAPL2 but specifically recruited LC3B (Figures 2D and 2E).

To gain insights into the mechanism of LC3B binding to IRGQ, we attempted to co-crystallize the IRGQ LIR2 (417–425) peptide with LC3B. The crystal structure was solved at 1.6 Å resolution (Table S1). We found that the LIR2 motif (residues 421–425) interacted with the LDS of LC3B, with W421 plugging the HP1 site and L424 occupying the HP2 sites, respectively. An overlay between LC3B in complex with the IRGQ LIR2 peptide and GABARAPL2 in complex with the IRGQ LIR1 peptide (183–190) showed that both complexes shared the canonical LIR interaction but displayed distinct binding modes of the LDS (Figure 2F). LIR2 N terminus bound R11 from α-helix 1 of LC3B, whereas the LIR1 N terminus recruited L24 and Y25 of α-helix 2 of GABARAPL2 for interaction. However, the second molecule in the asymmetric unit of LC3B-LIR2 crystals showed a binding mode similar to GABARAPL2, where H27 and K51 of LC3B formed H-bonds with E418 and T420 of LIR2, respectively (Figure S3E). The LIR1 site of IRGQ was protected from interactions with LC3B due to the prerequisite of helix 2 interactions. The LIR1-mediated binding mode was not feasible for the IRGQ-LC3B complex due to the presence of bulky, charged residues (E18, R21, and E25) in helix 2 of LC3B causing steric clashes (Figure 2G). Deletion of the N-terminal α-helix 2 of GABARAPL2 or LC3B prevented binding to IRGQ as well as

Figure 2. Specific binding modes of IRGQ to GABARAPL2 and LC3B

(A) SDS-PAGE and western blot of an *in vitro* His-pull-down using purified His-hATG8 proteins together with either HCT116 cell lysate or purified GST-IRGQ.

(B) Differences in deuterium uptake of IRGQ upon binding to GABARAPL2. Relative deuterium uptake by IRGQ was measured as a percentage of maximum uptake in the presence of GABARAPL2 (78% coverage, 2.72 redundancy, 3 min exposure). The uptake difference (binding—control) was mapped onto the AlphaFold model of full-lengh IRGQ (AF-A1A4Y4-F1) and indicated using a color gradient from red (decreased) via white (unchanged) to blue (increased).

(C) Structure of IRGQ N-terminal domain 1–184 (pink) and IRGQ LIR1 185–190 (orange) in complex with GABARAPL2 (gray). In addition, to the canonical LIR1 motif interactions, GABARAPL2 α-helix 2 makes extensive contacts within a pocket formed by the structurally conserved switch I (partially disordered), switch II G-protein region, and the linker between LIR1 and N-terminal G-domain.

(D) SDS-PAGE and western blot blotting of an *in vitro* GST pull-down using purified GST-GABARAPL2 together with HEK293T cell lysate transfected with FLAG-IRGQ WT or FLAG-IRGQ mutants (LIR1 mutant = F186A L189A, LIR2 mutant = W421A L424A).

(E) Same as (D), but using GST-LC3B instead of GST-GABARAPL2.

(F) The structure of LC3B (green) in complex with the IRGQ LIR2 peptide (416–425) (blue) overlaid with GABARAPL2 (gray) and the IRGQ LIR1 peptide (183–190) (orange) shows distinct binding modes of the two IRGQ LIR peptides.

(G) Structural superposition and sequence alignment of the α2 helices of GABARAPL2 (gray) and LC3B (green). Non-conserved, bulky, charged residues of LC3B (E18, R21, and E25) and a loss of hydrogen bonding with IRGQ D7 carbonyl oxygen via K20 to L22 prevent interaction of LC3B with IRGQ at the N-terminal domain (pink).

(H) SDS-PAGE and western blot of an *in vitro* GST pull-down using purified indicated GST proteins together with HEK293T cell lysate.

Table 1. Structural models of IRGQ-hATG8 complexes

Binding modes	IRGQ-GABARAP	IRGQ-GABARAPL1	IRGQ-GABARAPL2	IRGQ-LC3A	IRGQ-LC3B	IRGQ-LC3C
LIR1-LDS[a]	4/25	1/25	18/25[a]	6/25	2/25	6/25
LIR1*-LDS	3/25	1/25	0/25	3/25	0/25	1/25
LIR2-LDS[a]	18/25[a]	13/25[a]	7/25	13/25[a]	18/25[a]	11/25
LIR2*-LDS	0/25	6/25	0/25	3/25	3/25	6/25
No LIR-LDS	0/25	4/25	0/25	0/25	2/25	1/25

Table summarizing the binding modes between IRGQ and hATG8 proteins in top 25 modeled complexes. Five predominant binding modes are observed; two canonical LIR-LDS (LIR1-LDS and LIR2-LDS) binding modes; two partially docked LIR*-LDS (LIR1*-LDS and LIR2*-LDS), and binding mode with no LIR involvement. The relative populations of these modes in the top-ranked AlphaFold2 models-multimer models are provided and representative images of IRGQ-GABARAPL2 (LIR1-LDS), as well as IRGQ-LC3B (LIR2-LDS), are depicted in Figures S3F and S3G.
[a]predominant binding mode

LC3B containing the LDS mutation (F24A) (Figure 2H). To test the differential binding of hATG8 proteins to IRGQ LIR1 and LIR2 sites, we modeled the three-dimensional (3D) structure of all six IRGQ-hATG8 complexes using AlphaFold2-multimer (Table 1). In the top-ranked complex models, we found that hATG8 proteins could interact with IRGQ using alternate binding modes involving either LIR1 or LIR2 sites. We analyzed the IRGQ-GABARAPL2 and IRGQ-LC3B complex models in detail (Figures S3F and S3G) and found that GABARAPL2 was sequestered by IRGQ predominantly using the LIR1-LDS binding mode (18/25 top models; Table 1; Figure S3F), whereas the LC3B interaction was mediated predominantly by the LIR2-LDS binding mode (18/25 top models; Table 1; Figure S3G). Our modeling data suggested that the LIR1-LDS binding mode was essential to recruit GABARAPL2 and LIR2-LDS for LC3B, respectively (Figures S3F and S3G).

In summary, LC3B bound to IRGQ via the LIR2 motif in a single binding mode, whereas GABARAPL2, despite having two potential binding modes (both to LIR1 and LIR2), showed a strong preference for binding to the N-terminal domain of IRGQ followed by the LIR1 motif.

IRGQ modulates MHC class I levels at the cell surface

To assess the physiological role of IRGQ, we performed a multiplexed TMT-total proteome analysis of PA-TU-8988T IRGQ WT and KO cells (Figure 3A). As expected, IRGQ was depleted from IRGQ KO cells, whereas, interestingly, HLA family members were highly accumulated. In addition, we analyzed total proteomes of PA-TU-8988T WT, IRGQ KO, or FIP200 KO cells under fed and starved conditions and compared organelle classes (Figures S4A–S4C). As expected, starvation in WT cells induces turnover of the ER, lysosome, and endosomes (Figure S4A). The starvation-mediated turnover of the ER, lysosomes, and endosomes also occurs in the absence of IRGQ (Figure S4B). Because FIP200 is an essential autophagy gene, its absence blocks the turnover of the ER, lysosomes, and endosomes under starvation conditions (Figure S4C). Therefore, it is unlikely that IRGQ plays a global role in autophagy or ER-phagy, as is the case for FIP200, but rather has selected, specific targets. To determine whether IRGQ mediated the regulation of HLA transcription or degradation at the protein level, we first performed real-time quantitative PCR (qPCR) of HLA-A, -B, -C, and B2M in the presence or absence of IFNγ (Figure 3B). As expected, IFNγ treatment induced the transcription of HLA and B2M proteins. IRGQ KO also significantly influenced HLA but not B2M mRNA levels; however, not to the same extent as induction through IFNγ (Figure 3B). We then tested the overall protein levels of HLA molecules in different WT and IRGQ-depleted cell lines (Figures 3C, 3D, and S4D–S4F). We found that HLA molecules accumulated in IRGQ-depleted cells, whereas IRGQ overexpression resulted in HLA downregulation (Figure 3C). The reciprocal correlation between the levels of HLA molecules and IRGQ in various cell lines suggested that IRGQ can regulate MHC class I protein levels in tumorigenic (PA-TU-8988T, HeLa, Huh-7, and SK-N-AS1) and healthy primary cells (human macrophages), whereas MHC class II was not affected (Figure 3E). Next, we confirmed that the function of IRGQ can be restored in PA-TU-8988T IRGQ KO cells by re-introducing doxycycline-inducible WT HA-IRGQ (Figure S4G). The levels of HLA are equal in WT and doxycycline-treated PA-TU-8988T IRGQ KO pLDT HA-IRGQ cells, whereas HLA levels are elevated in these cells without doxycycline treatment (Figure S4H).

To test whether IRGQ's effects on HLA accumulation were mostly post translational, we quantified the protein turnover by using a cycloheximide (CHX) pulse chase assay (Figure S4I). After CHX treatment, WT cells showed reduced HLA levels, whereas IRGQ KO cells did not, indicating IRGQ's role in HLA protein clearance. BafA1 and MG132 treatments revealed that IRGQ-mediated HLA degradation primarily occurs via the autophagic pathway, with partial involvement of the proteasome (Figure S4I).

To assess the role of IRGQ in the autophagic degradation of MHC class I, endogenously tagged mCherry-IRGQ HeLa were subjected to EBSS-mediated starvation. Immunoprecipitation of mCherry-IRGQ revealed equal levels in treated and untreated cells; however, upon nutrient starvation, IRGQ's interaction with GABARAPL2 and MHC class I molecules (HLA-C, HLA-A, and B2M) increased (Figure 3F). We confirmed this by proximity-ligation of IRGQ and HLA class I ABC molecules in cells treated with the autophagy inducer Torin-1(Figure S4J). Because MHC class I molecules exert their function at the cell surface, we profiled the total cellular surfaceOME in PA-TU-8988T (Figure 3G) and HeLa cells (Figure S4K). To this end, we biotin-labeled the cell surface proteins and subjected them to MS analysis. HeLa cells stably overexpressing HA-IRGQ exhibited fewer HLA surface molecules (Figure S4K). This was confirmed by

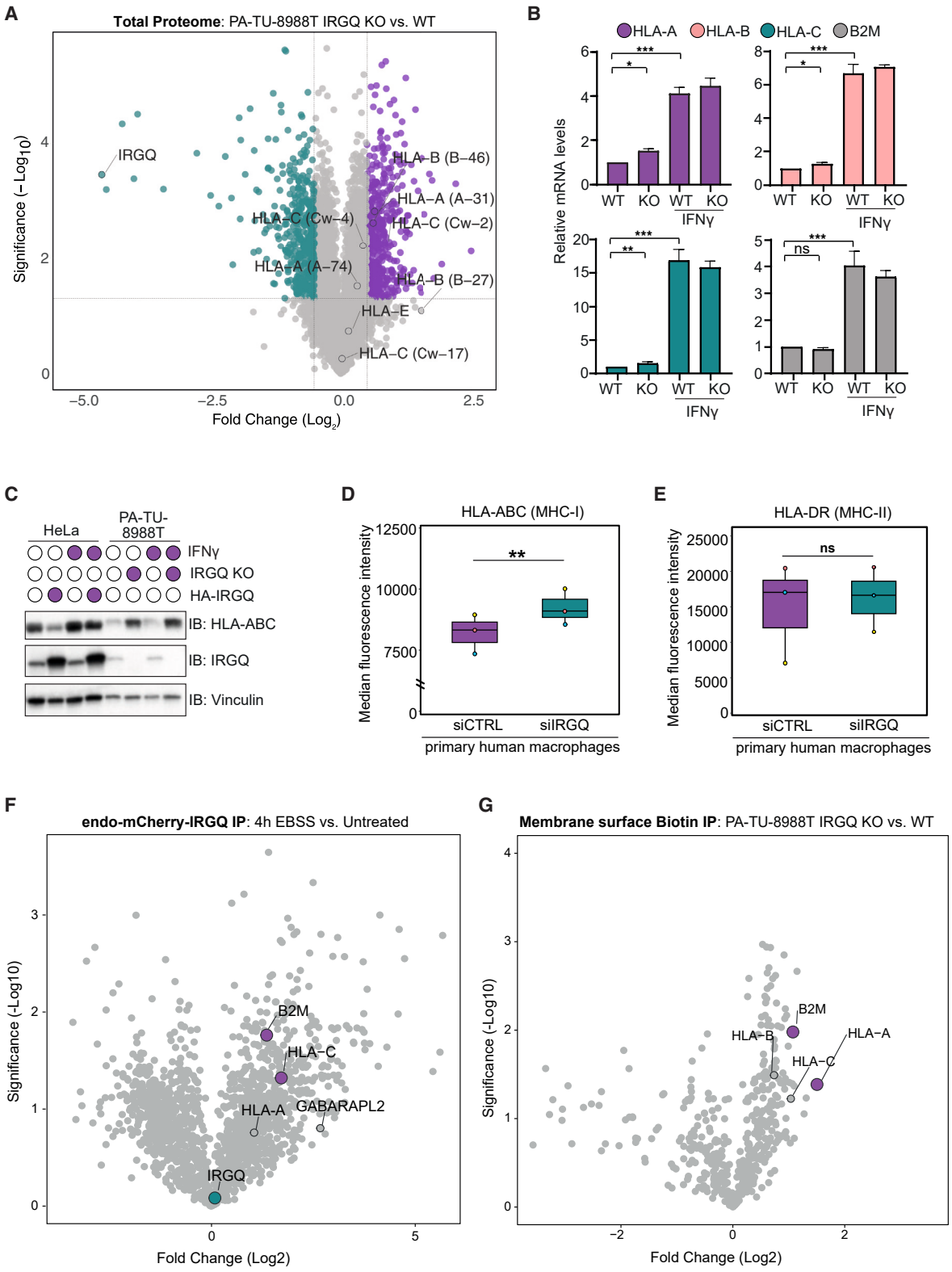

Figure 3. IRGQ reduces MHC class I levels on the membrane and intracellularly

(A) Total proteome analysis of TMT-labelled IRGQ WT and KO PA-TU-8988T cells reveals accumulation of MHC class I molecules. Data were analyzed with MaxQuant and Proteome Discoverer; *n* = 3. The volcano plot represents the Student's t test difference from IRGQ KO over WT cells and −log Student's t test

(legend continued on next page)

fluorescence-activated cell sorting (FACS) analyses of cell surface HLA in these IRGQ-overexpressing HeLa cells (Figure S4L). Conversely, the small interfering RNA (siRNA)-mediated depletion of IRGQ in the HCC cell line Huh-7 caused an accumulation of total HLA surface levels (Figure S4M). In PA-TU-8988T IRGQ KO cells, HLA molecules were the most enriched surface proteins compared with WT cells (Figure 3G). Notably, comparison of HLA levels at the cell surface and the whole-cell level showed that the accumulation of HLA molecules in IRGQ KO cells at the whole-cell level (input) was not mirrored at the cellular surface but that most of the accumulated HLA molecules remained intracellularly (Figure S4N).

IRGQ-MHC class I complexes traffic through the autophagic pathway

Across different cell types, high expression of IRGQ was associated with reduced levels of HLA, and vice versa. To decipher the mechanism of IRGQ-mediated MHC class I instability, we performed cell fractionations of PA-TU-8988T WT and IRGQ KO cells (Figure 4A). IRGQ could be detected in the cytosol and the ER. The levels of HLA proteins in IRGQ KO cells were higher than in WT cells, both in the input (total cell lysate) and the ER. The levels of EGFR, another cell surface protein, were not affected by IRGQ depletion, indicating specificity for MHC class I (Figure 4A). To monitor the localization of IRGQ upon autophagy induction, we used the complementation affinity purification (BiCAP) method[45]: two halves of the split-Venus system (Vn and Vc) tethered to two potentially interacting proteins generate a functional fluorescent protein upon complexation. Confocal microscopy revealed that IRGQ and HLA molecules were distinctly localized in the cell (Figure 4B). Upon autophagy induction, proximity-labeled dimers of IRGQ (Vn-IRGQ and Vc-IRGQ constructs) were detected in the ER membrane (co-localization with REEP5), on autophagosomes (co-localization with BFP-LC3B), and in lysosomes (co-localization with LAMP1) (Figure 4C). In order to track the interaction of IRGQ and HLA, we co-transfected Vn-IRGQ with HLA-Vc and monitored their proximity with live-cell imaging (Figure 4D). We found that both IRGQ and HLA molecules were proximal and moved together, presumably as a complex, into autophagosomes and lysosomes (Figure 4D; Video S1). Vn-IRGQ/HLA-Vc heterodimers and Vn/Vc-IRGQ homodimers were distinctly co-localized and detected inside lysosomes (lysotracker stain), which is not the case for proximal HLA-Vn/Vc homodimers (Figure 4E).

IRGQ degrades non-conformational MHC class I through autophagy

Prior to their transport to the plasma membrane, MHC class I molecules undergo maturation in the ER, and different conformers coexist in cells. To decipher which HLA conformation IRGQ acts on, we fractionated cells into soluble and insoluble fractions[46] (Figures 5A and S5A). BafA1 treatment increased the amount of HLA in the insoluble fraction at similar levels in WT and KO IRGQ PA-TU-8988T cells. MG132 treatment, which blocks proteasomal degradation of MHC class I after retrograde transport into the cytosol and peptide generation for MHC class I peptide loading, further increased the amount of insoluble HLA, with significantly more insoluble HLA present in IRGQ KO cells (Figures 5A and S5A). Misfolded non-conformational HLA molecules are known to aggregate in the ER.[47] The fraction of high-molecular-weight species containing HLA aggregates or oligomeric complexes were more prominent in the absence of IRGQ, as detected by native-PAGE (Figure S5B). To measure the amount of MHC class I within the ER, lysates were treated with endoH, an enzyme that only deglycosylates proteins present in the ER and *cis*-Golgi.[48] Significantly more deglycosylated MHC class I molecules were present in IRGQ KO cells, indicating that the percentage of ER-resident MHC class I increased in the absence of IRGQ (Figures 5B and S5C). Importantly, MG132 treatment, which causes an accumulation of "empty" MHC class I molecules due to a restriction of peptide abundance,[49] caused a similar increase of deglycosylated MHC class I molecules in WT cells compared with untreated IRGQ KO cells, but did not further increase in IRGQ KO cells (comparing #4 and #6). This suggested that IRGQ functioned as a major regulator for disposal of ER-resident non-conformational MHC class I molecules. PNGase treatment was used as a positive control to deglycosylate all MHC class I molecules, irrespective of their location (Figures 5B and S5C).

To confirm IRGQ's role in modulating non-conformational HLA, we used two antibodies: HLA-W6/32, which detects the HLA-B2M heterodimer, and a polyclonal HLA-ABC, which

p value from IRGQ KO over WT cells. Proteins significantly depleted in IRGQ KO cells are marked in green and proteins significantly upregulated in IRGQ KO cells are marked in purple.

(B) Relative mRNA expression levels of HLA-A, HLA-B, HLA-C, and B2M in IRGQ WT and KO cells in the presence or absence of IFNγ (10 ng/mL, 24 h). $n = 3$.

(C) SDS-PAGE and western blot of HeLa WT and HA-IRGQ transfected, as well as PA-TU-8988T WT and IRGQ KO cells in the presence or absence of IFNγ (10 ng/mL, 24 h).

(D) FACS analysis of HLA-ABC antibody in primary human macrophages from three healthy donors transfected with control or IRGQ siRNA. Data are presented as the box-and-whisker plot and individual donors are color coded. $n = 3$.

(E) Same as in (D) but using HLA-DR antibody.

(F) Interactome of endogenous IRGQ during starvation-induced autophagy in HeLa cells. Data were analyzed with MaxQuant and Perseus; $n = 3$. The volcano plot represents the Student's t test difference and −log Student's t test *p* value from endogenous mCherry-IRGQ IP under basal or EBSS (4 h) and BafA1 (4 h, 200 nM) treated condition. The bait IRGQ is marked in green and significantly increased binding to HLA-C and B2M (both marked in purple) is observed upon EBSS treatment.

(G) SurfaceOME of IRGQ WT and KO PA-TU-8988T cells. Biotinylated surface proteins were immunoprecipitated by streptavidin, and proteins were analyzed with MaxQuant and Perseus; $n = 3$. The volcano plot represents the Student's t test difference and −log Student's t test *p* value from IRGQ KO over WT cells. Proteins significantly enriched in IRGQ KO cells are HLA-A and B2M (marked in purple).

Data are presented as the mean with error bars indicating the SD. Statistical significance of differences between experimental groups was assessed with Student's t test. Differences with $p < 0.05$ are annotated as *, $p < 0.01$ are annotated as **, and $p < 0.001$ are annotated as ***; n.s. not significant. See also Figure S4.

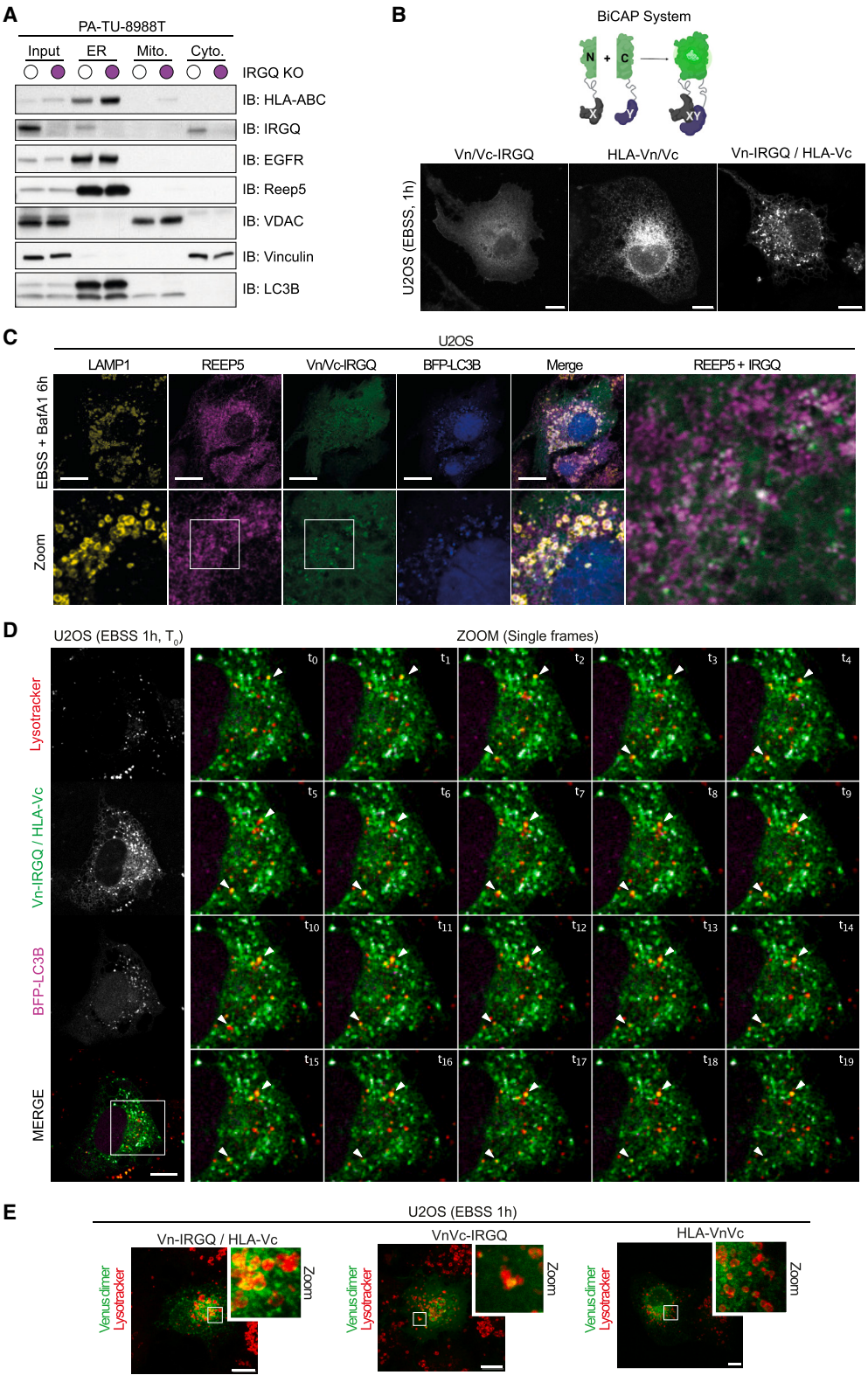

Figure 4. IRGQ forms a complex with MHC class I

(A) PA-TU-8988T WT and IRGQ KO cells were fractionated into ER, mitochondria, and the cytosol following SDS-PAGE and western blot with indicated antibodies. Cellular fractionation reveals that IRGQ KO-mediated MHC class I accumulation occurs in the ER.

(legend continued on next page)

recognizes the HLA heavy chain regardless of conformation (Figure 5C). Higher HLA levels were found in IRGQ KO cells with the HLA-ABC antibody in the 1st IP, but not with HLA-W6/32. A 2nd IP using the opposite antibodies confirmed this, showing HLA accumulation in IRGQ KO cells with HLA-ABC but not HLA-W6/32 (Figure 5D). This indicates that the accumulated HLA in IRGQ KO cells is non-conformational.

To further dissect this, FACS analysis of surface HLA molecules was performed using the polyclonal HLA-ABC antibody, the conformational HLA-W6/32 clone, and the HLA-HC10 clone, which only detects free HLA heavy chains (Figure 5E). Again, HLA-ABC and conformational HLA-W6/32 molecules were slightly enriched on the cellular surface of IRGQ-depleted cells. Free heavy chains (HLA-HC10) should not be detectable on the cellular surface, as these molecules should have undergone stringent quality control mechanisms prior to reaching the membrane; however, in PA-TU-8988T and HeLa IRGQ KO cells, as well as in siRNA IRGQ-depleted Huh7 cells, this quality control pathway is absent. Thus, free HLA heavy chains (HLA-HC10) were only detected on the membrane of IRGQ KO but not WT cells (Figures 5E, S5D, and S5E). FACS analysis revealed that reintroduction of IRGQ restores surface HLA-HC10 levels back to WT levels, indicating that exogenously expressed HA-IRGQ acts in MHC class I quality control similarly to endogenous IRGQ (Figure S5F). To resolve whether IRGQ also plays a role in AAK1-mediated MHC class I lysosomal uptake,[50] we measured the amount of surface MHC class I from human macrophages of six healthy donors depleted of IRGQ, AAK1, or both (Figure S5G). The knockdown (KD) of IRGQ and of AAK1 could be verified (Figure S5H), and both result in increased MHC class I surface levels; however, there is no additive effect of IRGQ and AAK1 double KD (Figure S5G).

Upon autophagy induction, IRGQ fostered interactions with LC3B and GABARAPL2, which are recruited to the growing phagophore and are important for cargo delivery. In addition, autophagy induction increased co-localization of IRGQ with HLA at the ER. In this light, we investigated the role of IRGQ in HLA degradation through autophagy by monitoring the delivery of conformational and non-conformational HLA molecules to lysosomes in IRGQ WT and KO cells (Figure S5I). Significantly fewer non-conformational HLA molecules (HLA-ABC) were present in lysosomes in the absence of IRGQ, whereas conformational HLA molecules (HLA-W6/32) were unaffected (Figure 5F). Depleting LC3B and GABARAPL2 from IRGQ WT or KO cells (Figure S5J) even further increased the absence of non-conformational HLA from lysosomes (Figure 5G). Compared with WT cells, all single KO (or KD) cells showed a significant reduction in the percentage of positive HLA lysosomes, and this effect was enhanced when two or all three of these proteins were depleted simultaneously (Figure 5G). Thus, HLA degradation through autophagy depended not only on IRGQ but also significantly on its binding partners, LC3B and GABARAPL2.

We tested whether IRGQ directly binds purified MHC class I but found no interaction, suggesting the need for additional adaptors or post-translational modifications (Figure S6A). MS revealed that the Vn-IRGQ/HLA-Vc complex interacts with autophagy-lysosome, ubiquitin-proteasome, and ER proteostasis proteins, including LC3B and MARCH5 (Figures S6B–S6D). HLA ubiquitylation sites at K267 and K340 were only present in IRGQ-bound complexes (Figures S6E and S6F). Mutation of K267/340R reduced co-localization with ER markers and slowed degradation (Figures S6G–S6K). WT HLA interacts with proteasomal subunits, whereas K267/340R associates with kinesins and endosomal proteins (Figure S6L).

Taken together, IRGQ acted in the quality control of MHC class I and directs non-conformational HLA molecules for autophagosome-lysosomal degradation.

IRGQ depletion allows an increased CD8+ T cell response to restrict HCC

HCC is a tumor with strikingly poor prognosis, and targeted therapies with beneficial clinical impact have not yet been successfully developed.[32] IRGQ mRNA (Figure S7A) and protein (Figure S7B) levels were highly upregulated in HCC compared with non-transformed liver tissues. In addition, HCC tumors with elevated IRGQ levels expressed lower levels of MHC class I genes compared with tumors with reduced expression of IRGQ (Figure S7C). Data from publicly available datasets show that HCC patients with an increased IRGQ expression exhibit a significantly shorter survival time compared with patients with low IRGQ expression (Figure S7D). In HCC patients with high CD8+ T cell infiltration into the tumor, the relevance of IRGQ as a survival prognostic factor was markedly increased (Figure 6A) compared with tumors with low CD8+ T cells (Figure S7E). These data indicated that low IRGQ levels positively influenced MHC class I surface expression and favor a CD8+ T cell response, resulting in a better HCC patient survival rate and highlighting IRGQ as a potential target in HCC tumors with elevated CD8+ T cell infiltration.

To investigate IRGQ's role in immune evasion, we developed an HCC mouse model[51–54] by amplifying *c-Myc* and deleting *Trp53* in C57BL/6J mice[32,51] using hydrodynamic tail vein injection with CRISPR-Cas9 and sleeping beauty gene editing (Figure S7F). Proteome analysis of healthy (WT) and HCC (*c-Myc*; *Trp53Δ*) liver tissue showed upregulation of HCC markers and proliferative indicators.[55] Tumors lacked cholangiocarcinoma markers (Krt7 and Krt19), confirmed hepatocyte origin (Hnf4a),

(B) Schematic of the complementation affinity purification system: BiCAP, Vn/Vc Venus. U2OS cells transfected with homodimer Vn/Vc-IRGQ, homodimer HLA-Vn/Vc, and heterodimer Vn-IRGQ/HLA-Vc, treated for 1 h with EBSS. Representative fluorescence images were taken with a Leica confocal microscope SP8. Scale bar: 5 μm.

(C) U2OS cells transfected with homodimer Vn/Vc-IRGQ and BFP-LC3B, treated for 6 h with EBSS and BafA1. Cells were stained with antibodies against endogenous LAMP1 (to visualize lysosomes) and Reep5 (to depict the ER network). Representative fluorescence images were taken with a Leica confocal microscope SP8. Scale bar: 10 μm.

(D) U2OS cells transfected with heterodimer Vn-IRGQ/HLA-Vc and BFP-LC3B, treated for 1 h with EBSS and lysotracker for 30 min. Live-cell imaging was done with a Leica confocal microscope SP8. Representative video. Scale bar: 10 μm.

(E) U2OS cells transfected with heterodimer Vn-IRGQ/HLA-Vc or homodimers of Vn/Vc-IRGQ and HLA-Vn/Vc, treated for 1 h with EBSS and lysotracker for 30 min. Representative fluorescence images were taken with a Leica confocal microscope SP8. Scale bar: 10 μm.

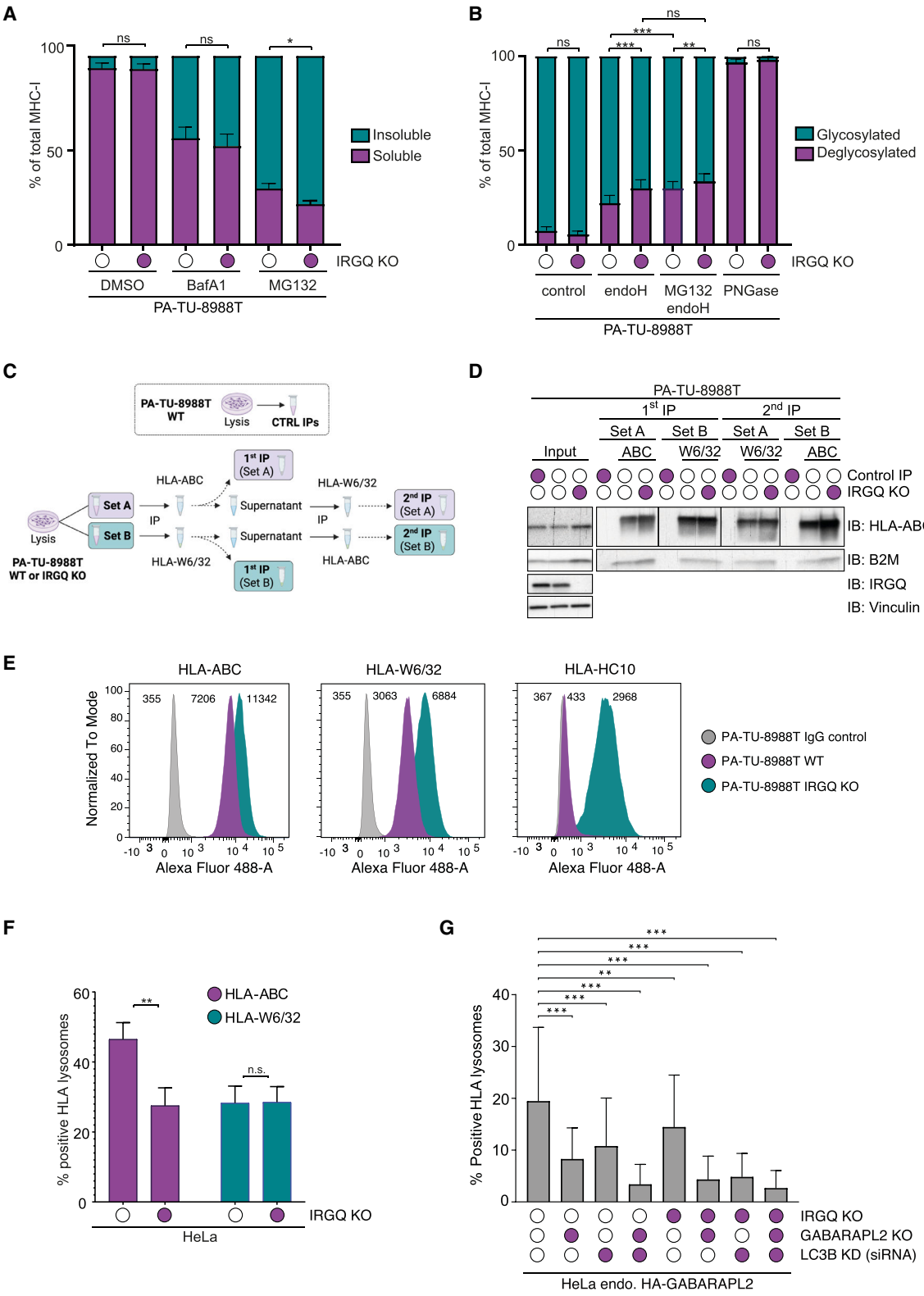

Figure 5. IRGQ degrades non-conformational MHC class I through autophagy

(A) Cellular fractionation of soluble and insoluble cellular components of PA-TU-8988T WT and IRGQ KO cells upon treatment with BafA1 and MG132 (16 h; 100 and 500 nM, respectively). Quantification of the cellular fractionation of HLA levels from western blots (Figure S5A). *n* = 3.

(legend continued on next page)

and HCC classification (Afp and Gpc3), with de-differentiation markers (low Alb) and reduced IFN signaling, characteristic of proliferative HCC[55] (Figure S7F). Aiming to elucidate the function of IRGQ in HCC tumors, we deleted *Irgq* by CRISPR-Cas9 in order to compare *Irgq* WT and KO tumors (*c-Myc*; *Trp53*Δ vs. *c-Myc*; *Trp53*Δ; *Irgq*Δ) (Figure 6B). This was confirmed on a protein level by western blot (Figure S7G). Strikingly, mice with WT *Irgq* tumors displayed a median survival rate of 33 days, whereas mice with *Irgq*Δ tumors lived approximately 82 days (Figures 6C and S7H). *c-Myc*; *Trp53*Δ; *Irgq*Δ mice showed reduced tumor burden compared with WT *Irgq* animals (Figures 6D and 6E). In order to determine whether *Irgq* is required for HCC immune evasion, we monitored survival upon treatment with an anti-CD8 antibody. The survival benefit of the *c-Myc*; *Trp53*Δ; *Irgq*Δ mice was reduced to the survival rate of *c-Myc*; *Trp53*Δ mice upon their treatment with the anti-CD8 antibody, indicating that the *Irgq*-depletion survival benefit stemmed from increased MHC class I presentation with concomitant CD8+ T cell activation (Figure 6F). Next, we confirmed that IRGQ modulates CD8+ T cell activation by degrading non-conformational MHC class I molecules. In IRGQ KO cells, these molecules reach the surface, triggering a stronger T cell-mediated response (Figure 5E).[56,57] T cell killing assays showed increased activation of total human T cells and CD8+ T cells toward IRGQ KO cells, further enhanced by tetanus toxoid as an antigen (Figures 6G and S7I). Additionally, reduced IRGQ expression in gp33-expressing MC38 cells led to elevated Nur77 expression in CD8+ T cells, indicating stronger T cell receptor (TCR) signaling[58] (Figure S7J). In addition, we performed immune cell profiling from the blood of the *c-Myc*; *Trp53*Δ; *Irgq*Δ mice and found that regulatory T cells (Tregs) were not affected (Figure 6I). However, mice with *Irgq* depleted from liver tumors had enhanced levels of activated CD8+ T cells (Figure 6J) as well as PD-1+ CD8+ T cells (Figure 6K), which may represent a hyporesponsive state of T cells due to chronic TCR stimulation.[59]

In summary, we identified IRGQ as a factor involved in immune evasion in HCC.

DISCUSSION

Protein quality control is vital for the proper functioning of MHC class I molecules, which are crucial for the immune system to recognize and respond to foreign substances like pathogens or tumor cells. MHC class I molecules undergo a strict quality control process to maintain their integrity. Cytotoxic T cells monitor these molecules for foreign peptides, triggering an immune response to eliminate infected or cancerous cells. This process ensures effective targeting while preventing excessive immune reactions that could damage healthy tissue.[60,61]

Here, we identified IRGQ as a regulator of immunity and a potential biomarker or therapeutic target for HCC. IRGQ functions as an autophagy receptor by binding GABARAPL2 and LC3B via two LIR motifs and its N-terminal domain. Notably, IRGQ binds LC3B and GABARAPL2 at distinct sites, despite their similarity. This differential binding may enhance autophagy substrate specificity under different physiological conditions. Autophagy induction promotes the degradation of MHC class I molecules[5,50,62,63] and the complex assembly of IRGQ with ATG8 and one of its substrates—MHC class I. In IRGQ-deficient cells, MHC class I levels increase as IRGQ plays a key role in MHC class I quality control. IRGQ interacts with MHC class I in the ER, ensuring improperly formed molecules are degraded via lysosomes. Without IRGQ, faulty MHC class I molecules, including heavy chains without light chains or peptides, reach the cell membrane and these molecules can still, or even more strongly, trigger a CD8+ T cell response (Figure S7K). Indeed, the presence of both empty and conformational MHC class I molecules on the target cell surface enhances T cell killing and immune responses.[56,57] The affinity between CD8 and the MHC class I molecule maintains close contact between the cytotoxic T cell and the target tumor cell during antigen-specific activation in the tumor microenvironment. MHC class I restriction of tetanus toxoid and gp33 requires fully assembled MHC class I complexes. Consequently, these molecules may be displayed in equilibrium with misfolded heavy chains and may also form more readily if misfolded MHC class I molecules are not adequately degraded. Nevertheless, many cancers can evade the immune system, and patients' response to immune checkpoint therapy is highly individualized.[8,32,60,64] Thus, improving tumor immunogenicity is a key factor for more effective immunotherapy.

Liver cancer is the sixth most common cancer and the second leading cause of cancer death due to its high metastatic capacity and recurrence rates.[32] HCC patients and mice with low IRGQ expression show better survival, as reduced IRGQ levels enhance the immune response. In *Irgq*-deficient mice, CD8+ T cells restrict tumor growth, leading to smaller liver tumors. Similarly, low IRGQ levels in humans correlate with better survival in CD8-high HCC tumors. T cells from healthy donors are

(B) Quantification from western blot (Figure S5C) of cellular glycosylation states of MHC class I molecules in PA-TU-8988T WT and IRGQ KO cells, untreated or upon treatment with MG132 (16 h; 500 nM). $n = 7$.

(C) Schematic of sequential HLA-ABC and HLA-W6/32 IPs.

(D) SDS-PAGE and western blot of double immunoprecipitation with conformation-dependent HLA antibodies in PA-TU-8988T WT and IRGQ KO cells according to scheme (C).

(E) FACS analysis of PA-TU-8988T WT and IRGQ KO cells using IgG control, HLA-ABC, HLA-W6/32, and HLA-HC10 antibodies. Free heavy chains of MHC class I (HLA-HC10) are present at the cell surface of IRGQ KO cells.

(F) Quantification of HLA-positive lysosomes (IF images Figure S5I) of at least 50 cells per condition. HeLa WT and IRGQ KO cells were treated with EBSS (4 h) together with BafA1. Less HLA-ABC is present in lysosomes of IRGQ KO cells, whereas conformational MHC class I (HLA-W6/32) is unaffected. Images used for the analysis were taken in z stacks with a Leica confocal microscope SP8. $n = 3$.

(G) Same as (F), but only staining HLA-ABC in HeLa WT cells or cells depleted of IRGQ, LC3B, and/or GABARAPL2. Verification of KO/KD in Figure S5J. IRGQ, GABARAPL2, and LC3B all direct MHC class I for lysosomal degradation.

Data are presented as the mean with error bars indicating the SD. Statistical significance of differences between experimental groups was assessed with Student's t test. Differences with $p < 0.05$ are annotated as *; differences with $p < 0.01$ are annotated as ** and $p < 0.001$ are annotated as ***; n.s. not significant.

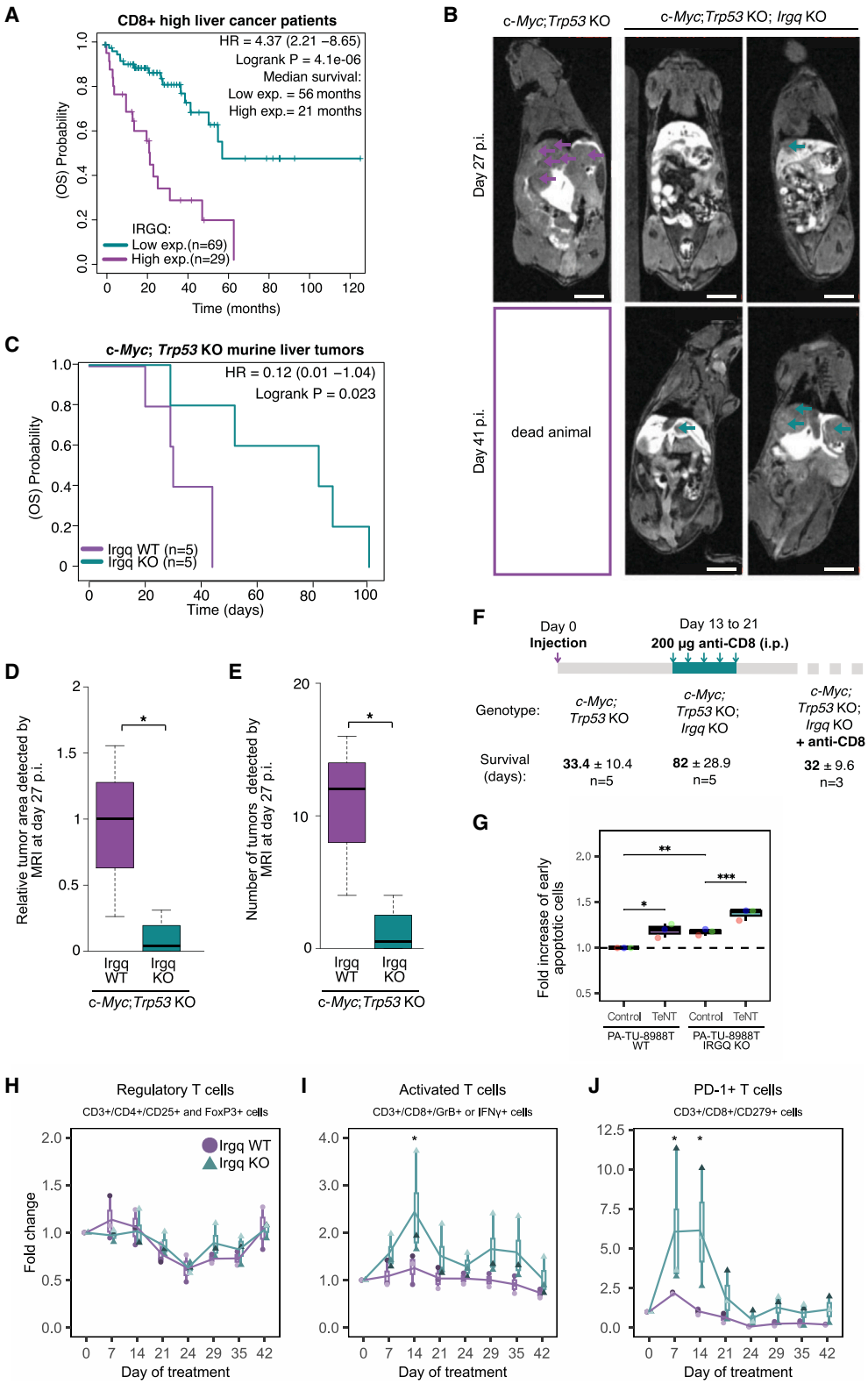

Figure 6. IRGQ regulates CD8+ T cell response in human and murine hepatocellular carcinoma

(A) Kaplan-Meier survival plot of liver cancer patients with high or low IRGQ mRNA expression levels in CD8+ T cell-infiltrated tumors (data obtained from NIH Center for Cancer Genomics, the Cancer Genome Atlas program [TCGA]).

(legend continued on next page)

more reactive to IRGQ KO cancer cells due to higher MHC class I surface levels. In *c-Myc; Trp53Δ; IrgqΔ* mice, the T cell response peaks 7–14 days post activation, with effector T cells actively eliminating cancer cells. The dynamics of the T cell response to cancer may vary depending on several factors, including the type of cancer, the tumor microenvironment, and the specific tumor antigens.[65]

In summary, we unraveled the molecular mechanism of IRGQ action during autophagy-mediated degradation and quality control of MHC class I molecules, impacting T cell immunity.

Limitations of the study

Future studies will have to decipher the exact molecular basis for recognition of non-conformational MHC class I molecules by IRGQ. Ubiquitylation on K267 and K340 of MHC class I potentially marks HLA for IRGQ-mediated autophagy degradation by recruiting autophagy adaptor proteins.

IRGQ regulates protein levels of HLA molecules post translationally through autophagic degradation; nevertheless, an increase of HLA-A, -B, and -C mRNA is also observed in IRGQ-depleted cells and in IRGQ-low HCC samples. This is possibly due to a feedback loop, which further potentiates the effect of IRGQ on HLA levels.

Lastly, future studies are needed to better understand the role of (neo)antigen-specific activation of the cytotoxic T cell and the impact of unloaded and/or misfolded MHC class I molecules on T-cell-mediated anti-cancer immunity.

RESOURCE AVAILABILITY

Lead contact

Further information and requests for resources and reagents should be directed to and will be fulfilled by the lead contact, Ivan Dikic (dikic@biochem2.uni-frankfurt.de).

Materials availability

All reagents generated in this study are available from the lead contact with a completed materials transfer agreement.

Data and code availability

- All data reported in this paper will be shared by the lead contact upon request. The mass spectrometry proteomics data have been deposited to the ProteomeXchange Consortium via the PRIDE[66] partner repository with the dataset identifiers. PRIDE: PXD044618, PXD045117, PXD045212, and PXD045259. The crystal structures have been deposited to the PDB database: IRGQ (1-192)-GABARAPL2: PDB: 8Q6Q; LC3B-IRGQ LIR2 peptide: PDB: 8Q7K. Accession numbers are listed in the key resources table.
- This paper does not report original code.
- Any additional information required to reanalyze the data reported in this paper is available from the lead contact upon request.

ACKNOWLEDGMENTS

We thank Daniela Höller for critical reading of the manuscript. We acknowledge all members of the Quantitative Proteomics Unit at IBC2 (Goethe University, Frankfurt), in particular Thorsten Mosler and Georg Tascher, for support and expertise in proteomics methodology and data analysis, Martin Adrian-Allgood and Julia Pomirska for technical help and measurements, Kristina Wagner for preparing LC columns, and David Krause for help in (bio)informatics. We acknowledge Miljan Kuljanin for support and expertise in proteomics methodology and Steven Gygi for use of CORE for MS data analysis software. Moreover, we thank Blerina Aliraj for technical help with FACS and Yvonne Benatzy and Vanesa Guerrero Ruiz for preparing human macrophages. MC38-gp33 cells and Nur77eGFP × TCR327 mice were kindly provided by Dr. Hans Christian Probst (Institute for Immunology; University Medical Center Mainz). We thank the Deutsche Forschungsgemeinschaft (German Research Foundation, DFG) for funding the liquid chromatography (LC)-MS system (easy nLC1200, Orbitrap Fusion LUMOS) used in this study (FuGG Project-ID: 403765277). The research was funded by Dr. Rolf M. Schweite Stiftung to I.D. (project 13/2017), grants from the Goethe University Frankfurt to L.H. (Nachwuchswissenschaftler grant 710000624), and GRADE A/B Focus to L.H. (PID003790), as well as the LOEWE Zentrum Frankfurt Cancer Institute Discovery & Development Grant to L.H. (21001366). Additionally, this work was supported by the Clusterproject ENABLE funded by the Hessian Ministry for Science and the Arts to L.H. and A.W.; CRC project on selective autophagy, grant/award number: project-ID 259130777 to I.D., L.H., and A.W.; the Leistungszentrum Innovative Therapeutics (TheraNova) funded by the Fraunhofer Society and the Hessian Ministry of Science and Arts to I.D. and U.G.M.; Burroughs Wellcome Fund Career Award for Medical Scientists to J.D.M.; Hale Family Center for Pancreatic Cancer Research to J.D.M.; the Sidney Kimmel Foundation to J.D.M.; Jane Coffin Childs Fellowship to V.V.E.; and support from NIH grant RO1 NS083524 to J.W.H.

AUTHOR CONTRIBUTIONS

L.H., I.D., J.W.H., J.D.M., and V.V.E. conceived the study. L.H., I.D., J.D.L., J.D.M., V.V.E., T.B., A.W., and J.W.H. supervised experiments. L.H., U.G.-M., I.M., A.-C.J., C.P.-G., V.V.E., M.M., H.J.B., J.V., A.V.A., G.B., J.M., A.C.-P., I.B., J.Z., and R.M.B. designed/performed experiments and analyzed data. K.H., G.J.v.d.H.N., and A.G. generated tools for the experiments. L.H. and I.D. managed the project and wrote the manuscript with input from all authors.

(B) Representative contrast-enhanced magnetic resonance imaging (MRI) images of *c-Myc; Trp53Δ* and *c-Myc; Trp53Δ; IrgqΔ* mice at 27 and 41 days post plasmid injection. Arrows indicate tumors. Scale bar: 8 mm.
(C) Kaplan-Meier survival plot of *c-Myc; Trp53Δ* (Irgq WT) and *c-Myc; Trp53Δ; IrgqΔ* (Irgq KO) with HCC.
(D) Relative liver tumor area detected by MRI at day 27 post plasmid injection of WT and Irgq KO mice (*c-Myc; Trp53Δ* vs. *c-Myc; Trp53Δ; IrgqΔ*). Data are presented in a box-and-whisker plot.
(E) Same as (D), but assessing tumor numbers.
(F) Respective survival days of Irgq WT and KO mice treated with anti-CD8 antibody. CRISPR-Cas9 plasmid injection at day 0 and 5× injections of 200 μg of anti-CD8 antibody between days 13 and 21.
(G) FACS analysis of early apoptotic PA-TU-8988T WT and IRGQ KO cells upon co-culture with isolated primary human CD8+ T cells. Data are presented as the box-and-whisker plot and individual samples are color coded. $n = 3$.
(H–J) FACS analysis of (H) CD25+ FoxP3+ CD4+ T cells (Tregs), of (I) GrB+ or IFNγ+ CD8+ T cells, or of (J) CD279+ CD8+ T cells from the blood of *c-Myc*; *Trp53Δ* and *c-Myc; Trp53Δ; IrgqΔ* mice until 42 days post plasmid injection. Data are presented as the box-and-whisker plot and individual donors are color coded. Statistical significance of differences between experimental groups was assessed with Kruskal-Wallis-Test.
Data are presented as the mean with error bars indicating the SD. Statistical significance of differences between experimental groups was assessed with Student's t test. Differences with $p < 0.05$ are annotated as *; $p.< 0.01$ are annotated as **; $p < 0.001$ are annotated as ***.

DECLARATION OF INTERESTS

J.W.H. is a co-founder and consultant for Caraway Therapeutics (a subsidiary of Merck Inc) and is a scientific advisory board member for Lyterian Therapeutics.

STAR★METHODS

Detailed methods are provided in the online version of this paper and include the following:

- KEY RESOURCES TABLE
- EXPERIMENTAL MODEL AND STUDY PARTICIPANT DETAILS
  - Cell Culture
  - Isolation of PBMCs, T cells, and macrophages
  - Isolation of T cells from PBMCs
  - Isolation of human macrophages from PBMCs
  - PA-TU-8988T and human T cell co-culture
  - Purification of gp33-specific CD8+ T cells
  - Co-culture of gp33-specific CD+8 T Cells with MC38-gp33 cells
  - Hydrodynamic tail-vein injection
  - Isolation of mouse peripheral blood cells
  - Analysis of Human publicly available datasets
- METHOD DETAILS
  - Transfections of siRNA and plasmids
  - Cell lysis
  - Protein expression and purification
  - HDX mass spectrometry
  - X-Ray crystallography
  - Structure solution and refinement
  - Modeling IRGQ–hATG8 complexes
  - qRT-PCR
  - Immunofluorescence microscopy and live-cell imaging
  - Pulldowns and Immunoprecipitation
  - α^{P32}GTP binding assay
  - Antibodies
  - Cellular fractionation into soluble and insoluble fractions
  - EndoH/PNGase treatment
  - Cellular fractionation of organelles
  - Proximity ligation assay (PLA)
  - Lysosomal Immunoprecipitation
  - TMT total cell or lysosomal proteomics
  - SurfaceOME
  - Label-free quantitative interactome mass spectrometry
  - PTM MS-screen for Venus-IRGQ/HLA complexes
  - TMT 9-plex Total Liver Proteome
  - Native PAGE
  - Western blot
  - Cloning of plasmids for hydrodynamic tail-vein injection
  - Flow cytometry and intracellular cytokine staining
- QUANTIFICATION AND STATISTICAL ANALYSIS

SUPPLEMENTAL INFORMATION

Supplemental information can be found online at https://doi.org/10.1016/j.cell.2024.09.048.

Received: September 29, 2023
Revised: June 24, 2024
Accepted: September 29, 2024
Published: October 30, 2024

REFERENCES

1. Neefjes, J., Jongsma, M.L.M., Paul, P., and Bakke, O. (2011). Towards a systems understanding of MHC class I and MHC class II antigen presentation. Nat. Rev. Immunol. *11*, 823–836. https://doi.org/10.1038/NRI3084.
2. Bjorkman, P.J., and Parham, P. (1990). Structure, function, and diversity of class I major histocompatibility complex molecules. Annu. Rev. Biochem. *59*, 253–288. https://doi.org/10.1146/ANNUREV.BI.59.070190.001345.
3. Raghavan, M., Del Cid, N., Rizvi, S.M., and Peters, L.R. (2008). MHC class I assembly: out and about. Trends Immunol. *29*, 436–443. https://doi.org/10.1016/J.IT.2008.06.004.
4. Cresswell, P. (2005). Antigen processing and presentation. Immunol. Rev. *207*, 5–7. https://doi.org/10.1111/J.0105-2896.2005.00320.X.
5. Yamamoto, K., Venida, A., Yano, J., Biancur, D.E., Kakiuchi, M., Gupta, S., Sohn, A.S.W., Mukhopadhyay, S., Lin, E.Y., Parker, S.J., et al. (2020). Autophagy promotes immune evasion of pancreatic cancer by degrading MHC-I. Nature *581*, 100–105. https://doi.org/10.1038/S41586-020-2229-5.
6. Springer, S. (2015). Transport and quality control of MHC class I molecules in the early secretory pathway. Curr. Opin. Immunol. *34*, 83–90. https://doi.org/10.1016/J.COI.2015.02.009.
7. Gestal-Mato, U., and Herhaus, L. (2023). Autophagy-dependent regulation of MHC-I molecule presentation. J. Cell. Biochem. https://doi.org/10.1002/JCB.30416.
8. Montealegre, S., and van Endert, P.M. (2018). Endocytic Recycling of MHC Class I Molecules in Non-professional Antigen Presenting and Dendritic Cells. Front. Immunol. *9*, 3098. https://doi.org/10.3389/fimmu.2018.03098.
9. Weigert, A., and Herhaus, L. (2023). Immune modulation through secretory autophagy. J. Cell. Biochem. https://doi.org/10.1002/JCB.30427.
10. Dikic, I. (2017). Proteasomal and Autophagic Degradation Systems. Annu. Rev. Biochem. *86*, 193–224. https://doi.org/10.1146/annurev-biochem-061516-044908.
11. Dikic, I., and Elazar, Z. (2018). Mechanism and medical implications of mammalian autophagy. Nat. Rev. Mol. Cell Biol. *19*, 349–364. https://doi.org/10.1038/s41580-018-0003-4.
12. Mizushima, N. (2018). A brief history of autophagy from cell biology to physiology and disease. Nat. Cell Biol. *20*, 521–527. https://doi.org/10.1038/s41556-018-0092-5.
13. Deretic, V. (2021). Autophagy in inflammation, infection, and immunometabolism. Immunity *54*, 437–453. https://doi.org/10.1016/j.immuni.2021.01.018.
14. Levine, B., Mizushima, N., and Virgin, H.W. (2011). Autophagy in immunity and inflammation. Nature *469*, 323–335. https://doi.org/10.1038/nature09782.
15. Gatica, D., Lahiri, V., and Klionsky, D.J. (2018). Cargo recognition and degradation by selective autophagy. Nat. Cell Biol. *20*, 233–242. https://doi.org/10.1038/s41556-018-0037-z.
16. Lamark, T., and Johansen, T. (2021). Mechanisms of Selective Autophagy. Annu. Rev. Cell Dev. Biol. *37*, 143–169. https://doi.org/10.1146/annurev-cellbio-120219-035530.
17. Kim, B.H., Shenoy, A.R., Kumar, P., Bradfield, C.J., and MacMicking, J.D. (2012). IFN-inducible GTPases in host cell defense. Cell Host Microbe *12*, 432–444. https://doi.org/10.1016/J.CHOM.2012.09.007.
18. Bekpen, C., Hunn, J.P., Rohde, C., Parvanova, I., Guethlein, L., Dunn, D.M., Glowalla, E., Leptin, M., and Howard, J.C. (2005). The interferon-inducible p47 (IRG) GTPases in vertebrates: loss of the cell autonomous resistance mechanism in the human lineage. Genome Biol. *6*, R92. https://doi.org/10.1186/gb-2005-6-11-r92.
19. Li, J., Xu, X., Liu, J., Zhang, S., Wang, T., Liu, Y., and Wang, Z. (2023). The immunity-related GTPase IRGC mediates interaction between lipid droplets and mitochondria to facilitate sperm motility. FEBS Lett. *597*, 1595–1605. https://doi.org/10.1002/1873-3468.14640.
20. Kaneda, Y., Miyata, H., Shimada, K., Oyama, Y., Iida-Norita, R., and Ikawa, M. (2022). IRGC1, a testis-enriched immunity related GTPase, is important for fibrous sheath integrity and sperm motility in mice. Developmental Biology *488*, 104–113. https://doi.org/10.1016/j.ydbio.2022.05.011.

21. Nath, P., Jena, K.K., Mehto, S., Chauhan, N.R., Sahu, R., Dhar, K., Srinivas, K., Chauhan, S., and Chauhan, S. (2021). IRGM links autoimmunity to autophagy. Autophagy *17*, 578–580. https://doi.org/10.1080/15548627.2020.1810920.

22. Nabar, N.R., and Kehrl, J.H. (2019). Inflammasome Inhibition Links IRGM to Innate Immunity. Mol. Cell *73*, 391–392. https://doi.org/10.1016/j.molcel.2019.01.029.

23. Singh, S.B., Davis, A.S., Taylor, G.A., and Deretic, V. (2006). Human IRGM induces autophagy to eliminate intracellular mycobacteria. Science *313*, 1438–1441. https://doi.org/10.1126/science.1129577.

24. Eren, E., Planès, R., Bagayoko, S., Bordignon, P.J., Chaoui, K., Hessel, A., Santoni, K., Pinilla, M., Lagrange, B., Burlet-Schiltz, O., et al. (2020). Irgm2 and Gate-16 cooperatively dampen Gram-negative bacteria-induced caspase-11 response. EMBO Rep. *21*, e50829. https://doi.org/10.15252/EMBR.202050829.

25. Chauhan, S., Mandell, M.A., and Deretic, V. (2015). IRGM governs the core autophagy machinery to conduct antimicrobial defense. Mol. Cell *58*, 507–521. https://doi.org/10.1016/j.molcel.2015.03.020.

26. Singh, S.B., Ornatowski, W., Vergne, I., Naylor, J., Delgado, M., Roberts, E., Ponpuak, M., Master, S., Pilli, M., White, E., et al. (2010). Human IRGM regulates autophagy and cell-autonomous immunity functions through mitochondria. Nat. Cell Biol. *12*, 1154–1165. https://doi.org/10.1038/ncb2119.

27. Goswami, A.B., Karadarević, D., and Castaño-Rodríguez, N. (2022). Immunity-related GTPase IRGM at the intersection of autophagy, inflammation, and tumorigenesis. Inflamm. Res. *71*, 785–795. https://doi.org/10.1007/S00011-022-01595-X.

28. Kumar, S., Jain, A., Choi, S.W., da Silva, G.P.D., Allers, L., Mudd, M.H., Peters, R.S., Anonsen, J.H., Rusten, T.E., Lazarou, M., et al. (2020). Mammalian Atg8 proteins and the autophagy factor IRGM control mTOR and TFEB at a regulatory node critical for responses to pathogens. Nat. Cell Biol. *22*, 973–985. https://doi.org/10.1038/S41556-020-0549-1.

29. Mehto, S., Jena, K.K., Nath, P., Chauhan, S., Kolapalli, S.P., Das, S.K., Sahoo, P.K., Jain, A., Taylor, G.A., and Chauhan, S. (2019). The Crohn's Disease Risk Factor IRGM Limits NLRP3 Inflammasome Activation by Impeding Its Assembly and by Mediating Its Selective Autophagy. Mol. Cell *73*, 429–445.e7. https://doi.org/10.1016/J.MOLCEL.2018.11.018.

30. Bekpen, C., Xavier, R.J., and Eichler, E.E. (2010). Human IRGM gene "to be or not to be." Semin Immunopathol *32*, 437–444. https://doi.org/10.1007/s00281-010-0224-x.

31. Lin, G., Li, J., Chen, K., Wang, A., and Guo, C. (2022). Circ_0000854 regulates the progression of hepatocellular carcinoma through miR-1294 /IRGQ axis. Clin. Immunol. *238*, 109007. https://doi.org/10.1016/J.CLIM.2022.109007.

32. Molina-Sánchez, P., and Lujambio, A. (2019). Experimental Models for Preclinical Research in Hepatocellular Carcinoma (Humana Press) https://doi.org/10.1007/978-3-030-21540-8_16.

33. Yang, S., Wang, X., Contino, G., Liesa, M., Sahin, E., Ying, H., Bause, A., Li, Y., Stommel, J.M., Dell'Antonio, G., et al. (2011). Pancreatic cancers require autophagy for tumor growth. Genes Dev. *25*, 717–729. https://doi.org/10.1101/gad.2016111.

34. Abu-Remaileh, M., Wyant, G.A., Kim, C., Laqtom, N.N., Abbasi, M., Chan, S.H., Freinkman, E., and Sabatini, D.M. (2017). Lysosomal metabolomics reveals V-ATPase- and mTOR-dependent regulation of amino acid efflux from lysosomes. Science *358*, 807–813. https://doi.org/10.1126/science.aan6298.

35. Wyant, G.A., Abu-Remaileh, M., Wolfson, R.L., Chen, W.W., Freinkman, E., Danai, L.V., Vander Heiden, M.G., and Sabatini, D.M. (2017). mTORC1 Activator SLC38A9 Is Required to Efflux Essential Amino Acids from Lysosomes and Use Protein as a Nutrient. Cell *171*, 642–654.e12. https://doi.org/10.1016/j.cell.2017.09.046.

36. Davis, O.B., Shin, H.R., Lim, C.Y., Wu, E.Y., Kukurugya, M., Maher, C.F., Perera, R.M., Ordonez, M.P., and Zoncu, R. (2021). NPC1-mTORC1 Signaling Couples Cholesterol Sensing to Organelle Homeostasis and Is a Targetable Pathway in Niemann-Pick Type C. Dev. Cell *56*, 260–276.e7. https://doi.org/10.1016/J.DEVCEL.2020.11.016.

37. Gupta, S., Yano, J., Mercier, V., Htwe, H.H., Shin, H.R., Rademaker, G., Cakir, Z., Ituarte, T., Wen, K.W., Kim, G.E., et al. (2021). Lysosomal retargeting of Myoferlin mitigates membrane stress to enable pancreatic cancer growth. Nat. Cell Biol. *23*, 232–242. https://doi.org/10.1038/S41556-021-00644-7.

38. Galluzzi, L., Baehrecke, E.H., Ballabio, A., Boya, P., Bravo-San Pedro, J.M., Cecconi, F., Choi, A.M., Chu, C.T., Codogno, P., Colombo, M.I., et al. (2017). Molecular definitions of autophagy and related processes. EMBO J. *36*, 1811–1836. https://doi.org/10.15252/embj.201796697.

39. Nguyen, T.N., Padman, B.S., Usher, J., Oorschot, V., Ramm, G., and Lazarou, M. (2016). Atg8 family LC3/GAB ARAP proteins are crucial for autophagosome-lysosome fusion but not autophagosome formation during PINK1/Parkin mitophagy and starvation. J. Cell Biol. *215*, 857–874. https://doi.org/10.1083/jcb.201607039.

40. Chino, H., Hatta, T., Natsume, T., and Mizushima, N. (2019). Intrinsically Disordered Protein TEX264 Mediates ER-phagy. Mol. Cell *74*, 909–921.e6. https://doi.org/10.1016/j.molcel.2019.03.033.

41. Eck, F., Phuyal, S., Smith, M.D., Kaulich, M., Wilkinson, S., Farhan, H., and Behrends, C. (2020). ACSL3 is a novel GABARAPL2 interactor that links ufmylation and lipid droplet biogenesis. J. Cell Sci. *133*, jcs243477. https://doi.org/10.1242/jcs.243477.

42. Kalvari, I., Tsompanis, S., Mulakkal, N.C., Osgood, R., Johansen, T., Nezis, I.P., and Promponas, V.J. (2014). iLIR: A web resource for prediction of Atg8-family interacting proteins. Autophagy *10*, 913–925. https://doi.org/10.4161/auto.28260.

43. Birgisdottir, Å.B., Lamark, T., and Johansen, T. (2013). The LIR motif - crucial for selective autophagy. J. Cell Sci. *126*, 3237–3247. https://doi.org/10.1242/jcs.126128.

44. Kumar, S., Jain, A., Farzam, F., Jia, J., Gu, Y., Choi, S.W., Mudd, M.H., Claude-Taupin, A., Wester, M.J., Lidke, K.A., et al. (2018). Mechanism of Stx17 recruitment to autophagosomes via IRGM and mammalian Atg8 proteins. J. Cell Biol. *217*, 997–1013. https://doi.org/10.1083/JCB.201708039.

45. Croucher, D.R., Iconomou, M., Hastings, J.F., Kennedy, S.P., Han, J.Z.R., Shearer, R.F., McKenna, J., Wan, A., Lau, J., Aparicio, S., et al. (2016). Bimolecular complementation affinity purification (BiCAP) reveals dimer-specific protein interactions for ERBB2 dimers. Sci. Signal. *9*, ra69. https://doi.org/10.1126/scisignal.aaf0793.

46. Hughes, E.A., Hammond, C., and Cresswell, P. (1997). Misfolded major histocompatibility complex class I heavy chains are translocated into the cytoplasm and degraded by the proteasome. Proc. Natl. Acad. Sci. USA *94*, 1896–1901. https://doi.org/10.1073/PNAS.94.5.1896.

47. Vassilakos, A., Cohen-Doyle, M.F., Peterson, P.A., Jackson, M.R., and Williams, D.B. (1996). The molecular chaperone calnexin facilitates folding and assembly of class I histocompatibility molecules. EMBO J. *15*, 1495–1506. https://doi.org/10.1002/j.1460-2075.1996.tb00493.x.

48. Schuren, A.B.C., Boer, I.G.J., Bouma, E.M., Van de Weijer, M.L., Costa, A.I., Hubel, P., Pichlmair, A., Lebbink, R.J., and Wiertz, E.J.H.J. (2021). The UFM1 Pathway Impacts HCMV US2-Mediated Degradation of HLA Class I. Molecules *26*, 287. https://doi.org/10.3390/MOLECULES26020287.

49. Wei, J., Zanker, D., Di Carluccio, A.R., Smelkinson, M.G., Takeda, K., Seedhom, M.O., Dersh, D., Gibbs, J.S., Yang, N., Jadhav, A., et al. (2017). Varied Role of Ubiquitylation in Generating MHC Class I Peptide Ligands. J. Immunol. *198*, 3835–3845. https://doi.org/10.4049/JIMMUNOL.1602122.

50. Loi, M., Müller, A., Steinbach, K., Niven, J., Barreira da Silva, R., Paul, P., Ligeon, L.A., Caruso, A., Albrecht, R.A., Becker, A.C., et al. (2016). Macroautophagy Proteins Control MHC Class I Levels on Dendritic Cells and Shape Anti-viral CD8(+) T Cell Responses. Cell Rep. *15*, 1076–1087. https://doi.org/10.1016/J.CELREP.2016.04.002.

51. Chen, X., and Calvisi, D.F. (2014). Hydrodynamic transfection for generation of novel mouse models for liver cancer research. Am. J. Pathol. *184*, 912–923. https://doi.org/10.1016/j.ajpath.2013.12.002.

52. Ruiz de Galarreta, M.R., Bresnahan, E., Molina-Sánchez, P., Lindblad, K.E., Maier, B., Sia, D., Puigvehi, M., Miguela, V., Casanova-Acebes, M., Dhainaut, M., et al. (2019). β-Catenin Activation Promotes Immune Escape and Resistance to Anti-PD-1 Therapy in Hepatocellular Carcinoma. Cancer Discov. *9*, 1124–1141. https://doi.org/10.1158/2159-8290.CD-19-0074.

53. Leung, C.O.N., Yang, Y., Leung, R.W.H., So, K.K.H., Guo, H.J., Lei, M.M.L., Muliawan, G.K., Gao, Y., Yu, Q.Q., Yun, J.P., et al. (2023). Broad-spectrum kinome profiling identifies CDK6 upregulation as a driver of lenvatinib resistance in hepatocellular carcinoma. Nat. Commun. *14*, 6699. https://doi.org/10.1038/S41467-023-42360-W.

54. Chen, D., Wang, J., Li, Y., Xu, C., Fanzheng, M., Zhang, P., and Liu, L. (2023). LncRNA NEAT1 suppresses cellular senescence in hepatocellular carcinoma via KIF11-dependent repression of CDKN2A. Clin. Transl. Med. *13*, e1418. https://doi.org/10.1002/CTM2.1418.

55. Wu, Y., Liu, Z., and Xu, X. (2020). Molecular subtyping of hepatocellular carcinoma: A step toward precision medicine. Cancer Commun. *40*, 681–693. https://doi.org/10.1002/CAC2.12115.

56. Geng, J., and Raghavan, M. (2021). Conformational sensing of major histocompatibility complex (MHC) class I molecules by immune receptors and intracellular assembly factors. Curr. Opin. Immunol. *70*, 67–74. https://doi.org/10.1016/J.COI.2021.03.014.

57. Geng, J., Altman, J.D., Krishnakumar, S., and Raghavan, M. (2018). Empty conformers of HLA-B preferentially bind CD8 and regulate CD8+ T cell function. eLife *7*, e36341. https://doi.org/10.7554/eLife.36341.

58. Moran, A.E., Holzapfel, K.L., Xing, Y., Cunningham, N.R., Maltzman, J.S., Punt, J., and Hogquist, K.A. (2011). T cell receptor signal strength in Treg and iNKT cell development demonstrated by a novel fluorescent reporter mouse. J. Exp. Med. *208*, 1279–1289. https://doi.org/10.1084/JEM.20110308.

59. Jiang, Y., Li, Y., and Zhu, B. (2015). T-cell exhaustion in the tumor microenvironment. Cell Death Dis. *6*, e1792. https://doi.org/10.1038/cddis.2015.162.

60. Dhatchinamoorthy, K., Colbert, J.D., and Rock, K.L. (2021). Cancer Immune Evasion Through Loss of MHC Class I Antigen Presentation. Front. Immunol. *12*, 636568. https://doi.org/10.3389/FIMMU.2021.636568/BIBTEX.

61. Van Eyndhoven, L.C., and Tel, J. (2022). Revising immune cell coordination: origins and importance of single-cell variation. Eur. J. Immunol. *52*, 1889–1897. https://doi.org/10.1002/EJI.202250073.

62. Uhl, M., Kepp, O., Jusforgues-Saklani, H., Vicencio, J.M., Kroemer, G., and Albert, M.L. (2009). Autophagy within the antigen donor cell facilitates efficient antigen cross-priming of virus-specific CD8+ T cells. Cell Death Differ. *16*, 991–1005. https://doi.org/10.1038/CDD.2009.8.

63. Parekh, V.V., Pabbisetty, S.K., Wu, L., Sebzda, E., Martinez, J., Zhang, J., and Van Kaer, L. (2017). Autophagy-related protein Vps34 controls the homeostasis and function of antigen cross-presenting CD8α+ dendritic cells. Proc. Natl. Acad. Sci. USA *114*, E6371–E6380. https://doi.org/10.1073/PNAS.1706504114.

64. Xu, F., Jin, T., Zhu, Y., and Dai, C. (2018). Immune checkpoint therapy in liver cancer. J. Exp. Clin. Cancer Res. *37*, 110. https://doi.org/10.1186/s13046-018-0777-4.

65. Waldman, A.D., Fritz, J.M., and Lenardo, M.J. (2020). A guide to cancer immunotherapy: from T cell basic science to clinical practice. Nat. Rev. Immunol. *20*, 651–668. https://doi.org/10.1038/s41577-020-0306-5.

66. Perez-Riverol, Y., Bai, J., Bandla, C., García-Seisdedos, D., Hewapathirana, S., Kamatchinathan, S., Kundu, D.J., Prakash, A., Frericks-Zipper, A., Eisenacher, M., et al. (2022). The PRIDE database resources in 2022: a hub for mass spectrometry-based proteomics evidences. Nucleic Acids Res. *50*, D543–D552. https://doi.org/10.1093/NAR/GKAB1038.

67. Grumati, P., Morozzi, G., Hölper, S., Mari, M., Harwardt, M.I., Yan, R., Müller, S., Reggiori, F., Heilemann, M., and Dikic, I. (2017). Full length RTN3 regulates turnover of tubular endoplasmic reticulum via selective autophagy. eLife *6*, e25555. https://doi.org/10.7554/eLife.25555.

68. Karplus, P.A., and Diederichs, K. (2015). Assessing and maximizing data quality in macromolecular crystallography. Curr. Opin. Struct. Biol. *34*, 60–68. https://doi.org/10.1016/J.SBI.2015.07.003.

69. Kampstra, P. (2008). Beanplot: A Boxplot Alternative for Visual Comparison of Distributions. J. Stat. Soft. *28*, 1–9. https://doi.org/10.18637/JSS.V028.C01.

70. Nagy, Á., Lánczky, A., Menyhárt, O., and Győrffy, B. (2018). Validation of miRNA prognostic power in hepatocellular carcinoma using expression data of independent datasets. Sci. Rep. *8*, 9227. https://doi.org/10.1038/S41598-018-27521-Y.

71. Tang, Z., Li, C., Kang, B., Gao, G., Li, C., and Zhang, Z. (2017). GEPIA: a web server for cancer and normal gene expression profiling and interactive analyses. Nucleic Acids Res. *45*, W98–W102. https://doi.org/10.1093/NAR/GKX247.

72. Goldman, M.J., Craft, B., Hastie, M., Repečka, K., McDade, F., Kamath, A., Banerjee, A., Luo, Y., Rogers, D., Brooks, A.N., et al. (2020). Visualizing and interpreting cancer genomics data via the Xena platform. Nat. Biotechnol. *38*, 675–678. https://doi.org/10.1038/S41587-020-0546-8.

73. NIH. cProSite - Cancer Proteogenomic Data Analysis Site. https://cprosite.ccr.cancer.gov/.

74. Herhaus, L., Bhaskara, R.M., Håkon Lystad, A., Simonsen, A., Hummer, G., and Dikic, I. (2020). TBK1-mediated phosphorylation of LC3C and GABARAP-L2 controls autophagosome shedding by ATG4 protease. EMBO Rep. *21*, e48317. https://doi.org/10.15252/embr.201948317.

75. Herhaus, L., Perez-Oliva, A.B., Cozza, G., Gourlay, R., Weidlich, S., Campbell, D.G., Pinna, L.A., and Sapkota, G.P. (2015). Casein kinase 2 (CK2) phosphorylates the deubiquitylase OTUB1 at Ser16 to trigger its nuclear localization https://doi.org/10.1126/scisignal.aaa0441.

76. Eisinger, M.L., Dörrbaum, A.R., Michel, H., Padan, E., and Langer, J.D. (2017). Ligand-induced conformational dynamics of the Escherichia coli Na+/H+ antiporter NhaA revealed by hydrogen/deuterium exchange mass spectrometry. Proc. Natl. Acad. Sci. USA *114*, 11691–11696. https://doi.org/10.1073/PNAS.1703422114.

77. Pettersen, E.F., Goddard, T.D., Huang, C.C., Couch, G.S., Greenblatt, D.M., Meng, E.C., and Ferrin, T.E. (2004). UCSF Chimera–a visualization system for exploratory research and analysis. J. Comput. Chem. *25*, 1605–1612. https://doi.org/10.1002/JCC.20084.

78. Kabsch, W. (2010). XDS. Acta Crystallogr. D Biol. Crystallogr. *66*, 125–132. https://doi.org/10.1107/S0907444909047337.

79. Evans, P.R., and Murshudov, G.N. (2013). How good are my data and what is the resolution? Acta Crystallogr. D Biol. Crystallogr. *69*, 1204–1214. https://doi.org/10.1107/S0907444913000061.

80. Potterton, L., Agirre, J., Ballard, C., Cowtan, K., Dodson, E., Evans, P.R., Jenkins, H.T., Keegan, R., Krissinel, E., Stevenson, K., et al. (2018). CCP4i2: The new graphical user interface to the CCP4 program suite. Acta Crystallogr. D Struct. Biol. *74*, 68–84. https://doi.org/10.1107/S2059798317016035.

81. Emsley, P., Lohkamp, B., Scott, W.G., and Cowtan, K. (2010). Features and development of Coot. Acta Crystallogr. D Biol. Crystallogr. *66*, 486–501. https://doi.org/10.1107/S0907444910007493.

82. Liebschner, D., Afonine, P.V., Baker, M.L., Bunkóczi, G., Chen, V.B., Croll, T.I., Hintze, B., Hung, L.W., Jain, S., McCoy, A.J., et al. (2019). Macromolecular structure determination using X-rays, neutrons and electrons: recent developments in Phenix. Acta Crystallogr. D Struct. Biol. *75*, 861–877. https://doi.org/10.1107/S2059798319011471.

83. Jumper, J., Evans, R., Pritzel, A., Green, T., Figurnov, M., Ronneberger, O., Tunyasuvunakool, K., Bates, R., Žídek, A., Potapenko, A., et al. (2021). Highly accurate protein structure prediction with AlphaFold. Nature *7873*, 583–589. https://doi.org/10.1038/s41586-021-03819-2.

84. Herhaus, L., Al-Salihi, M., MacArtney, T., Weidlich, S., and Sapkota, G.P. (2013). OTUB1 enhances TGFβ signalling by inhibiting the ubiquitylation and degradation of active SMAD2/3. Nat. Commun. *4*, 2519. https://doi.org/10.1038/ncomms3519.

85. Herhaus, L., Al-Salihi, M.A., Dingwell, K.S., Cummins, T.D., Wasmus, L., Vogt, J., Ewan, R., Bruce, D., Macartney, T., Weidlich, S., et al. (2014). USP15 targets ALK3/BMPR1A for deubiquitylation to enhance bone morphogenetic protein signalling. Open Biol. *4*, 140065. https://doi.org/10.1098/rsob.140065.

86. Wieckowski, M.R.M.R., Giorgi, C., Lebiedzinska, M., Duszynski, J., and Pinton, P. (2009). Isolation of mitochondria-associated membranes and mitochondria from animal tissues and cells. Nat. Protoc. *4*, 1582–1590. https://doi.org/10.1038/NPROT.2009.151.

87. Eapen, V.V., Swarup, S., Hoyer, M.J., Paulo, J.A., and Harper, J.W. (2021). Quantitative proteomics reveals the selectivity of ubiquitin-binding autophagy receptors in the turnover of damaged lysosomes by lysophagy. eLife *10*, e72328. https://doi.org/10.7554/eLife.72328.

88. McAlister, G.C., Nusinow, D.P., Jedrychowski, M.P., Wühr, M., Huttlin, E.L., Erickson, B.K., Rad, R., Haas, W., and Gygi, S.P. (2014). MultiNotch MS3 enables accurate, sensitive, and multiplexed detection of differential expression across cancer cell line proteomes. Anal. Chem. *86*, 7150–7158. https://doi.org/10.1021/AC502040V.

89. Ordureau, A., Paulo, J.A., Zhang, J., An, H., Swatek, K.N., Cannon, J.R., Wan, Q., Komander, D., and Harper, J.W. (2020). Global Landscape and Dynamics of Parkin and USP30-Dependent Ubiquitylomes in iNeurons during Mitophagic Signaling. Mol. Cell *77*, 1124–1142.e10. https://doi.org/10.1016/j.molcel.2019.11.013.

90. Huttlin, E.L., Jedrychowski, M.P., Elias, J.E., Goswami, T., Rad, R., Beausoleil, S.A., Villén, J., Haas, W., Sowa, M.E., and Gygi, S.P. (2010). A tissue-specific atlas of mouse protein phosphorylation and expression. Cell *143*, 1174–1189. https://doi.org/10.1016/j.cell.2010.12.001.

91. Covarrubias-Pinto, A., Acuña, A.I., Boncompain, G., Papic, E., Burgos, P.V., Perez, F., and Castro, M.A. (2018). Ascorbic acid increases SVCT2 localization at the plasma membrane by accelerating its trafficking from early secretory compartments and through the endocytic-recycling pathway. Free Radic. Biol. Med. *120*, 181–191. https://doi.org/10.1016/J.FREERADBIOMED.2018.03.013.

92. Zuckermann, M., Hlevnjak, M., Yazdanparast, H., Zapatka, M., Jones, D.T.W., Lichter, P., and Gronych, J. (2018). A novel cloning strategy for one-step assembly of multiplex CRISPR vectors. Sci. Rep. *8*, 17499. https://doi.org/10.1038/S41598-018-35727-3.

93. Ashkenazy, H., Abadi, S., Martz, E., Chay, O., Mayrose, I., Pupko, T., and Ben-Tal, N. (2016). ConSurf 2016: an improved methodology to estimate and visualize evolutionary conservation in macromolecules. Nucleic Acids Res. *44*, W344–W350. https://doi.org/10.1093/NAR/GKW408.

STAR★METHODS

KEY RESOURCES TABLE

REAGENT or RESOURCE	SOURCE	IDENTIFIER
Antibodies		
Alexa Fluor® 700 anti-human CD45 Antibody	BioLegend	Cat#304024; RRID:AB_493761
APC anti-mouse CD137 Antibody	BioLegend	Cat#106110; RRID:AB_2564297
APC/Fire™ 750 anti-human HLA-DR Antibody	BioLegend	Cat#307658; RRID:AB_2572101
APC/Fire™ 750 anti-mouse CD19 Antibody	BioLegend	Cat#115558; RRID:AB_2572120
BD Horizon™ BV421 Mouse Anti-Human HLA-ABC	BD Biosciences	Cat#565332; RRID:AB_2739189
BD Horizon™ BV711 Rat Anti-Mouse CD4	BD Biosciences	Cat#563050; RRID:AB_2737973
BD Horizon™ BV421 Rat Anti-Mouse IFN-γ	BD Biosciences	Cat#563376; RRID:AB_2738165
BD Horizon™ BUV395 Rat Anti-Mouse CD8a	BD Biosciences	Cat#565968; RRID:AB_ 2739421
BD Horizon™ BUV805 Mouse Anti-Human CD3	BD Biosciences	Cat#612893; RRID:AB_2870181
BD Horizon™ PE-CF594 Hamster Anti-Mouse CD3e	BD Biosciences	Cat#562286; RRID:AB_11153307
BD OptiBuild™ BV650 Mouse Anti-Mouse CD366 (TIM-3)	BD Biosciences	Cat#747623; RRID:AB_2744189
BD OptiBuild™ BV786 Rat Anti-Mouse CD279 (PD-1)	BD Biosciences	Cat#748264; RRID:AB_2872692
BD OptiBuild™ BUV737 Rat Anti-Mouse CD223	BD Biosciences	Cat#741820; RRID:AB_2871155
BD Pharmingen™ Alexa Fluor® 700 Rat Anti-Mouse CD45	BD Biosciences	Cat#560510; RRID:AB_1645208
BD Pharmingen™ PE-Cy™5 Rat Anti-Mouse CD44	BD Biosciences	Cat#553135; RRID:AB_394650
Brilliant Violet 605™ anti-mouse/human CD11b Antibody	BioLegend	Cat#101257; RRID:AB_11126744
FITC anti-human/mouse Granzyme B Antibody	BioLegend	Cat#515403; RRID:AB_2114575
FOXP3 Monoclonal Antibody (FJK-16s), PE, eBioscience™	invitrogen	Cat#12-5773-82; RRID:AB_465936
PE/Cyanine7 anti-mouse CD25 Antibody	BioLegend	Cat#102016; RRID:AB_312865
PerCP/Cyanine5.5 anti-mouse CD62L Antibody	BioLegend	Cat#104432; RRID:AB_2285839
anti-IRGQ	Sigma-Aldrich	Cat#HPA043254; RRID:AB_10794178
*InVivo*MAb anti-mouse CD8α, clone 2.43	BioXcell	Cat#BE0061; RRID:AB_1125541
anti-HA-tag	Roche	Cat#11867423001; RRID:AB_390918
anti-vinculin	Sigma-Aldrich	Cat#V4505; RRID:AB_477617
anti-LC3B	MBL	Cat#PMO36
anti-Lamp1	Abcam	Cat#Ab24170; RRID:AB_775978
anti-REEP5	Santa Cruz Biotechnology	Cat#sc-393508
anti-HLA-ABC-I	Proteintech	Cat#15240-1-AP; RRID:AB_1557426
anti-HLA W6/32	Sigma-Aldrich	Cat#MABN1783
anti-B2M	Proteintech	Cat#13511-1-AP; RRID:AB_2062735
anti-HLA HC10	Nordic MUbio	Cat#MUB2037P

(*Continued on next page*)

Continued

REAGENT or RESOURCE	SOURCE	IDENTIFIER
anti-FlagM2-tag	Sigma-Aldrich	Cat#F3165; RRID:AB_259529
anti-GFP- tag	Clontech	Living Colors Cat#632592; RRID:AB_2336883
anti-His-tag	Roche	Cat#11922416001; RRID:AB_514486
anti-tubulin	Sigma-Aldrich	Cat#T9026; RRID:AB_477593
anti-GAPDH	Cell Signaling Technology	Cat#2118; RRID:AB_561053
anti-VDAC	Proteintech	Cat#55259-1-AP; RRID:AB_10837225
anti-EGFR	Cell Signaling Technology	Cat#2232; RRID:AB_331707
anti-GABARAPL2	MBL	Cat#PM038; RRID:AB_10210502
anti-LAMP1	DSHB	Cat#H4A3; RRID:AB_626853
anti-p62	MBL	Cat#M162-3; RRID:AB_1279299
anti-PARP	Cell Signaling Technology	Cat#9542; RRID:AB_2160739
anti-Histone H2A	Abcam	Cat#Ab18255; RRID:AB_470265
anti-Histone H3	Cell Signaling Technology	Cat#9715; RRID:AB_331563
anti-IRGM	Abcam	Cat#Ab69494; RRID:AB_1209373
anti-pSTAT1	Cell Signaling Technology	Cat#7649; RRID:AB_10950970
goat anti-mouse (HRP)	Santa Cruz Biotechnology	Cat#sc-2031; RRID:AB_631737
goat anti-rabbit (HRP)	Santa Cruz Biotechnology	Cat#sc-2030; RRID:AB_631747
goat anti-rat (HRP)	Santa Cruz Biotechnology	Cat#sc-2006; RRID:AB_1125219
Anti-rat Alexa Fluor 647	Life Technologies	Cat#A-21247; RRID:AB_141778
anti-rat Cy3	Jackson Lab	Cat#712166153; RRID:AB_2340669
anti- mouse Alexa Fluor 405	Life Technologies	Cat#A-31553; RRID:AB_221604
anti-mouse Cy3	Dianova	Cat#715-165-151; RRID:AB_2315777
anti-rabbit Alexa647	Life Technologies	Cat#A21244; RRID:AB_2535812
anti-mouse Alexa 647	Life Technologies	Cat#A-31626
Bacterial and virus strains		
NEB Turbo competent E.coli	NEB	Cat#C2984H
Biological samples		
Buffy coats	DRK-Blutspendedienst Baden-Württemberg-Hessen, Institut für Transfusionsmedizin und Immunhämatologie, Frankfurt, Germany	N/A
Chemicals, peptides, and recombinant proteins		
2-Mercaptoethanol	gibco	Cat#31350-010
Albumin Fraction V (BSA)	Carl Roth	Cat#7076.3
Dulbecco's Phosphate Buffered Saline (PBS)	Sigma-Aldrich	Cat#D5652-10L
Fetal Bovine Serum (FBS)	Capricorn Scientific	Cat#FBS-11A
HEPES solution	Sigma Life Science	Cat#H0887
Human Plasma	DRK-Blutspendedienst Baden-Württemberg-Hessen, Institut für Transfusionsmedizin und Immunhämatologie, Frankfurt, Germany	N/A
MEM Non-essential Amino Acid Solution	Sigma Life Science	Cat#M7145
Pancoll	Pan Biotech GmbH	Cat#P04-60500
Penicillin-Streptamycin	Sigma-Aldrich	Cat#P4333
RPMI Medium 1640 + GlutaMax™	gibco	Cat#61870-010
Sodium pyruvate solution	Sigma Life Science	Cat#S8636
Tetanus toxin from *Clostridium tetani*	Sigma-Aldrich/Merck	Cat#T3194

(*Continued on next page*)

Continued

REAGENT or RESOURCE	SOURCE	IDENTIFIER
Trypsin–EDTA Solution	Sigma Life Science	Cat#T4147
IRGQ-LIR2 peptide: (EDETWEVLE)	this paper	N/A
Deuterium oxide	Carl Roth	CAS number: 7789-20-0
IRGQ(1-192)-GABARAPL2(1-117) complex	this paper	N/A
Imidazole	Sigma-Aldrich/Merck	Cat#I5513
TCEP	Sigma-Aldrich/Merck	Cat#C4706
Glycerol	Fischer Chemical	Cat#G/0650/17
NaCl	Carl Roth	Cat#3957.2
PEG 3000	Molecular Dimensions	Cat#MD2-250-8
Tri-Sodium citrate	Molecular Dimensions	Cat#133128
Ethylene glycol	Molecular Dimensions	Cat#MD2-100-60
Gadoxetic acid contrast agent	Bayer-Schering pharma	Primovist®
DMEM, high glucose	Thermo Fisher Scientific (Gibco)	Cat#41965-039
IMDM	Thermo Fisher Scientific (Gibco)	Cat#21980032
EBSS	Thermo Fisher Scientific (Gibco)	Cat#24010043
Human IFNγ	Reprotech	Cat#AF-300-02
Torin-1	Tocris	Cat#4247
Bafilomycin A1	LC Laboratories/Biotrend	Cat#B-1080
MG132	MedChemExpress	Cat#HY-13259
Cycloheximide	Sigma-Aldrich/Merck	Cat#C4859-1ML
GeneJuice® Transfection Reagent	Merck Millipore	Cat#70967-6
TurboFect	Thermo Fisher Scientific	Cat#R0531
Opti-MEM	Thermo Fisher Scientific (Gibco)	Cat#31985062
Lipofectamine™ RNAiMAX Transfection Reagent	Thermo Fisher Scientific	Cat#13778150
Tris	Roth	Cat#AE15.2
EDTA	Fluka Analytical	Cat#34549-1KG
Triton® X 100	Roth	Cat#3051.2
Protease Inhibitors	Roche	Cat#4693132001
Phosphatase Inhibitors	Sigma-Aldrich	Cat#P5726, Cat#P0044
SDS Pellets	Roth	Cat#CN30.2
Benzonase® Nuclease HC, Purity > 90%	Millipore	Cat#71205-3
Saponin	Sigma-Aldrich	Cat#47036
LysoTracker Red DND-99	Thermo Fisher Scientific	Cat#L7528
Myc-agarose beads	Thermo Fisher Scientific	Cat#20169
Flag-M2 agarose beads	Sigma-Aldrich	Cat#A2220
Streptavidin-dynabeads	Thermo Fisher Scientific	Cat#65605D
RFP-Trap_A beads	ChromoTek	Cat#rta-10
GFP- Trap_A beads	ChromoTek	Cat#gta-10
aP32GTP	Hartmann Analytic	Cat#SRP-108
PNGase F	NEB	Cat#P0704S
Endo Hf	NEB	Cat#P0703S
Sulfo-NHS-LC-Biotin	Thermo Fisher Scientific	Cat#21335
NeutrAvidin Protein beads	Thermo Fisher Scientific	Cat#29200
NuPAGE™ LDS Sample Buffer	Thermo Fisher Scientific	Cat#NP0007
4-20% Mini-PROTEAN® TGX Stain-Free™ Protein Gels	BioRad	Cat#456-8094

(*Continued on next page*)

Continued

REAGENT or RESOURCE	SOURCE	IDENTIFIER
Critical commercial assays		
7-AAD	BD Biosciences	Cat#51-68981E
BD Horizon™ Brilliant Stain Buffer	BD Biosciences	Cat#566349
EasySep™ Human CD8+ T Cell Isolation Kit	STEMCELL Technologies	Cat#17953
EasySep™ Human T Cell Isolation Kit	STEMCELL Technologies	Cat#17951
eBioscience™ FOXP3/Transcription Factor Staining Buffer Set	invitrogen	Cat#00-5523-00
FACSFlow™ Sheath Fluid	BD Biosciences	Cat#342003
FcR Blocking Reagent human	Miltenyi Biotec	Cat#130-059-901
FcR Blocking Reagent mouse	Miltenyi Biotec	Cat#130-092-575
Flow Cytometry Absolute Count Standard™	Bangs Laboratories	Cat#580
HiPerFect® Transfection Reagent	QIAGEN	Cat# 301707
Zombie UV™ Fixable Viability Kit	BioLegend	Cat#423107
plasmid PlusMega kit	Qiagen	Cat#12941
RNeasy Mini Kit	Qiagen	Cat#74104
RNase-Free DNase Set	Qiagen	Cat#79254
iScript™ cDNA Synthesis Kit	BioRad	Cat#170-8891
LightCycler 480 SYBR Green I Master	Roche	Cat#04707516001
PLA Duolink® In Situ Detection Reagents	Sigma-Aldrich	Cat#DUO92014
Duolink® In Situ PLA® Probe Anti-Rabbit PLUS	Sigma-Aldrich	Cat#DUO92002
Duolink® In Situ PLA® Probe Anti-Mouse MINUS	Sigma-Aldrich	Cat#DUO92004
TMT10plex™ Isobaric Label Reagent Set, 1 x 0.8 mg	Thermo Fisher Scientific	Cat#90110
SepPak tC18 columns	Waters	Cat#WAT054955
micro BCA	Thermo Fisher Scientific	Cat#23235
Luminol Reagent	Santa Cruz Biotechnology	Cat#sc-2048
Deposited data		
HDX-MS raw data of IRGQ: GABARAPL2 and LC3B	this study	PRIDE: PXD045212
Whole-cell and lysosomal proteomics from 8998T cells	this study	PRIDE: PXD044618
Crystallography data IRGQ(1-192)-GABARAPL2(1-117) complex	this study	PDB: 8Q6Q
Crystallography data IRGQ LIR2 peptide-LC3B complex	this study	PDB: 8Q7K
Experimental models: Cell lines		
PA-TU-8988T	DSMZ	ACC 162
PA-TU-8988T ATG5-/-	This study	N/A
PA-TU-8988T FIP200-/-	This study	N/A
PA-TU-8988T IRGQ-/-	This study	N/A
HeLa	DSMZ	ACC 57
HEK293T	ATCC	CRL-3216
Huh-7	Cellosaurus	CVCL_0336
U2OS	ATCC	HTB-96
HCT116	ATCC	CCL-247
SK-N-AS1	ATCC	CRL-2137

(*Continued on next page*)

Continued

REAGENT or RESOURCE	SOURCE	IDENTIFIER
Experimental models: Organisms/strains		
C57BL/6J	Jackson Laboratories	Strain #:000664 RRID:IMSR_JAX:000664
Oligonucleotides		
ATG5 gRNA	IDT	GGCCATCAATCGGAAACTCA
IRGQ gRNA	IDT	ACGGTCCAGAGCACCACATT
FIP200 gRNA	IDT	CTGGTTAGGCACTCCAACAG
mTp53-1	IDT	CCTCGAGCTCCCTCTGAGCC
mTp53-2	IDT	GTGTAATAGCTCCTGCATGG
mIrgq-1	IDT	CCAGGGCGAAGATCCACCCG
mIrgq-2	IDT	GACACGGTAGAGATTCCCGA
gIRGQ#1	IDT	TTTGTGCTACCGGCGAACTG
gIRGQ#2	IDT	GAATGCACTCAGTAAGGGAA
gIRGQ#3	IDT	CGTGAGGCCTTTGAGACCGG
gGABARAPL2#1	IDT	GTCGAGCGAAATATCCCGACA
gGABARAPL2#2	IDT	GTCCCACAGAACACAGATGCG
gGABARAPL2#3	IDT	GGTTCCATCTGATATCACTG
Recombinant DNA		
IRGQ(1-192)-GABARAPL2(1-117) in pRSFDuet-1 vector	this paper	N/A
IRGQ (1-623) in pGEX6P1 vector	this paper	N/A
LC3B in pGEX4T1 vector	this paper	N/A
GABARAPL2 in pGEX4T1 vector	this paper	N/A
pX330-gRNA	pX330-gRNA was a gift from Charles P. Lai.	Addgene plasmid # 158973; http://n2t.net/addgene:158973; RRID:Addgene_158973)
PX330-sg-Tp53-sg-Irgq	this paper	N/A
PX330-sg-Tp53	this paper	N/A
c-myc-PT3EF1	c-myc-PT3EF1a was a gift from Xin Chen	Addgene plasmid # 92046; http://n2t.net/addgene:92046; RRID:Addgene_92046
SB100X	SB100X was a gift from Mark Groudine	Addgene plasmid # 127909; http://n2t.net/addgene:127909; RRID:Addgene_127909
Software and algorithms		
FlowJo	BD	https://www.flowjo.com/solutions/flowjo
R	R Foundation	https://www.r-project.org/
ProteinLynx Global Server (PLGS) 3.0.3.	Waters Corporation	RRID: SCR_016664
DynamX 3.0	Waters Corporation	Library number: LITR134832928, Part number: 720005145en
UCSF Chimera	PMID:15264254	RRID: SCR_004097
AlphaFold2	PMID:34265844	RRID: SCR_025454
Pymol 2.2.3	Schrodinger	pymol.org
KM plotter	Gyorffy	https://kmplot.com
Gepia2	Zefang Tang, Tianxiang Chen, Chenwei Li and Boxi Kang of Zhang Lab, Peking University.	http://gepia2.cancer-pku.cn
UCSC Xena	University of California Santa Cruz	https://xena.ucsc.edu
cProSite - Cancer Proteogenomic Data Analysis Site	National Cancer Institute Proteomic Data Commons (PDC)	https://cprosite.ccr.cancer.gov
Box Plot R	Tyers and Rappsilber labs	http://shiny.chemgrid.org/boxplotr/
Morpheus	Broadinstitute	https://software.broadinstitute.org/morpheus/

(*Continued on next page*)

Continued

REAGENT or RESOURCE	SOURCE	IDENTIFIER
Other		
LeucoSEP™ Polypropylene Tubes	Greiner Bio-One	Cat#227290
Enzymate BEH pepsin column	Waters Corporation	SKU: 186007233
GSTrap FF	Cytiva	Cat#17-5144-01
Hiprep Q HP	Cytiva	Cat#29018182
HiLoad 16/600 Superdex 75 pg	Cytiva	Cat#28989333
Swiss CI crystallization plates	SWISS CI	Cat#3W96T-PS
3-T MRI scanner	Siemens	Magnetom Trio

EXPERIMENTAL MODEL AND STUDY PARTICIPANT DETAILS

Cell Culture

HeLa (female), HEK293T (female), Huh-7 (male), U2OS (female), HCT116 (male), and PA-TU-8988T (female) cells were cultured in Dulbecco's modified Eagle's medium (DMEM; Gibco) supplemented with 10% fetal bovine serum (FBS) and 1% penicillin/streptomycin (P/S). SK-N-AS1 (female) cells were cultured in Iscove's Modified Dulbecco's Medium (IMDM, Gibco) supplemented with 10% FBS and 1% P/S. MC38 colon adenocarcinoma cells expressing the gp33 peptide (MC38-gp33, female) were thawed and cultured in DMEM supplemented with 10% FBS, 2 mM glutamine, 1 mM sodium pyruvate and 1% P/S. All cell lines were maintained at 37°C in a humidified atmosphere with 5% CO_2. HeLa WT endogenous HA-GABARAPL2 cells were generated using CRISPR/Cas9 technology and kindly provided by the Behrends laboratory (LMU München, Germany).[41] Lentiviral stable cell lines were generated as previously described.[67] The guide RNAs were cloned into lentiviral vectors containing Cas9: pLenti-Puro or pLenti-Neo. The guides used for the CRISPR/Cas 9 KO cells are:

- IRGQ#1: TTTGTGCTACCGGCGAACTG
- IRGQ#2: GAATGCACTCAGTAAGGGAA
- IRGQ#3: CGTGAGGCCTTTGAGACCGG
- GABARAPL2#1: GTCGAGCGAAATATCCCGACA
- GABARAPL2#2: GTCCCACAGAACACAGATGCG
- GABARAPL2#3: GGTTCCATCTGATATCACTG

Following viral infection, cells were selected in media containing 2 μg/mL of puromycin or 1 mg/mL of neomycin.

For gene editing of PA-TU-8998T cells, guide RNAs against ATG5, FIP200, and IRGQ were designed and obtained using the IDT guide RNA (crRNA) design tool as outlined in the manufacturer instructions. Equimolar amounts (240 pM) of the relevant crRNA and tracrRNA (IDT #1072532) were mixed and diluted to a final volume of 10 μL using nuclease-free duplex buffer (IDT). 80 pM Cas9 (IDT #1081058) was diluted to a final volume of 5 μL with nuclease-free duplex buffer, mixed with 5 μL (120 pmol) of sgRNA, and then incubated for 15 mins at RT to form Cas9-RNP complex. PA-TU-8988T cells were resuspended in 22 μL nucleofector SE solution supplemented with 1 μL electroporation enhancer (IDT #1075915), then gently mixed with 10 μL of Cas9-RNP complex. Cell suspensions were transferred to a Lonza 4D nucleocuvette strip, electroporated using program DN-100, incubated at RT for 10 min, then transferred to 6-cm dishes containing pre-warmed media without antibiotics. Single-cell cloning was carried out 2-3 days after selection using the limited dilution method. Monoclonal cell populations were expanded 10-14 days later. KO clones were identified by Western blot using antibodies whose epitopes were distinct from Cas9 RNP target regions. crRNA sequences were as follows: ATG5: GGCCATCAATCGGAAACTCA; IRGQ: ACGGTCCAGAGCACCACATT; FIP200: CTGGTTAGGCACTCCAACAG.

Where indicated, cells were subjected to different treatments. Earl's Balanced Salt Solution (EBSS), for different time points, indicated in respective experiments. Human IFNγ (AF-300-02; Reprotech) was added to cells for 24 hours at a final concentration of 10 ng/mL. Cells were treated with the mTOR inhibitor Torin-1 for 24 h at 250 μM. BafA1 was resuspended in DMSO and added to cells at a final concentration of 200 nM, different time points indicated in respective experiments. MG132 treatment was done at indicated time points, at a final concentration of 500 nM. Cycloheximide (CHX) was used to inhibit protein translation and used at a final concentration of 10 μM for 16 hours.

Isolation of PBMCs, T cells, and macrophages

Human peripheral blood mononuclear cells (PBMCs) were isolated from commercially available buffy coats from anonymous donors using Pancoll (Cat#P04-60500; Pan Biotech GmbH) density centrifugation. Buffy coats were obtained from DRK-Blutspendedienst Baden-Württemberg-Hessen, Institut für Transfusionsmedizin und Immunhämatologie, Frankfurt, Germany. In brief, Pancoll (15 mL) was added to LeucoSEP Polypropylene Tubes (Cat#227290; Greiner Bio-One) and brought under the HDPE barrier by a short centrifugation at 500 × g. Buffy coats (20 mL) were added to each tube, and the volume was adjusted to 50 mL with PBS supplemented

with 2 mM EDTA. Density centrifugation was performed for 35 minutes at 440 × g. After removing blood plasma, the PBMC ring was transferred to a new 50 mL tube. Cells were washed with PBS supplemented with 2 mM EDTA three times and pelleted by 5 minutes of centrifugation at 500 × g. The remaining erythrocytes were removed by hypotonic lysis in ice-cold water for 20 seconds. The lysis was stopped by adding 600 mM KCl solution to a final concentration of 150 mM and filling the volume to 50 mL with PBS supplemented with 2 mM EDTA, and cells were pelleted by 5 minutes of centrifugation at 500 × g. Finally, the cells were resuspended in the appropriate medium for downstream processing and counted using a Neubauer chamber.

Isolation of T cells from PBMCs

T cells were isolated from PBMCs using EasySep Human T Cell Isolation Kit following the manufacturer's protocol. In brief, 5×10^7 cells were resuspended in 2 mL of PBS supplemented with 2 % heat-inactivated FBS and 2 mM EDTA. The Isolation Cocktail (100 μL) was added to the cell suspension and incubated for 5 minutes at room temperature. Rapid Spheres (80 μL) were added to the mixture, the sample volume was adjusted to 2.5 mL with the PBS supplemented with 2 % FCS and 2 mM EDTA, and the sample was placed into the EasySep magnet. After 3 minutes of incubation, the unbound cells were transferred into a new tube. Isolated cells were counted using a Neubauer chamber and processed for the co-culture experiment.

Isolation of human macrophages from PBMCs

Isolated PBMCs were seeded to high-adherence culture dishes in RPMI 1640 medium supplemented with 100 U/mL penicillin and 100 μg/mL streptomycin. Cells were incubated for 1.5 hours under growth conditions, and non-adherent cells were removed by washing with RPMI 1640 medium. Monocytes were differentiated into naïve macrophages with RPMI 1640 medium containing 3% heat-inactivated 0-positive human serum, 100 U/mL penicillin, and 100 μg/mL streptomycin (complete media) for at least seven days.

PA-TU-8988T and human T cell co-culture

IRGQ KO and control PA-TU-8988T cells were treated for 24 hours with 20 nM Tetanus toxin from *Clostridium tetani* (Cat#T3194; Sigma-Aldrich/Merck). As a control, cells were treated with the same volume of PBS. After 24 hours, cells were washed with PBS, trypsinized in Trypsin-EDTA, and transferred in PBS supplemented with 10% heat-inactivated FBS. The cell suspension was counted and mixed with the freshly isolated human T cells in a 1:2 ratio (50000 PA-TU-8988T cells and 100000 T cells) in a 96-well plate. Co-culture was incubated for 24 hours in 100 μL of T cell media (RPMI supplemented with 100 U/mL penicillin, 100 μg/mL streptomycin, 10% heat-inactivated FBS, 1% MEM non-essential amino acids, 1% sodium pyruvate, 1% HEPES buffer solution, and 50 μM β-mercaptoethanol). After 24 hours, cells were collected by trypsinization and processed for FACS analysis.

Purification of gp33-specific CD8+ T cells

Spleens of Nur77eGFP x TCR327 mice were mechanically disrupted and filtered from cell debris through 40 μm cell strainer. Erythrocytes were removed through the use of Gey's lysis buffer. Cells were counted by exclusion of dead cells with trypan blue staining. CD8+ T cells were isolated using the CD8+ T Cell Isolation Kit (mouse, Miltenyi Biotec) according to the manufacturer's instructions using MACS (Magnetic Activated Cell Sorting). The cell number and viability were determined using the Luna-FL cell counter (logos biosystems).

Co-culture of gp33-specific CD+8 T Cells with MC38-gp33 cells

1×10^5 gp33-specific CD8+ T cells and 1×10^5 MC38-gp33 were co-cultured in IMDM supplemented with 10% FBS, 1% glutamine, 1% sodium pyruvate at 37°C, 5% CO_2 in 96-well flat-bottom plates. After 24 hours, cells were collected and processed for FACS analysis.

Hydrodynamic tail-vein injection

All *in vivo* experiments were conducted in accordance with European, national, and institutional guidelines, and protocols were approved by the Regierungspräsidium Darmstadt of the state of Hessen, Germany (FU/2012). C57BL/6 mice were obtained from Jackson Laboratories and were housed in standard cages in pathogen-free facilities on a 12-hour light/dark cycle with ad libitum access to food and water.

For Hydrodynamic tail-vein injection, all animals were examined before starting the experiments to ensure they were healthy and acclimated to the laboratory environment. Six to 8-week-old female mice were injected with a sterile mix of 0.9 % NaCl solution/plasmid corresponding to 10 % of their body weight. Each mouse received 12 μg of c-myc-PT3EF1 (MYC) (Addgene plasmid #92046; https://www.addgene.org/92046/), 12 μg of PX330-sg-Tp53 (or PX330-sg-Tp53-sg-Irgq), and 2 μg of SB100 transposase–encoding plasmids.[68] Mice were injected into one of their lateral tail veins in 5-8 seconds. Hydrodynamic tail injection was performed under isofluorane anesthesia. Vectors for hydrodynamic delivery were produced using the plasmid PlusMega kit (QIAGEN, Cat. No. 12941).

The health of the animals was monitored at least bi-weekly, and tumor growth was followed by contrast-enhanced magnetic resonance imaging (MRI) using gadoxetic acid contrast agent (Primovist, Bayer-Schering, Berlin, Germany) and 3-T MRI scanner (Siemens Magnetom Trio, Siemens Medical Solutions, Erlangen, Germany). Before imaging, animals were anesthetized using

ketamine (65 mg/kg) and xylazine (13 mg/kg), injected with gadoxetic acid (0.057 mmol/kg), and positioned in the scanner. Tumor area and number of tumors were quantified using MRI and boxplots were generated using BoxPlotR[69] and p-values were calculated using two-tailed t-test. For survival curves, visualization and log rank p-values were calculated using the online tool KM plotter.[70] Treatments for T cell depletion were initiated one week after the hydrodynamic delivery of the plasmids. For CD8 antibody treatment experiments, mice received 5 sequential (days 12, 14, 16, 18 and 21 upon hydrodynamic injection) intraperitoneal injections with anti-CD8 (200 μg, clone 2.43, BioXcell). Once the animals were sacrificed, livers were collected, formalin-fixed and paraffin-embedded or frozen.

Isolation of mouse peripheral blood cells

Mouse peripheral blood cells were isolated from 50-100 μL of mouse tail vein blood. Blood was collected in the EDTA tubes and centrifuged for 5 minutes at 500 g. The supernatant was removed, and the remaining cell pellet was washed twice with 5 mL of PBS supplemented with 2 mM EDTA. Erythrocyte removal was done by incubating washed cells for 4 minutes in 5 mL of Ery-Lysis Buffer (155 mM NH_4Cl, 10 mM $NaHCO_3$, 0.1 mM Na-EDTA). Lysis was stopped by adding an equal amount of PBS supplemented with 2 mM EDTA, and the cells were pelleted by centrifugation for 5 minutes at 500 g. Lysis of the erythrocytes was repeated until no visible red cell pellet was observed in the tube after centrifugation (2-3 times). After the last centrifugation step, the cells were resuspended in PBS supplemented with 0.5 % BSA (Cat#7076.3; Carl Roth) and processed for FACS analysis.

Analysis of Human publicly available datasets

Kaplan-Meier curves for liver cancer patient survival curves were estimated with the online tool KM plotter[70] based on GEO, EGA and TCGA datasets. Using the KM plotter online tool, patients were split using the option 'Auto select best cutoff' in high or low IRGQ gene expression groups. Log-Rank p-values were automatically calculated by the online tool KM plotter.

Box plot comparing TCGA gene expression between normal and HCC tumor samples was generated using the online tool GEPIA.[71] For GEPIA, the differential analysis was based on TCGA tumors versus (TCGA normal, whereas the expression data was log_2 (TPM+1) - transformed and the l–g2FC was defined as median (tumor) - median (normal). P-values were calculated with a one-way ANOVA comparing tumor with normal samples.

Heatmap comparing gene expression of liver HCC samples was performed using UCSC Xena online tool.[72] Heatmap data was downloaded as log_2(norm_count+1) using UCSC Xena and the groups high vs low IRGQ were visualized using BoxPlotR.[69] P-values were calculated using two-tailed t-test.

Box plots comparing relative protein abundance (TMT log_2 ratio) between normal and HCC tumor samples was generated using the online tool Cancer Proteogenomic Data Analysis Site[73] based on National Cancer Institute's Clinical Proteomic Tumor Analysis Consortium (CPTAC) and National Cancer Institute's International Cancer Proteogenome Consortium (ICPC) datasets.

METHOD DETAILS

Transfections of siRNA and plasmids

Expression constructs of indicated proteins were cloned into indicated vectors using PCR or a gateway system. Site-directed mutagenesis was performed by PCR to introduce desired amino acid substitutions. All expression constructs were sequenced by Seqlab.

Plasmid transfections were performed with 3 μL GeneJuice (Merck Millipore) or Turbofect (Thermo Fisher Scientific), 0.5 μg (for microscopy), or 1 ug (for Western blot and MS analyses) total plasmid DNA in 200 μL Opti-MEM (Life Technologies). After incubation for 15 minutes, the solution was added to the cells. After 24 hours, cells were used for downstream analysis.

siRNA transfections were performed with 3 μL RNAiMax (Invitrogen), 20 nM siRNA (IRGQ #1: GCAAGATGGAGAATCCCAA, IRGQ #2: CCTCTTGTCTGCGTGCGCA, LC3B #8-6522-3/7 [Eurofins Genomics] or AllStars Negative Control siRNA [Qiagen]) in 150 μl Opti-MEM (Life Technologies). All siRNA treatments were accompanied by a non-targeting siRNA control. After incubation for 15 minutes, the solution was added to the cells cultured in a 6-well dish, which were used for downstream analysis 72 hours post-transfection.

siRNA transfections of MC38-gp33 were performed with 3 μL Turbofect Transfection Reagent (Invitrogen), 30 nM siRNA (IRGQ: Horizon Discovery, L-042471-01-0005; control: Qiagen, SI03650318) in 200 μl Opti-MEM. After incubation for 15 minutes, the solution was added to the cells cultured in a 6-well dish, which were used for downstream analysis 72 hours post-transfection. The cell number and viability were determined using the Luna-FL cell counter (logos biosystems).

In primary human macrophages, control siRNA and siRNAs targeting human IRGQ were co-transfected with siGLO at a final concentration of 50 nM each using HiPerFect transfection reagent according to the manufacturer's recommendations. Each knockdown was routinely confirmed by Western blot for each experiment. In brief, siRNAs were mixed with HiPerFect transfection reagent and RPMI supplemented with 100 U/mL penicillin and 100 μg/mL streptomycin. The transfection mixture was vortexed and incubated for 10 minutes at room temperature. The cells were washed with RPMI supplemented with 100 U/mL penicillin and 100 μg/mL streptomycin before transfection. 600 μL of transfection mixture was added to each well, and the cells were incubated for 6 hours. After 6 hours of incubation, 0.9 mL of complete media was added. The following day cells were washed, and fresh 2 mL of complete media was added. Knockdown was done for 3 days.

Cell lysis

For pulldowns and immunoprecipitations, cells were washed with PBS and scraped on ice in IP lysis buffer (50 mM Tris, pH 7.5, 150 mM NaCl, 0,5 mM EDTA, 1% Triton X-100), supplemented with complete protease inhibitors (cOmplete, EDTA-free; Roche Diagnostics) and phosphatase inhibitors (P5726, P0044; Sigma-Aldrich). Mechanical disruption was performed with an insulin syringe (each sample was passed through 20 times, without foaming), subsequently, samples were incubated for 30 minutes on ice. Lysates were cleared by centrifugation at 15000 rpm for 15 minutes at 4°C.[74]

For general Western blot, total cell lysis buffer (TCL) was used at room temperature (50 mM Tris HCl, pH 7.5, 1 mM EDTA, 150 mM NaCl, 1% SDS, 25 mM NaF, 11 μl/mL Benzonase (71205-25KUN; Millipore)), supplemented with complete protease inhibitors (cOmplete, EDTA-free; Roche Diagnostics) and phosphatase inhibitors (P5726, P0044; Sigma-Aldrich). In some instances, cells were lysed by sonication in 8M Urea buffer with 50 mM Tris HCL pH 7.5, 150 mM NaCl, supplemented with complete protease inhibitors (cOmplete, EDTA-free; Roche Diagnostics) and phosphatase inhibitors (P5726, P0044; Sigma-Aldrich).

Protein expression and purification

GST or His-tagged fusion proteins were expressed in E. coli strain BL21 (DE3). Bacteria were cultured in LB medium supplemented with 100 μg/mL ampicillin at 37°C in a shaking incubator (150 rpm) until OD600 ~0.5-0.6. Protein expression was induced by the addition of 0.5 mM IPTG and cells were incubated at 16°C for 16 hours. Bacteria were harvested by centrifugation (4000 rpm) and lysed by sonication in GST lysis buffer (20 mM Tris HCl, pH 7.5, 10 mM EDTA, pH 8.0, 5 mM EGTA, 150 mM NaCl, 0.1% β-mercaptoethanol, 1 mM PMSF) or His lysis buffer (25 mM Tris HCl, pH 7.5, 200 mM NaCl, 0.1% β-mercaptoethanol, 1 mM PMSF, 1mg/mL lysozyme). Lysates were cleared by centrifugation (10000 rpm), 0.05% of Triton X-100 was added and the lysates were incubated with glutathione Sepharose 4B beads (GE Life Sciences) or Ni-NTA agarose beads (Thermo Fisher Scientific) on a rotating platform at 4°C for 1 hour. The beads were washed five times either in GST wash buffer (20 mM Tris HCl, pH 7.5, 10 mM EDTA, pH 8.0, 150 mM NaCl, 0.5% Triton X-100, 0.1% β-mercaptoethanol, 1 mM PMSF) or His wash buffer (25 mM Tris HCl, pH 7.5, 200 mM NaCl, 0.05% Triton X-100, 10 mM Imidazole). The immobilized proteins were reconstituted in GST storage buffer (20 mM Tris HCl, pH 7.5, 0.1% NaN3, 0.1% β-mercaptoethanol) or eluted with His elution buffer (25 mM Tris HCl, pH 7.5, 200 mM NaCl, 300 mM Imidazole) and dialyzed in (25 mM Tris HCl, pH 7.5, 200 mM NaCl) at 4°C for 16 hours.[75]

For crystallization of IRGQ-GABARAPL2 complex, N-terminal His-tagged IRGQ (1-192) and GABARAP-L2 (1-117) were cloned into pRSFDuet-1 vectors and co-expressed in *E. coli* strain BL21 (DE3) using similar methods described above. Cell pellets were lysed by sonication and centrifuged at 35000 g. The clarified cell extract was incubated with 2.5 mL of Ni-NTA resin pre-equilibrated with lysis buffer (50 mM HEPES pH 7.5, 500 mM NaCl, 10 mM imidazole, 5 % Glycerol, 0.5 mM TCEP). The column was washed with 100 mL Binding Buffer (50 mM HEPES pH 7.5, 500 mM NaCl, 5 % glycerol, 10 mM imidazole, 0.5 mM TCEP), 50 mL wash buffer (50 mM HEPES pH 7.5, 500 mM NaCl, 5 % glycerol, 40 mM imidazole, 0.5 mM TCEP) and eluted with 15 mL of Elution Buffer (50 mM HEPES pH 7.5, 500 mM NaCl, 5 % glycerol, 250 mM imidazole, 0.5 mM TCEP). The eluant fractions were concentrated to 5 mL and applied to a Superdex 200 16/60 column pre-equilibrated in GF Buffer (50 mM HEPES pH 7.5, 500 mM NaCl, 0.5 mM TCEP, 5 % glycerol).

Purified GST-MHC-I was purchased from Novus Biologicals.

HDX mass spectrometry

Equilibration (E)-, labelling (L) and quench (Q)-buffers were prepared freshly in either H_2O (E-buffer: 50 mM HEPES, 200 mM NaCl, 5 mM DTT at pH: 7.5, Q-buffer: 150 mM potassium phosphate, at pH 2.2) or D_2O (L-buffer: 50 mM HEPES, 200 mM NaCl, 5 mM DTT at pD: 7.1). Prior to the experiment, buffers E/L were equilibrated to RT and buffer Q was cooled to ~0 °C. Protein samples were thawed on ice and centrifuged at 16000 g for 45 min prior to use. GST-IRGQ was diluted to a concentration of 9 μM and 12 μM (15/20 pmol on pepsin column per injection) for HDX experiments with GABARAPL2 and LC3B, respectively. GABARRAPL2 and LC3B were added in 4X molar excess at a concentration of either 36 μM or 48 μM (60/80 pmol on pepsin column per injection).

HDX mass spectrometry experiments were performed using an automated HDX-2 system (Waters, Milford USA) as described in [76]. In brief, we incubated GST-IRGQ with a four-fold molar excess of GABARAPL2 and LC3B and recorded deuterium uptake for 5 time points up to 40 minutes, as well as a control experiment without any ligand. Differences in deuterium uptake have been plotted onto the IRGQ AlphaFold model prediction (identifier: AF-Q8WZA9-F1). To focus on the segments with the most prominent differential uptake, we applied stringent manual data curation. This rigorous analysis yielded only a moderate sequence coverage (56.1 %), but enabled us to clearly identify sequence loci of decreased deuterium uptake.

HD exchange reactions were initiated by diluting 4 μl of GST-IRGQ incubated with either GABARAPL2 or LC3B in 56 μl of buffer E (reference) or buffer L (D_2O labelling) for several time points (0, 30, 180, 900 and 2400 seconds). Exchange reactions were quenched by mixing 50 μl of the sample with 50 μl of buffer Q. Following 30 seconds of incubation, 95 μl were injected into a temperature-controlled chromatography system equipped with a 50 μL sample loop (HDX nanoAqcuity UPLC, Waters). Proteins were digested online using a pepsin column (Enzymate BEH pepsin column; 2.1 x 30 mm; Waters). Eluting peptides were trapped on a C18 pre–column (C18 1.7 μM VanGuard 2.1 x 5 mm pre-column; Waters) at a flow rate of 100 μl/min for 3 minutes and separated on an analytical reversed-phase column (C18 1.7 μM Acquity UPLC 1 x 100 mm reverse phased column; Waters) with a 7-minute linear gradient from 5 % ACN (acetonitrile) to 40 % ACN + 0.23 % FA at 40 μL/minute. Next, the ACN concentration was increased to 95 %, held for 2 minutes, prior to column equilibration with 95 % H_2O + 0.23 % FA for 2 minutes. The reversed-phase chromatography system was

cooled to ~0 °C to minimize HD back exchange. Peptides were measured using a Synapt G2-Si mass spectrometer (Waters, Milford USA) in HDMS^E mode (50-2000 *m/z*), adding a third dimension of peptide separation on the basis on precursor ion mobility (LC, IM, *m/z*). The mass spectrometer was fitted with an electrospray source that is equipped with an additional independent LockSpray probe (GluFib lock mass: 785.8426 *m/z*) for alternating lock mass infusion.

Peptide identification was performed using the ProteinLynx Global Server 3.0.3. (PLGS, Waters) for each non-deuterated reference condition (control and binding). Only peptides with a high confidence score > 6 that were identified in at least three out of four technical replicates were kept for evaluation. Annotation of all isotope peaks based on weighted average *m/z* (centroid) in each peptide was performed using DynamX 3.0 (Waters). The relative deuterium uptake was determined through comparison of centroid masses of deuterated isotope peaks in each peptide and the corresponding non-deuterated reference peaks. All acquired spectra were manually inspected and strictly revised as necessary. To test for statistically significant differences in deuterium uptake, all peptides and their respective spectra were analysed using a two-stage t-test as described in [76]. In brief, the positive standard error of the mean (SEM) was determined across four technical replicates at each time point. The average SEM was calculated by dividing the sum of every SEM in each time point and condition with the number of time points. The t-distribution value for a 95 % confidence interval was used in the first stage (n = 3, $P \leq 0.05$, two-sided unpaired). Following calculation of the precursor-specific test value, precursors were evaluated as significant in the first stage if the absolute deuterium uptake difference in each time point is equal or greater than the calculated test value. At least three time points of each precursor had to pass the first stage for further consideration. In the second stage, summed differences of all time points were calculated and the corresponding SEM was estimated (multiplication of average SEM for each precursor and the number of timepoints). The second test value was computed by multiplying the SEM of the summed uptake differences with the t-distribution value for a 98 % confidence interval (n = 5, two-sided, unpaired). A precursor was considered significantly different if the absolute value of summed uptake differences is equal to or greater than the calculated test value. Only peptides that passed the two-stage t-test were used for visual representation on the IRGQ structure (crystal structure of IRGQ-NTD with GABARAPL2 and AlphaFold model prediction) using UCSF Chimera (version 1.16).[77]

X-Ray crystallography

Purified GABARAPL2 and IRGQ complex (12 mg/ml) was crystallised in sitting drops containing 75 nL protein and 75 nL well solution containing 20 % (w/v) PEG 3000, 0.1 M Tri-Sodium citrate pH 5.5 were equilibrated at 20 °C. Crystals were cryo-protected using 25% (v/v) ethylene glycol and flash-cooled in liquid nitrogen.

Tag-free LC3B protein (concentration: 15 mg/ml) was crystallized in the presence of two-fold molar excess of IRGQ LIR2 peptide (EDETWEVLE). 0.3 μl of this complex was added to 0.3 μl of crystallization solution (1.0 M Lithium chloride, 0.1 M Citrate pH-4.0 and 20 % w/v PEG 6000) in a sitting drop crystallization plate with 30 μl of crystallization solution. The plates were incubated at 20 °C for 4 days. The obtained crystals were cryopreserved using 25 % ethylene glycol and flash frozen in liquid nitrogen.

Structure solution and refinement

The crystals were sent to Swiss Light Source PX beamline for X-ray diffraction experiment. IRGQ-GABARAPL2 complex diffracted to 1.8 Å and LC3B-LIR2 peptide crystals diffracted to 1.6 Å resolution. Integration was performed using *XDS*[78] and data scaling and merging were carried out with *AIMLESS*[79] via the *CCP4i2* interface.[80] The relevant statistics are given in Table S1. Data processing focused on $CC_{1/2}$ as a primary quality parameter, with the goal of achieving a value above 50 %.[68] LC3B-LIR2 dataset was processed to a resolution of 1.6 Å, resulting in $CC_{1/2} = 0.862$ in the highest resolution shell and an $\langle I/\sigma(I)\rangle$ of 1.88. The structure was determined by molecular replacement (CCP4i2 Phaser) using the published crystal structures of human LC3B (PDB code: 3VTU), AlphaFold model of IRGQ fragment (1-192) and human GABARAPL2 (PDB code: 4CO7) as search models. The corresponding electron density for LIR2 peptide was manually built in Coot[81] and the resulting model was used for refinement using Phenix Refine interface.[82]

Modeling IRGQ–hATG8 complexes

We modeled the 3D structure of the human IRGQ in complex with all six hATG8 molecules (GABARAP, GABARAPL1, GABARAPL2, LC3A, LC3B and LC3C) using AlphaFold2-Multimer [83] a state-of-the-art neural network-based structure prediction method. We obtained 25 top-ranked models for each complex and analyzed each structure for LIR–LDS contacts across the IRGQ–hATG8 interface.

qRT-PCR

Cells were seeded on 6-well dishes and treated as indicated. RNA isolation and DNAse treatment were performed according to the kit's protocol (Qiagen #74104, #79254). RNA concentration was measured, and 2 μg was used for cDNA synthesis. For cDNA synthesis, the BioRad Kit was used (#170-8891). For the qRT-PCR, 1 μL of cDNA was used. Per reaction: 1 μL cDNA, 5 μL of SYBR green mix (Roche, #04707516001), 0.5 μL of forward primer (from 10 mM stock), 0.5 μL of reverse primer (from 10 mM stock), 3 μL dH_2O. Each condition has a technical triplicate. Primers used are:

- GAPDH Fw: TGCACCACCAACTGCTTAGC
- GAPDH Rv: GGCATGGACTGTGGTCATGAG
- HLA-A Fw: GAGGAGGAAGAGCTCAGATAGA

- HLA-A Rv: GGCAGCTGTCTCACACTTTA
- HLA-B Fw: GGACTGAGATGCAGGATTTCTT
- HLA-B Rv: TCTCTCCACCTCCTCACATTAT
- HLA-C Fw: AATGTGAGGAGGTGGAGAGA
- HLA-C Rv: CCTCTCTGGAACAGGAAAGATG
- B2M Fw: CCAGCGTACTCCAAAGATTCA
- B2M Rv: TGGATGAAACCCAGACACATAG

Immunofluorescence microscopy and live-cell imaging

For immunofluorescence (IF), transfected U2OS cells were seeded onto 12-mm-diameter glass coverslips in 12-well culture dishes and treated accordingly. Cells were washed in PBS before fixation with 4% paraformaldehyde for 8 minutes at room temperature (RT). Cells were rinsed with PBS before being incubated for 2 minutes in permeabilization solution (PMS, 0.1% Saponin (47036; Sigma-Aldrich), 5 mM $MgCl_2$ in PBS). Then, incubated 1 hour in antibody solution at RT (0.1% Saponin (47036; Sigma-Aldrich), 5 mM $MgCl_2$, 5% BSA in PBS, plus the designated primary antibody). After three washes in PBS, cells were incubated with respective secondary antibodies in antibody solution (0.1% Saponin (47036; Sigma-Aldrich), 5 mM $MgCl_2$, 5 % BSA in PBS, plus secondary antibody, and nuclear stain 4',6-diamidino-2-phenylindole (DAPI)) for 1 hour, at RT, in the dark. Cells were washed twice in PBS and once with deionized water before being mounted onto glass slides using a mounting medium (Sigma-Aldrich). Slides were imaged using a Leica Microscope Confocal SP8 fitted with a 60x oil-immersion lens. Images were analyzed and processed using the ImageJ software.

For live cell imaging, transfected U2OS cells were seeded onto 35 mm Petri dishes with a glass bottom. Cells were treated with EBSS and incubated with LysoTracker Red DND-99 (Invitrogen) for half an hour. Subsequently, cells were washed in phosphate-buffered saline (PBS) and normal DMEM was replaced with phenol-red-free DMEM (Gibco). Dishes were live-imaged on a 37 °C warming stage, for no longer than 5 minutes and images were collected using a Leica Microscope Confocal SP8 fitted with a 60xoil-immersion lens. Images were analyzed and processed using the ImageJ software.

Pulldowns and Immunoprecipitation

Cleared cell extracts were mixed with Myc-agarose beads (20169; Thermo Fisher Scientific), Flag-M2 agarose beads (A2220; Sigma-Aldrich), Streptavidin-dynabeads (65605D; Thermo Fisher Scientific), RFP-Trap_A beads (rta-10; ChromoTek) or GFP-Trap_A beads (gta-10; ChromoTek) 16 hours at 4 °C on a rotating platform. The beads were washed four times in IP lysis buffer. Immunoprecipitated and input samples were reduced in SDS sample buffer (50 mM Tris HCl, pH 6.8, 10 % glycerol, 2 % SDS, 0.02 % bromophenol blue, 5 % beta-mercaptoethanol) and heated at 95 °C for 5 minutes.[84,85]

Immunoprecipitation (IP) with different HLA antibodies was done from PA-TU-8988T cells seeded in 15 cm dishes. Cells were lysed as described (in this case, with 1 mL of buffer). Input samples (100 μL) were reduced in sodium dodecyl sulphate (SDS) sample buffer (50 mM Tris–HCl, pH 6.8, 10 % glycerol, 2 % SDS, 0.02 % bromophenol blue, 5 % beta-mercaptoethanol) and heated at 95 °C for 10 minutes. The rest of the lysate was divided in two 2 mL Eppendorf tubes (400 μL), one for each HLA antibody and diluted three times with detergent-free IP-lysis buffer (total final volume 1600 μL). Samples were precleared with 10 μL of Protein-G beads for 1 hour at 4 ºC in a rotating platform. Immunoprecipitation was done by incubation for 16 hours at 4 ºC with 3 μg of each antibody. Then, 10 μL Protein A agarose beads were added to each tube and incubated for 1 hour at 4 ºC on a rotating platform. Samples were centrifuged, and beads and supernatant were separated. Beads were labeled as the 1st IP, washed 4 times with IP wash buffer, reduced in SDS sample buffer, and heated at 95 °C for 10 min. The supernatant, collected in a different tube, was incubated again for 16 hours with the opposite antibody (3 μg). Afterward, protein A beads (10μL) were added to each tube and incubated again for 1 hour at 4 ºC in a rotating platform. Beads were collected, labeled as 2nd IP, and processed as before. Samples were stored at -20 ºC until Western blot.

α^{P32}GTP binding assay

Proteins were immobilized on glutathione-Sepharose beads, or immunoprecipitated with FLAG-beads from HEK293T cells and washed using GTPase lysis buffer. Nucleotide chelation was performed by incubating the proteins for 10 minutes with 10 mM EDTA. Subsequently, α^{P32}GTP loading was achieved by incubation with α^{P32}GTP (SRP-108; Hartmann Analytic) for 30 minutes at 30 °C. The reaction was terminated by the addition of 60 mM $MgCl_2$ after three washes in the GTPase lysis buffer. Samples were spotted on PVDF membranes to perform Dot-blot analysis, with subsequent analysis by autoradiography.

Antibodies

The following antibodies were used in this study: anti-HA-tag (11867423001; Roche), anti-vinculin (V4505; Sigma-Aldrich), anti-IRGQ (HPA043254; Sigma-Aldrich), anti-LC3B (PMO36; MBL), anti-Lamp1 (Ab24170; Abcam), anti-REEP5 (sc-393508; Santa Cruz Biotechnology), anti-HLA-ABC-I (15240-1-AP; Proteintech), anti-HLA W6/32 (MABN1783; Sigma-Aldrich), anti-B2M (13511-1-AP; Proteintech), anti-HLA HC10 (Nordic MUbio; MUB2037P), anti-FlagM2-tag (F3165; Sigma-Aldrich), anti-GFP-tag (Living Colors 632592; Clontech), anti-His-tag (11922416001; Roche), anti-tubulin (T9026; Sigma-Aldrich), anti-GAPDH (#2118; Cell Signaling

Technology), anti-VDAC (#55259-1-AP; Proteintech), anti-EGFR (#2232; Cell Signaling Technology), anti-GABARAPL2 (PM038; MBL), anti-LAMP1 (H4A3; DSHB), anti-p62 (M162-3; MBL), anti-PARP (#9542; Cell Signaling Technology), anti-Histone H2A (Ab18255; Abcam), anti-Histone H3 (#9715; Cell Signaling Technology), anti-IRGM (Ab69494; Abcam), anti-pSTAT1 (pY701; #7649; Cell Signaling Technology). Primary antibodies used for Western blot were diluted 1:1000 and for immunofluorescence studies 1:200. Secondary HRP conjugated antibodies: goat anti-mouse (sc-2031; Santa Cruz Biotechnology), goat anti-rabbit (sc-2030; Santa Cruz Biotechnology) and goat anti-rat (sc-2006; Santa Cruz Biotechnology) were used for immunoblotting. Anti-rat Alexa Fluor 647 (A-21247; Life Technologies), anti-rat Cy3 (712166153; Jackson Lab), anti-mouse Alexa Fluor 405 (A-31553; Life Technologies), anti-mouse Cy3 (715-165-151; Dianova), anti-rabbit Alexa647 (A21244; Life Technologies), anti-mouse Alexa 647 (A-31626; Life Technologies) were used for immunofluorescence studies.

Cellular fractionation into soluble and insoluble fractions

PA-TU-8988T cells were seeded in 10 cm dishes and treated with BafA1 and MG132 as indicated. Cells were lysed with 300 μL of RIPA buffer (25 mM Tris/HCl pH 7.6, 150 mM NaCl, 1 % NP40, 1 % Sodium Deoxycholate, 0.1 % SDS; 10 mM NEM, 1 mM PMSF). Samples were centrifuged at 20000 g for 30 minutes. Supernatant was transferred to a precooled tube and SDS loading buffer added, and incubated at 95 ºC for 10 minutes. The pellet was carefully washed 3 times with cool PBS. After each wash, the pellet was centrifuged at 20000 g for 10 minutes. After the last wash, the supernatant was discarded and the pellet was resuspended in 40 μL of SDS buffer, boiled at 95 ºC for 10 minutes and both fractions (cellular fraction and insoluble fraction) were analyzed by Western blot.

EndoH/PNGase treatment

Cells were lysed in endoH-lysis buffer (1 % Triton X-100, 100 mM NaCl, 50 mM Tris-HCl, pH 7.5, 20 mM N-Ethylmaleimide) using mechanical force with a 5 mL syringe and lysates were centrifuged for 10 minutes at 21000 rpm. Lysate supernatant (18 μL) and denaturing buffer (New England Biolabs) (2 μL) were incubated at 95 °C for 10 minutes. Following, 20 μL of the corresponding mastermix (endoH-mastermix: 4 μL glycobuffer 3, 2 μL endoH, 14 μL H_2O; PNGase-mastermix: 4 μL glycobuffer 2, 4 μL nonidet-P40, 2 μL PNGase, 10 μL H_2O) were added and incubated for 1 hour at 37 °C. Samples were analyzed by Western blot.

Cellular fractionation of organelles

Cellular fractionation was performed as previously described in [86]. In brief, cells were trypsinized and pelleted. The cell pellet was resuspended in $IB_{cells}1$ buffer (225 mM mannitol, 75 mM sucrose, 0.1 mM EGTA and 30 mM Tris-HCl, pH 7.4) at 4 °C. Cells were homogenized using a Teflon pestle and centrifuged at 700 g for 5 minutes at 4 °C. The pellet is discarded and the supernatant is centrifuged again at 7000 g for 10 minutes at 4 °C obtaining the cytosolic fraction in the supernatant, which will be further processed for isolation of the ER. The obtained pellet is resuspended in $IB_{cells}2$ buffer (225 mM mannitol, 75 mM sucrose and 30 mM Tris-HCl, pH 7.4) and centrifuged at 7000 g for 10 minutes, at 4 °C. The obtained pellet is the crude mitochondrial faction, which was further processed for SDS-PAGE analysis. The supernatant of the cytosolic fraction is further processed to sub-fractionate the ER by centrifugation at 20000 g for 30 minutes, at 4 °C. The resulting pellet is discarded and the supernatant is further centrifuged at 100000 g for 1 hour, at 4 °C, obtaining the ER fraction in the pellet and the cytosolic fraction in the supernatant. Both samples were further processed for SDS-PAGE analysis.

Proximity ligation assay (PLA)

The PLA Duolink® In Situ Detection Reagents (DUO92014, Sigma-Aldrich), Duolink® In Situ PLA® Probe Anti-Rabbit PLUS (DUO92002, Sigma-Aldrich) and Duolink® In Situ PLA® Probe Anti-Mouse MINUS (DUO92004, Sigma-Aldrich) were used and experiments performed according to the manufacturer's protocol. The primary and secondary antibodies were each used for 1 hour at room temperature at a dilution of 1:100 in antibody solution (0.1 % Saponin (47036; Sigma-Aldrich), 5 mM $MgCl_2$, 5 % BSA in PBS). The secondary antibody solution also contained Alexa Phalloidin 647 and DAPI.

Lysosomal Immunoprecipitation

Lysosomal Immunoprecipitation was carried out as described in [35–37] with a few modifications. Briefly, cells stably expressing Tmem192-3X HA were seeded in 15 cm plates. All buffers were supplemented with protease inhibitors. At 80 % confluency, the cells were scraped on ice and washed once with PBS containing protease inhibitors (Roche). The cells were pelleted at 300 g for 5 minutes at 4 ºC and were washed once with KPBS buffer (136 mM KCl, 10 mM KH_2PO_4, 50 mM sucrose at a pH 7.2). The cell pellet was resuspended in 1 mL KPBS and lysed using 30 strokes in a 2 mL Potter-Elvehjem homogenizer. The lysed cells were spun down at 1000 g for 5 minutes at 4 ºC. The pellet was discarded and the protein concentration of the lysate was determined by Bradford assay. After normalizing the protein concentration to be equal across all replicates, 5 % of the input sample was saved and 50-100 μL of anti HA magnetic beads was added the remainder of the sample. This mixture was placed on gentle rotation for 20 minutes, and beads were separated from the lysate using a magnetic stand. The beads were washed twice with KPBS containing 300 mM NaCl and once with KPBS buffer. The samples were then eluted either by boiling the beads with 100 μL 2x Laemmeli buffer (for Western blot) for 10 minutes or with 100 μL KPBS containing 0.5 % NP-40 in a thermo-mixer at 30 ºC for 20 minutes (for MS). Eluates for MS were snap frozen in liquid nitrogen and stored in -80 °C until further processing.

TMT total cell or lysosomal proteomics

A detailed version of this protocol is available at: https://doi.org/10.17504/protocols.io.bw7hphj6.[87] For MS of lysosomal eluates, samples were reduced using TCEP (5 mM for 10 minutes at 55 °C) and alkylated (with chloroacetamide 20 mM at room temperature for 30 minutes) prior to methanol chloroform precipitation. The protein precipitate was washed 3x with ice-cold methanol and resuspended in 200 mM HEPES pH 8.5 for protein digestion. Protein digestion was carried out by 1:100 protease to protein ratio of Lys-C for 2 hours at 37 °C followed by trypsin digestion for 16 hours. Each sample was labeled with TMT reagent (TMT10 reagent, Thermo Fisher Scientific, 90110) for 1 hour, and the reaction was quenched with hydroxylamine at a final concentration of 0.3 % (w/v). 1 % of each sample was mixed in a 1:1:1:1:1:1:1:1:1:1 ratio and a 'ratio-check' analysis using LC-MS/MS was performed to determine if the samples were present in equal ratios. Based on this result, the volumes of the remaining sample were adjusting and combined to maintain the 1:1:1:1:1:1:1:1:1:1 ratio. This combined sample was then dried to completeness using a vacuum centrifuge and acidified with 5 % (w/v) formic acid. Digested peptides were cleaned up using C18 SPE (Sep-Pak, Waters) and separated using basic pH reversed-phase HPLC and pooled into 24 fractions. All 24 fractions were vacuum dried to completeness and subject to the C18 stage tip method prior to loading on the mass-spectrometer. Data was obtained using an Orbitrap fusion Lumos mass spectrometer linked with a Proxeon EASY-nLC 1200 LC pump. Peptides were separated on a 75 μM inner diameter microcapillary tube packed with 35 cm of Accucore C18 resin (2.6 μm, 100A, Thermo Fisher Scientific). The data was acquired using the MS3 method.[88]

For Multi-Notch MS^3-based TMT analysis,[88] the scan sequence began with an MS^1 spectrum (Orbitrap analysis; resolution 60000 at 200 Th; mass range 375–1500 m/z; automatic gain control (AGC) target 5×10^5; maximum injection time 50 ms). Precursors for MS^2 analysis were selected using a Top10 method. MS^2 analysis consisted of collision-induced dissociation (quadrupole ion trap analysis; Turbo scan rate; AGC 2.0×10^4; isolation window 0.7 Th; normalized collision energy [NCE] 35; maximum injection time 90 ms). Monoisotopic peak assignment was used and previously interrogated precursors were excluded using a dynamic window (150 s ± 7 ppm) and dependent scans were performed on a single charge state per precursor. Following acquisition of each MS^2 spectrum, a synchronous-precursor-selection (SPS) MS^3 scan was collected on the top 10 most intense ions in the MS^2 spectrum.[88] MS^3 precursors were fragmented by high-energy collision-induced dissociation and analyzed using the Orbitrap (NCE 65; AGC 3×10^5; maximum injection time 150 ms, resolution was 50000 at 200 Th).

For proteomics data analysis, raw mass spectra obtained were processed as described in [89] and were processed using a Sequest. Mass spectra were converted to mzXml using a version of ReAdW.exe. Database searching included all entries from the Human Reference Proteome. Searches were performed with the following settings (1) 20 ppm precursor ion tolerance for total protein level analysis, (2) product ion tolerance was set at 0.9 Da, (3) TMT or TMTpro on lysine residues or N-termini at +229.163 Da or +304.207 Da, and (4) carbamidomethylation of cysteine residues (+ 57.021 Da) as a static modification and oxidation of methionine residues (+15.995 Da) as a variable modification. Peptide-spectrum matches (PSMs) were adjusted to a 1 % false discovery rate. PSM filtering was performed using a linear discriminant analysis, as described previously.[90] To quantify the TMT-based reporter ions in the datasets, the summed signal-to-noise (S:N) ratio for each TMT channel was obtained and found the closest matching centroid to the expected mass of the TMT reporter ion (integration tolerance of 0.003 Da). Proteins were quantified by summing reporter ion counts across all matching PSMs, as described previously.[90] PSMs with poor quality, or isolation specificity less than 0.7, or with TMT reporter summed signal-to-noise ratio that were less than 100 or had no MS^3 spectra were excluded from quantification.

SurfaceOME

Biotinylation of surface proteins was performed as previously described.[91] Cells were washed three times in ice-cold PBS 1 x Ca^{2+}/Mg^{2+} (pH 7.4) to remove any contaminating proteins and were labelled with 1 mM Sulfo-NHS-LC-Biotin (21335; Thermo Fisher Scientific) diluted in ice-cold PBS 1 x Ca^{2+}/Mg^{2+} (pH 7.4) for 30 minutes at 4 °C. Afterward, cells were washed three times with ice-cold PBS 1 x Ca^{2+}/Mg^{2+} (pH 7.4) and the free biotin was blocked with a solution of 50 mM Tris-HCl, followed by additional washes. The labeled cells were homogenized in 200 μL of buffer A (0.3 mmol/L sucrose, 3 mmol/L DTT, 1 mmol/L EDTA, 100 μg/mL phenylmethylsulfonyl fluoride (PMSF), Triton X-100) and then precipitated by continuous mixing with 40 μL of immobilized NeutrAvidin Protein beads (29200; Thermo Fisher Scientific) for 4 hours at 4 °C. The precipitates were washed four times in PBS 1 x Ca^{2+}/Mg^{2+} (pH 7.4) supplemented with 6 M Urea and then processed for label-free quantitative interactome MS.

Label-free quantitative interactome mass spectrometry

Cells expressing endogenously tagged mCherry-IRGQ were treated as indicated and lysed in IP lysis buffer and immunoprecipitated as stated above. Bound proteins were eluted in NuPAGE LDS Sample Buffer (Life Technologies) supplemented with 1 mM DTT, boiled at 70°C for 10 minutes, alkylated and loaded onto 4-20% gradient SDS-PAGE gels. Proteins were stained using InstantBlue and in-gel digested with trypsin. Peptides were desalted on reversed phase C18 StageTips and analyzed on an Q Exactive HF mass spectrometer (ThermoFisher). The raw data was analyzed using MaxQuant 1.6.5.0 with standard settings and activated LFQ quantification. The database used to identify the peptides was the human reference protein database (UniProt downloaded December 2017) and the FDR was set to 1% on protein, PSM and site decoy level. Statistical analysis was done with Perseus 1.6.5. Proteins were defined as interactors, if they passed a 5 % FDR corrected one-sided two-sample T-test with a minimal enrichment factor of two compared to a control IP.

PTM MS-screen for Venus-IRGQ/HLA complexes

Venus-transfected cells were washed with PBS and scraped on ice in IP lysis buffer (50 mM Tris, pH 7.5, 150 mM NaCl, 0,5 mM EDTA, 1% Triton X-100), supplemented with complete protease inhibitors (cOmplete, EDTA-free; Roche Diagnostics) and phosphatase inhibitors (P5726, P0044; Sigma). Mechanical disruption was performed with an insulin syringe (each sample was passed through 20 times, without foaming), subsequently, samples were incubated for 30 min on ice. Lysates were cleared by centrifugation at 15000 rpm for 15 min at 4 °C. Samples were diluted to 0.25% Triton X-100 with detergent free IP-lysis buffer. Pulldown of cleared cell extracts (lysates from 10 cm dishes of HEK transfected cells) was done by incubation with GFP-Trap A beads (ChromoTek) for 2 hours at 4 °C on a rotating platform. The beads were washed three times in IP wash buffer (50 mM Tris, pH 7.5, 300 mM NaCl, 0,5 mM EDTA, 0,1% Triton X-100). Final washes were done in detergent-free buffer. Peptide digestion was done by incubation with trypsin at 37 °C, for 16 hours. Digested peptides were acidified with trifluoroacetic acid (TFA) (Sigma Aldrich) to inhibit trypsin and peptides were prepared for SDB- RPS StageTip desalting. SDB-RPS StageTips were made by stacking two layers of 3MEm-pore solid phase extraction SDB membranes into a 200-ml micropipette tip. Acidified peptides were loaded onto the SDB-RPS StageTips and washed with 0.1% (v/v) TFA. Peptides were eluted using a two-step elution with 0.1% (v/v) TFA, 80% v/v) ACN and then dried using a speed-vacuum concentrator (45-75 min at 60 °C). Dried peptides were stored at -20 °C. Peptides were analyzed on an Orbitrap EliteTM or Q Exactive HF mass spectrometer (ThermoFisher). The raw data was analyzed using MaxQuant 1.6.5.0 with standard settings and activated LFQ quantification. The database used to identify the peptides was the human reference protein database (uniprot downloaded December 2017) and the FDR was set to 1% on protein, PSM and site decoy level. Search for Ubiquitination and Phosphorylation sites was done. Statistical analysis was done with Perseus.

TMT 9-plex Total Liver Proteome

A total of 10 mg of tissue for each sample were lysed with lysis buffer (2 % SDS, 50 mM Tris-HCl, pH 8.5, 10 mM TCEP, 40 mM chloroacetamide and protease inhibitor cocktail tablet (EDTA-free, Roche)). Samples were incubated for 10 minutes at 95°C before and after sonication with Sonic Vibra Cell at 1s ON/ 1s OFF pulse for 30 seconds at a maximal amplitude of 40 % to shear genomic DNA. Proteins were precipitated using 3 volumes of ice-cold methanol, 1 volume of chloroform and 2.5 volumes of water. After centrifugation at 14,000 g for 15 minutes at 4 °C, the upper aqueous phase was aspirated and 3 volumes of ice-cold methanol were added. Samples were mixed and proteins pelleted by centrifugation at 14,000 g for 5 minutes at 4 °C. Supernatant was discarded and pellets washed one additional time with ice-cold methanol. Protein pellets were dried at RT for further use. Proteins were resuspended in 8 M urea, 50 mM Tris pH 8.2 and protein concentration determined using a BCA assay with BSA as the standard (Thermo Fisher Scientific). 40 μg of protein from each sample were diluted to 0.8 M urea using digestion buffer (50 mM Tris, pH 8.2) and incubated with LysC (Wako Chemicals) at 1:50 (w/w) ratio and Trypsin (Promega, V5113) at 1:100 (w/w) ratio for 16 hours at 37 °C. Digests were acidified using trifluoroacetic acid (TFA) to 0.5 % and peptides were purified using SepPak tC18 columns (Waters, WAT054955). The material was activated with methanol, followed by a wash with 80 % acetonitrile (ACN), 0.1 % TFA and equilibration with 0.1 % TFA. Samples were resuspended in 0.1 % TFA and loaded to resin material. Peptides were washed with 0.1 % TFA and eluted with 60 % ACN. Eluted peptides were dried, resuspended in TMT labeling buffer (0.1 M EPPS pH 8.2, 20 % acetonitrile (ACN)) and peptide concentration determined by micro BCA (Thermo Fisher Scientific, 23235). 10 μg of peptides per sample were mixed with the first 9 channels of TMT10 reagent (UL298812, Thermo Fisher Scientific) in a 1:2 (w/w) ratio (2 μg TMT reagent per 1 μg peptide). Reactions were incubated for one hour at RT and after verification of labeling efficiency (>98 %) and mixing ratios by LC-MS analysis of a test po^{ol} comprising 1/20th of each sample, labeling was quenched by addition of hydroxylamine to a final concentration of 0.5 % and incubation at RT for 15 minutes. Labeled peptides were pooled according to determined mixing ratios in order to achieve the same total peptide intensity in each sample and desalted by SepPak (tC18, 50 mg, Waters). The material was activated with methanol, followed by a wash with 80 % ACN, 0.1% TFA and equilibration with 3 % ACN, 0.1 % TFA. Samples were resuspended in 3 % ACN, 0.1 % TFA and loaded to resin material. Peptides were washed with 3 % ACN, 0.1 % TFA, eluted with 60 % ACN, and dried again. Peptides were fractionated using high-pH liquid-chromatography on a micro-flow HPLC (Dionex U3000 RSLC, Thermo Fisher Scientific). 45 μg of pooled and purified TMT labeled samples were resuspended in Solvent A (5 mM ammonium-bicarbonate, 5 % ACN), were separated on a C18 column (XSelectXSelect CSH, 1 mm x 150 mm, 3.5 μm particle size; Waters) using a multistep gradient from 3-60 % Solvent B (55 mM ammonium-bicarbonate, 90 % ACN) over 65 minutes at a flow rate of 30 μL/minute. Eluting peptides were collected every 43 s from minute 2 for 69 minutes into a total of 96 fractions, which were cross-concatenated into 24 fractions. Pooled fractions were dried in a vacuum concentrator and resuspended in 2 % ACN, 0.1 % TFA for LC-MS analysis. Tryptic peptides were analyzed on an Orbitrap Lumos coupled to an easy nLC 1200 (Thermo Fisher Scientific) using a 35 cm long, 75 μm ID fused-silica column packed in-house with 1.9 μm C18 particles (Reprosil pur, Dr. Maisch), and kept at 50 °C using an integrated column oven (Sonation). HPLC solvents consisted of 0.1 % formic acid in water (Buffer A) and 0.1 % formic acid, 80 % acetonitrile in H2O (Buffer B). 500 ng of peptides were eluted by a non-linear gradient from 7 to 40% B over 90 minutes followed by a step-wise increase to 90 % B in 6 minutes, which was held for another 9 minutes.

A synchronous precursor selection (SPS) multi-notch MS3 method was used in order to minimize ratio compression. Full scan MS spectra (350-1400 m/z) were acquired with a resolution of 120,000 at m/z 200, maximum injection time of 100 ms and AGC target value of 4 x 105. The most intense precursors with a charge state between 2 and 6 per full scan were selected for fragmentation (“Top Speed” with a cycle time of 1.5 seconds) and isolated with a quadrupole isolation window of 0.7 Th. MS2 scans were performed in the Ion trap (Turbo) using a maximum injection time of 50 ms, AGC target value of 1.5 x 104 and fragmented using CID

with a normalized collision energy (NCE) of 35 %. SPS-MS3 scans for quantification were performed on the 10 most intense MS2 fragment ions with an isolation window of 0.7 Th (MS) and 2 m/z (MS2). Ions were fragmented using HCD with an NCE of 65 % (TMTclassic) and analyzed in the Orbitrap with a resolution of 50000 at m/z 200, scan range of 100-500 m/z, AGC target value of 1.5 x105 and a maximum injection time of 86 ms. Repeated sequencing of already acquired precursors was limited by setting a dynamic exclusion of 60 seconds and 7 ppm and advanced peak determination was deactivated. All spectra were acquired in centroid mode. Raw data was analyzed with Proteome Discoverer 2.4 (Thermo Fisher Scientific). Acquired MS2-spectra were searched against the mouse reference proteome (Taxonomy ID 10090) downloaded from UniProt (12-March-2020; ''One Sequence Per Gene'', 21959 sequences) and a collection of common contaminants (244 entries from MaxQuant's ''contaminants.fasta'') using SequestHT, allowing a precursor mass tolerance of 7 ppm and a fragment mass tolerance of 0.5 Da after recalibration of mass errors using the Spectra RC-node applying default settings. In addition to standard dynamic (Oxidation on methionine and Met-loss at protein N-termini) and static (Carbamidomethylation on cysteine) modifications, TMT-labelling of N-termini and lysines were set as static modifications. False discovery rates were controlled using Percolator (< 1% FDR on PSM level). Only PSMs with a signal-to-noise above 10, a co-isolation below 50 %, as well as at least 50 % SPS-matches derived from unique peptides were used for protein quantification after total intensity normalization. High and Medium confident proteins were used for downstream analyses.

Filtering and statistical analysis of the Proteome Discoverer output was performed in Perseus (v 2.0.7.0) as previously described 72. Specifically, only proteins quantified in all replicates in each group (100 % valid values) were used for statistical analysis. Significant proteins were defined after a one-way ANOVA test (S0=0.1, Benjamin-Hochberg FDR <0.01) and subsequent Post-Hoc Tukey's HSD test (FDR <0.01). Reactome Pathway analysis was done in STRING with default settings.

Native PAGE

Samples for Native page were collected from PA-TU-8988T cells. A single well from a 6-well dish for each (WT and IRGQ KO) was lysed in 200 μL of IP buffer (50 mM Tris/HCl pH 7.4, 0,5 mM EDTA, 150 mM NaCl, 1% Triton X-100). Samples were incubated on ice for 30 minutes and mechanically lysed with an insulin syringe (passed through 20 times) and lysate was cleared at maximum speed for 15 minutes. Once lysates were ready, the protocol provided by the manufacturer was followed (NativePAGE Bis-Tris Mini Gel Electrophoresis Protocol 2013, Thermo Fisher Scientific), and samples were run in a 3-12% precast gel from Invitrogen.

Western blot

For immunoblotting, proteins were resolved by SDS-PAGE and transferred to PVDF membranes. Blocking and primary antibody incubations were carried out in 5 % BSA in TBST (150 mM NaCl, 20 mM Tris, pH 8.0, 0.1 % Tween-20), secondary antibody incubations were carried out in 5 % low-fat milk in TBS-T and washings with TBS-T. Blots were developed using Western blot Luminol Reagent (sc-2048; Santa Cruz Biotechnology). All Western blots shown are representative. Quantifications were done with ImageJ software.

Cloning of plasmids for hydrodynamic tail-vein injection

Single gRNAs for mouse Tp53 and mouse Irgq were individually cloned into BbsI site of the PX330 plasmid, which contains Cas9:

mTp53-1: CCTCGAGCTCCCTCTGAGCC
mTp53-2: GTGTAATAGCTCCTGCATGG
mIrgq-1: CCAGGGCGAAGATCCACCCG
mIrgq-2: GACACGGTAGAGATTCCCGA

The obtained plasmids were used for the ASAP (Adaptable System for Assembly of multiplexed Plasmids)-cloning in order to assemble both p53 (plasmid PX330-sg-Tp53) or all 4 (plasmid PX330-sg-Tp53-sg-Irgq) gRNAs expression cassettes into a single PX330 plasmid, as described previously.[92] pX330-gRNA was a gift from Charles P. Lai (Addgene plasmid # 158973; http://n2t.net/addgene:158973).

Flow cytometry and intracellular cytokine staining

PA-TU-8988T cell co-culture: Co-cultured cells were collected, first by collecting the supernatant containing a portion of T cell suspension, and the remaining adherent cells were trypsinized with Trypsin-EDTA. Trypsinization was stopped by adding the PBS supplemented with 10 % heat-inactivated FBS. Both cell fractions were pulled and washed with PBS supplemented with 0.5 % BSA. The cells were incubated with human FcR blocking reagent containing Zombie UV for 10 minutes at 4 °C. Afterwards, the cells were incubated with fluorochrome-conjugated human CD3/CD45 antibody mix prepared in Brilliant Stain Buffer for 20 minutes at 4 °C. During the last 10 minutes of staining, 7-AAD was added. The cells were washed with and resuspended in FACSFlow Sheath Fluid. As a counting standard, Flow Cytometry Absolute Count Standard was added. The data acquisition was performed on the BD FACSymphony A5 SE flow cytometer. The data were processed in R (4.2.2) using RStudio (2022.12.0 Build 353) IDE. The following R packages were used: flowCore (2.10.0), ncdfFlow (2.44.0), flowWorkspace (4.10.1), ggcyto (1.26.4), dplyr (1.1.1), tidyr (1.3.0), ggplot2 (3.4.2), patchwork (1.1.2), ggpubr (0.6.0), and scales (1.2.1).

Macrophages: The cells were washed with PBS and trypsinized for 40 minutes with Trypsin-EDTA. Trypsinization was stopped by adding an equal volume of PBS supplemented with 2 % heat-inactivated FBS. The cells were carefully scraped from the well using a

silicon cell scraper. The cells were transferred to a FACS tube, centrifuged at 500 g for 5 minutes at 4 °C, and resuspended in PBS supplemented with 0.5 % BSA. After one more centrifugation step, the cell pellet was resuspended and incubated with human FcR blocking reagent containing Zombie UV for 10 minutes at 4 °C. Afterwards, the cells were incubated with fluorochrome-conjugated human HLA-ABC/HLA-DR antibody mix prepared in Brilliant Stain Buffer for 20 minutes at 4 °C. The cells were washed with and resuspended in FACSFlow Sheath Fluid. As a counting standard, Flow Cytometry Absolute Count Standard was added. The data acquisition was performed on the BD FACSymphony A5 SE flow cytometer. The data were processed in R (4.2.2) using RStudio (2022.12.0 Build 353) IDE. The following R packages were used: flowCore (2.10.0), ncdfFlow (2.44.0), flowWorkspace (4.10.1), ggcyto (1.26.4), dplyr (1.1.1), tidyr (1.3.0), ggplot2 (3.4.2), patchwork (1.1.2), ggpubr (0.6.0), and scales (1.2.1).

Peripheral mouse blood: Isolated mouse blood cells were pelleted and resuspended in the blocking solution (PBS supplemented with 0.5 % BSA and FcR blocking reagent for mice) to block non-specific binding and blocked for 10 minutes at 4 °C. During the blocking step, cells were stained with Zombie UV die to distinguish between live and dead cells. The cells were incubated with fluorochrome-conjugated anti-mouseCD8a/ CD11b/ CD4/ CD3e/ CD25/ CD62L/ CD279/ CD366/ CD137/ CD44/ CD45/ CD223/ CD19 antibody mix prepared in Brilliant Stain Buffer for 20 minutes at 4 °C. The cells were washed with FACSFlow Sheath Fluid and fixed following the FOXP3/Transcription Factor Staining Kit manufacturer's instruction. In brief, the cells were resuspended in Foxp3 Fixation/Permeabilization working solution and incubated for 40 minutes at 4 °C. Fixation was stopped by adding Permeabilization Buffer. Fixed cells were pelleted and resuspended in the blocking solution (Permeabilization Buffer + Fc blocking reagent for mice). Blocking was done for 20 minuntes, and the samples were stained with fluorochrome-conjugated mouse IFN-γ/FoxP3/Granzyme B antibody mix prepared in Brilliant Stain Buffer for 30 minutes at 4 fcv f °C. The cells were washed with and resuspended in FACSFlow Sheath Fluid. As a counting standard, Flow Cytometry Absolute Count Standard was added. The data acquisition was performed on the BD FACSymphony A5 SE flow cytometer. Spectral data were analyzed in FlowJo (v.10.8.1) and processed in R (4.2.2) using RStudio (2022.12.0 Build 353) IDE. The following R packages were used: dplyr (1.1.1), tidyr (1.3.0), ggplot2 (3.4.2), patchwork (1.1.2), ggpubr (0.6.0), and scales (1.2.1).

Nur77eGFP-expressing cells: Flow cytometric experiments were performed on FACSymphony A5 (BD Bioscience) flow cytometer and analyzed using FlowJo 10.0 software (BD Bioscience). For surface staining, cells were incubated with antibodies against the indicated markers and fixable viability dye 780 (ThermoFisher; 65-0865-14) for live/dead cell determination for 30 minutes at 4 °C.

QUANTIFICATION AND STATISTICAL ANALYSIS

All experiments have a minimum of three biological replicates. Data are presented as the mean with error bars indicating the s.d. (standard deviation). The statistical significance of differences between experimental groups was assessed with Student's T-test. Differences in means were considered significant if $p<0.05$. Differences with $p<0.05$ are annotated as *, $p<0.01$ are annotated as ** and $p<0.001$ are annotated as ***. Statistical values measurements were performed using R software with corresponding R packages, Excel or PRISM.

CellPress
OPEN ACCESS

Supplemental figures

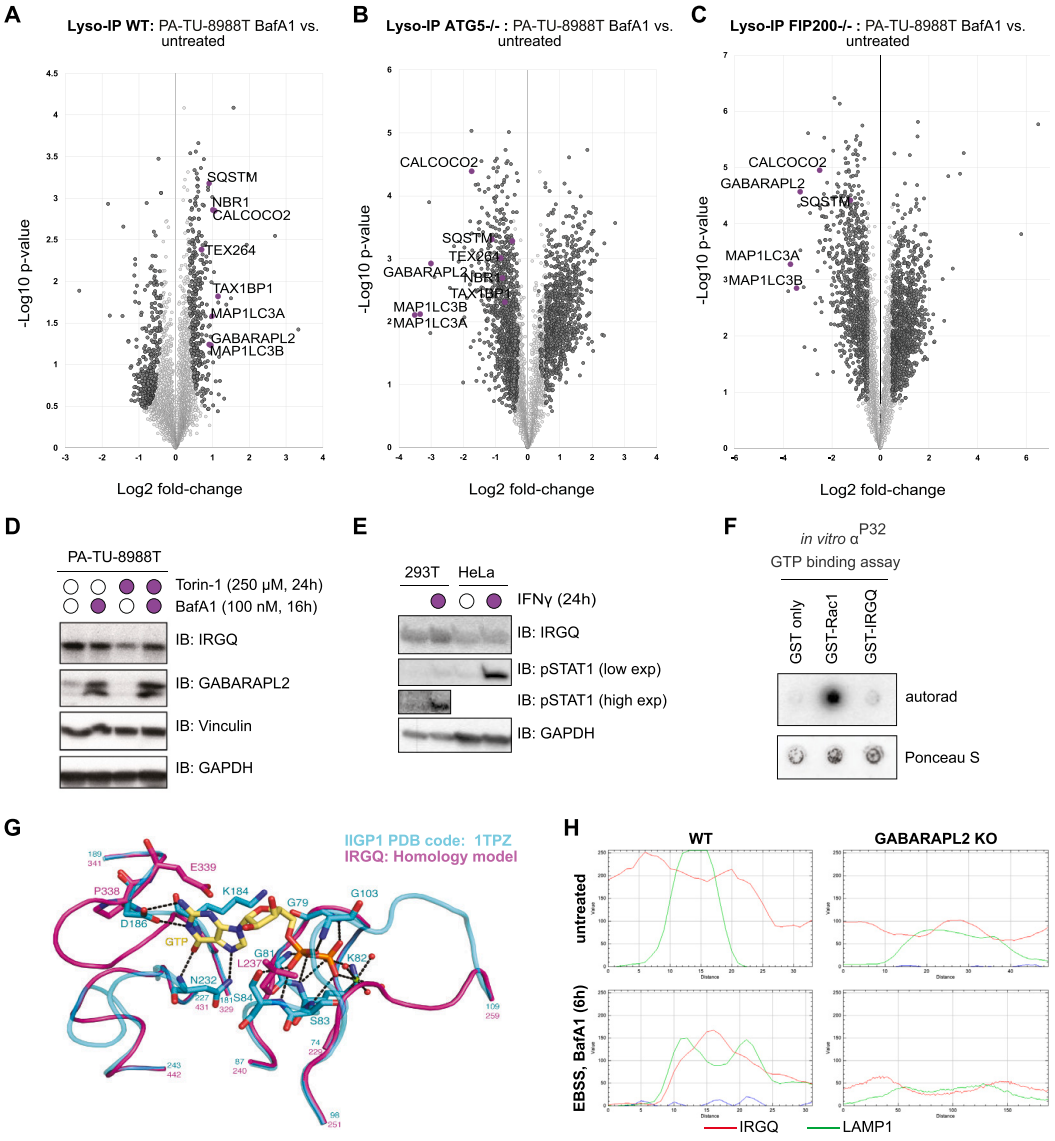

(legend on next page)

Figure S1. Protein abundances in isolated lysosomes and IRGQ characterization, related to Figure 1

(A–C) Volcano plots showing protein abundances in the lysosome after BafA1 treatment in (A) WT, (B) ATG5 $^{-/-}$, and (C) FIP200 $^{-/-}$ cells. The x axis represents the relative $\log_2$ fold change of protein abundance, and the y axis represents Welch's t test values calculated using Perseus. Dark gray proteins are indicated as statistically significant proteins using an FDR cutoff of 5%. Proteins in purple represent autophagy substrates.

(D) SDS-PAGE and western blot of PA-TU-8998T cells, treated with Torin-1 (24 h, 250 μM) and BafA1 (24 h, 100 nM). Protein lysates were analyzed by western blot with the indicated antibodies.

(E) SDS-PAGE and western blot of HEK293T and HeLa cell lysates that were treated with 10 ng/mL IFNγ for 24 h.

(F) Dot-blot and autoradiograph of GST proteins loaded with α^{P32}GTP.

(G) Superposition of interferon-inducible GTPase 1 in complex with GDP and the homology model of IRGQ highlights missing key residues for GDP binding in IRGQ.

(H) ImageJ profile plots of IF images (Figure 1E). IRGQ (red) only accumulates inside lysosomes (green) in WT cells treated with EBSS and BafA1.

(I) Quantification of IRGQ-positive lysosomes (IF images Figure 1E). Data are presented as the mean with error bars indicating the SD. Statistical significance of differences between experimental groups was assessed with Student's t test. Differences with $p < 0.05$ are annotated as *; $n = 3$.

(J and K) Immunofluorescence of endogenously mCherry-tagged IRGQ HeLa cells. Cells were left untreated or treated for 4 h in EBSS with BafA1 (200 nM). Fixed cells were probed with DAPI, phalloidin, and endogenous LC3B (J) and LAMP1 (K) antibodies. Scale bar: 10 μm.

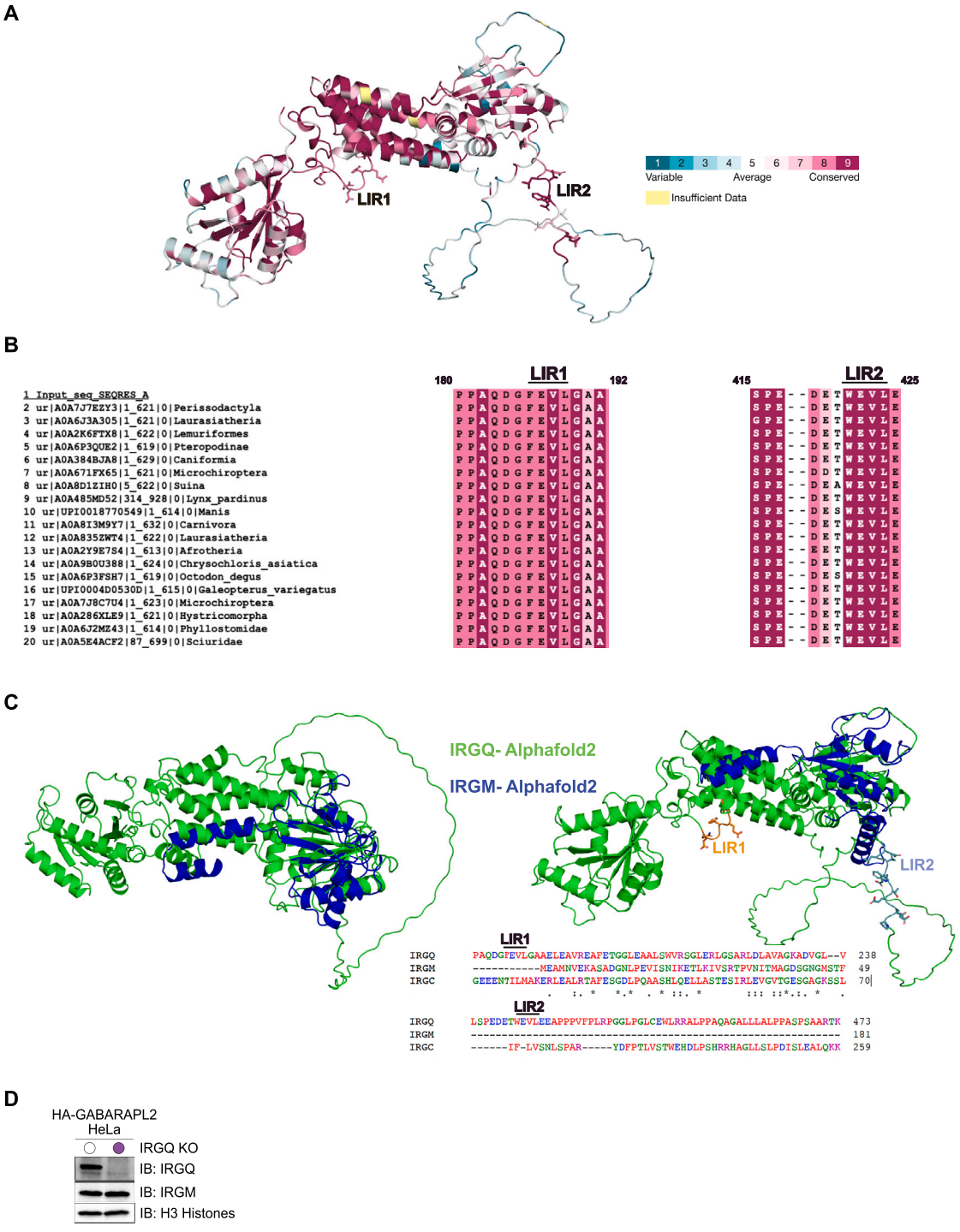

Figure S2. LIR conservation in IRGQ, related to Figure 2

(A) Residues conserved in IRGQ homologs mapped onto the AlphaFold model of human IRGQ (identifier: AF-Q8WZA9-F1), using ConSurf webserver[93] (https://consurf.tau.ac.il/consurf_index.php). The color key for variable to conserved residues is shown next to the model. Peptide stretches with stick representation show the LIR1 and LIR2 motifs present in IRGQ.

(B) Multiple sequence alignment of 49 IRGQ homologs showing the nature of conservation of LIR1 and LIR2 sequences derived from ConSurf webserver.

(C) Overlay of the AlphaFold models of IRGQ (AF-Q8WZA9-F1) and IRGM (AF-A1A4Y4-F1), two family members of IRG family in humans showing the lack of the LIR1 and LIR2 motif regions in IRGM. Sequence alignment of IRGQ, IRGM, and IRGC shows the presence of these LIR motifs in IRGQ.

(D) SDS-PAGE and western blot of HeLa WT and IRGQ KO cells.

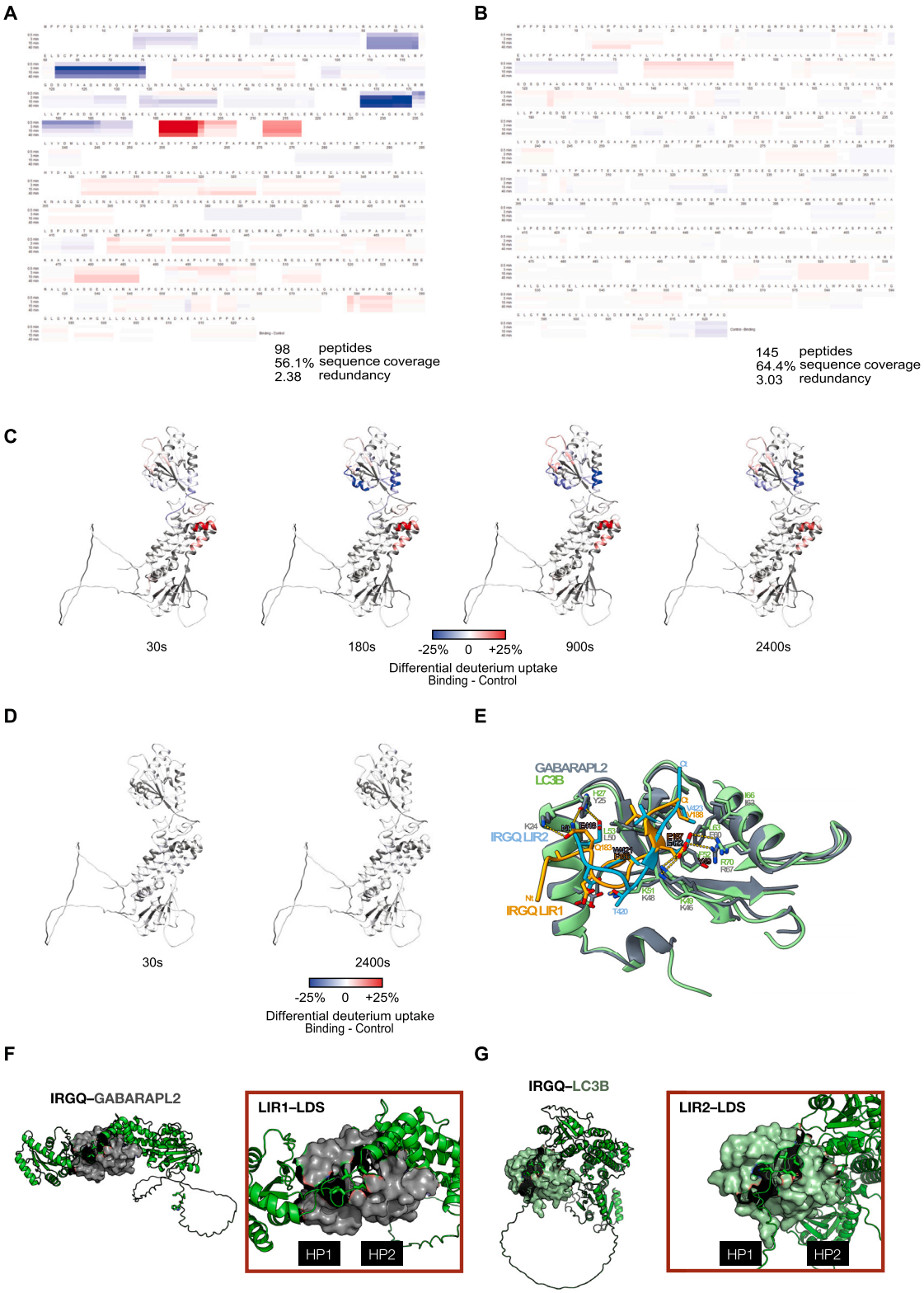

Figure S3. LIR-dependencies of IRGQ binding to LC3B and GABARAPL2, related to Figure 2

(A) Heatmap representation of differential deuterium uptake for IRGQ + GABARAPL2. Differential uptake of IRGQ + GABARAPL2 (binding)—IRGQ (control) is shown for all time points along the protein sequence. Generation of the heatmap preceded back-exchange correction and statistical evaluation.

(legend continued on next page)

(B) Same as (A) but showing differential deuterium uptake for IRGQ + LC3B.
(C) Differential deuterium uptake of IRGQ + GABARAPL2 (binding)—IRGQ (control) plotted on the IRGQ AlphaFold model prediction (identifier: AF-Q8WZA9-F1) for all time points. Amino acids that were not identified or excluded for the final evaluation are shown in dark gray. Color gradient ranges from blue (reduced differential uptake) to red (increased differential uptake).
(D) Same as (C) but showing differential deuterium uptake of IRGQ + LC3B for 30 and 2,400 s.
(E) The structure of LC3B (green) in complex with the IRGQ LIR2 peptide (416–425) (blue) overlaid with GABARAPL2 (gray) and the IRGQ LIR1 peptide (183–190) (orange). This binding mode derived from the second molecule of the asymmetric unit of the crystal structure suggests that LC3B-LIR2 interaction can adopt different conformations beyond the conserved HP1 and HP2 interactions.
(F and G) Top-ranked and most prominent binding mode of AlphaFold2 (F), IRGQ-GABARAPL2 and (G) IRGQ-LC3B complexes are shown. LIR sites (sticks) of IRGQ (green cartoon; top-ranked model) and LDS on hATG8 (surface view) are shown. Insets show the zoom-up of conserved of stabilizing LIR1-LDS and LIR2-LDS interactions of GABARAPL2 and LC3B, respectively.

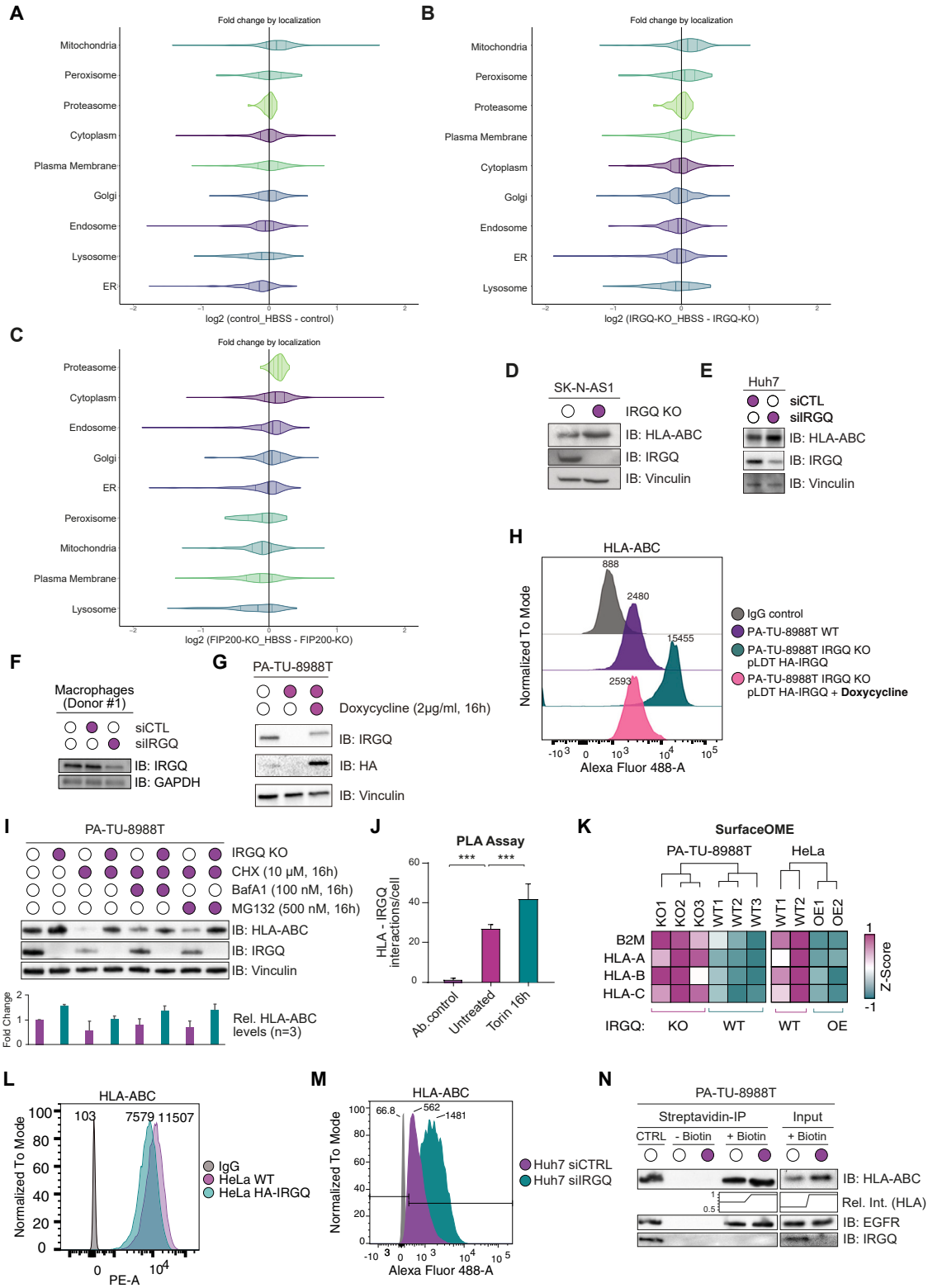

Figure S4. IRGQ modulates MHC class I protein levels, related to Figure 3

(A–C) Organelle classes of total proteome analysis of PA-TU-8988T (A) WT, (B) IRGQ KO, or (C) FIP200 KO cells under fed and starved conditions.
(D) SDS-PAGE and western blot of SK-N-AS1 WT and IRGQ KO cells.

(legend continued on next page)

(E) SDS-PAGE and western blot of Huh7 cells treated with siRNA against control or IRGQ.
(F) SDS-PAGE and western blot of primary human macrophages transfected with control or IRGQ siRNA (Figures 3D and 3E).
(G) SDS-PAGE and western blot of doxycycline-inducible HA-IRGQ (pLDT vector) PA-TU-8988T IRGQ KO cells in the presence and absence of doxycycline.
(H) FACS analysis of surface HLA-ABC from PA-TU-8988T cells that are either WT or KO of IRGQ with a reintroduced doxycycline-inducible HA-IRGQ (± doxycycline treatment).
(I) SDS-PAGE and western blot of lysates from PA-TU-8988T IRGQ WT and KO cells treated with cycloheximide (CHX, 10 μM, 16 h), BafA1 (100 nM, 16 h), and/or MG132 (500 nM, 16 h). ImageJ quantification of HLA intensity normalized to vinculin. $n = 3$.
(J) Duolink PLA assay using IRGQ and HLA antibodies in untreated or Torin-1 (16 h) treated cells. Data were analyzed by the Yokogawa CQ1 and are presented as the mean with error bars indicating the SD. Statistical significance of differences between experimental groups was assessed with Student's t test. Differences with $p < 0.001$ are annotated as ***; $n = 3$.
(K) SurfaceOME of IRGQ WT and KO PA-TU-8988T cells, as well as HeLa WT and HA-IRGQ, overexpressed cells. Biotinylated surface proteins were immunoprecipitated by streptavidin and proteins analyzed with MaxQuant and Perseus.
(L) FACS analysis of surface HLA-ABC from HeLa WT and HA-IRGQ overexpressed cells.
(M) FACS analysis of surface HLA-ABC from Huh-7 cells treated with control or siRNA targeting IRGQ.
(N) SDS-PAGE and western blot of streptavidin IPs from biotinylated cell surface membrane proteins and inputs from IRGQ WT and KO PA-TU-8988T cells. Quantification of HLA intensity from ImageJ.

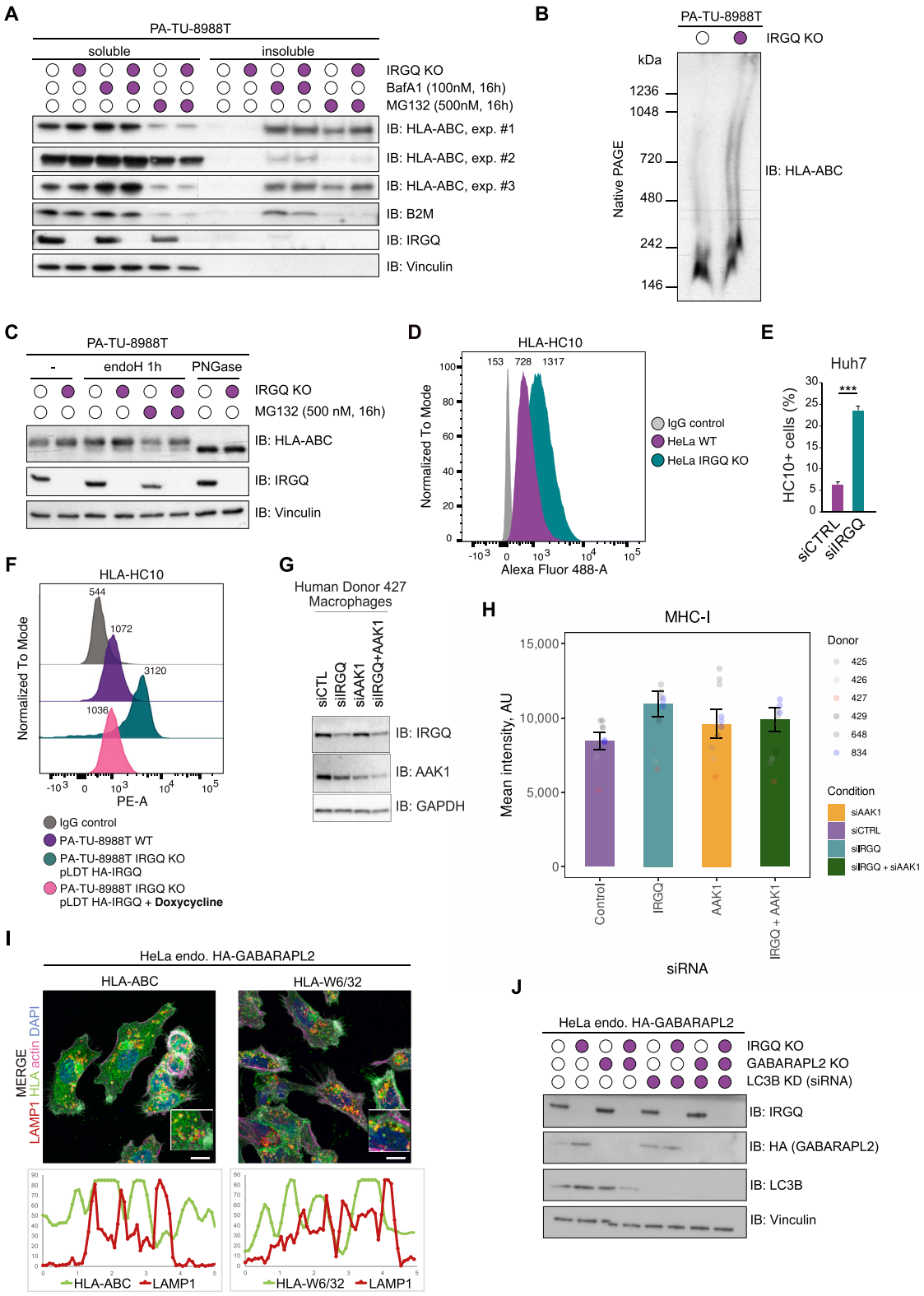

Figure S5. IRGQ targets non-conformational HLA molecules, related to Figure 5

(A) SDS-PAGE and western blot of lysates from PA-TU-8988T IRGQ WT and KO cells treated with BafA1 (100 nM, 16 h) or MG132 (500 nM, 16 h) and separated into soluble and insoluble factions by centrifugation. (Quantification Figure 5A, *n* = 3).

(legend continued on next page)

(B) Native-PAGE and western blot of lysates from PA-TU-8988T IRGQ WT and KO cells.
(C) SDS-PAGE and western blot of lysates from PA-TU-8988T IRGQ WT and KO cells treated with MG132 (500 nM, 16 h). Lysates were treated with endoH or PNGase for 1h. (Quantification Figure 5B, $n = 7$).
(D) FACS analysis of HeLa WT and IRGQ KO cells using IgG control and HLA-HC10.
(E) Percentage of Huh7 single cells positive for HLA-HC10 staining after FACS analysis for 3 independent replicates. Statistical significance of differences between experimental groups was assessed with Student's t test. Differences with $p < 0.001$ are annotated as ***; $n = 3$.
(F) FACS analysis of surface HLA-HC10 from PA-TU-8988T cells that are either WT or KO of IRGQ with a reintroduced doxycycline-inducible HA-IRGQ (± doxycycline treatment).
(G) FACS analysis of HLA-ABC antibody in primary human macrophages from six healthy donors transfected with control, IRGQ or/and AAK1 siRNA. Individual donors are color coded.
(H) SDS-PAGE and western blot of primary human macrophages treated with non-targeting control, IRGQ or AAK1 siRNAs from experiment (G).
(I) HeLa WT and IRGQ KO cells were treated with EBSS (4 h) together with BafA1, and fixed cells were stained with LAMP1, phalloidin (actin cytoskeleton marker), DAPI (nucleus marker), and either HLA-ABC (total MHC class I) or HLA-W6/32 (conformational MHC class I). Verification of HLA presence in lysosomes was done with ImageJ. Representative fluorescence images were taken in z stacks with a Leica confocal microscope SP8. (Quantification Figure 5F, $n = 3$.) Scale bar: 10 μm.
(J) SDS-PAGE and western blot of lysates from endo HA-GABARAPL2 WT, IRGQ KO, and/or GABARAPL2 KO cells treated with control or LC3B siRNA. Confirmation of KO/KD for quantification of Figure 5G.

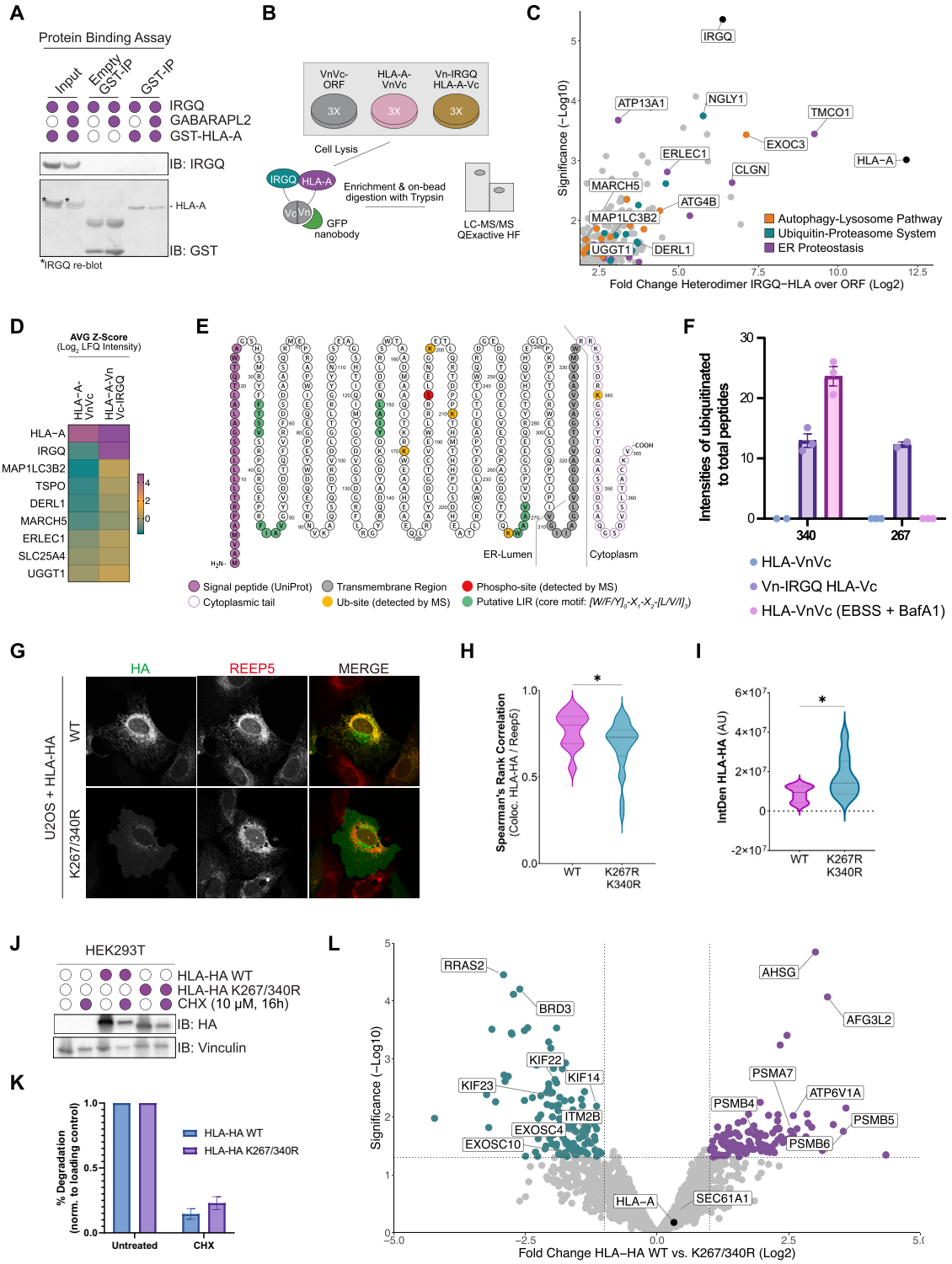

Figure S6. The role of HLA ubiquitylation for IRGQ recognition, related to Figure 5

(A) SDS-PAGE and western blot of an *in vitro* GST pull-down using purified GST-HLA together with purified IRGQ and/or GABARAPL2.

(B) Scheme of mass spectrometry experiment performed in (C), (D), and (F).

(C) HEK293T cells were transfected with VnVc-ORF, HLA-A-VnVc, or Vn-IRGQ/HLA-A-Vc lysates used for GFP IPs and processed for MS. Data were analyzed with MaxQuant and Perseus; $n = 3$. The volcano plot represents the Student's t test difference and −log Student's t test p value from Vn-IRGQ/HLA-A-Vc over control IPs. The bait IRGQ/HLA is marked in black, and the most significant interaction partners are color coded according to their category.

(legend continued on next page)

(D) Heatmap of interaction partners of HLA-A-VnVc or Vn-IRGQ/HLA-A-Vc from (B).
(E) Schematic representation of the amino acid sequence of HLA-A protein with marked PTMs identified in (B)–(D)
(F) Intensity of ubiquitylated peptides normalized to total peptides of HLA-A-VnVc, Vn-IRGQ/HLA-A-Vc, or HLA-A-VnVc (treated with EBSS and BafA1, 4 h) on residues K267 and K340, identified by mass spectrometry (B).
(G) Immunofluorescence of U2OS cells overexpressing WT HLA-HA or K267/340R mutant HLA-HA. Fixed cells were probed with endogenous REEP5 and HA antibodies.
(H) Spearman's rank correlation of co-localization between HLA WT or K267/340R mutant with REEP5. Statistical significance of differences between experimental groups was assessed with Student's t test. Differences with $p < 0.05$ are annotated as *; $n = 25$.
(I) Relative fluorescence intensity of HLA WT or K267/340R mutant. Statistical significance of differences between experimental groups was assessed with Student's t test. Differences with $p < 0.05$ are annotated as *; $n = 15$.
(J) SDS-PAGE and western blot of lysates from HEK293T cells overexpressing WT HLA-HA or K267/340R mutant HLA-HA treated with CHX (10 μM, 16 h).
(K) ImageJ quantification of HLA intensity normalized to vinculin (from J). $n = 3$.
(L) HEK293T cells were transfected with HLA-A-HA WT or HLA-A-HA K267/340R lysates used for HA IPs and processed for MS. Data were analyzed with Fragpipe; $n = 3$. The volcano plot represents the Student's t test difference and −log Student's t test p value from HLA-A-HA WT over HLA-A-HA K267/340R IPs. The bait HLA is marked in black, and proteins that preferentially bind WT HLA are marked in purple in comparison with proteins interacting with HLA-A-HA K267/340R in green.

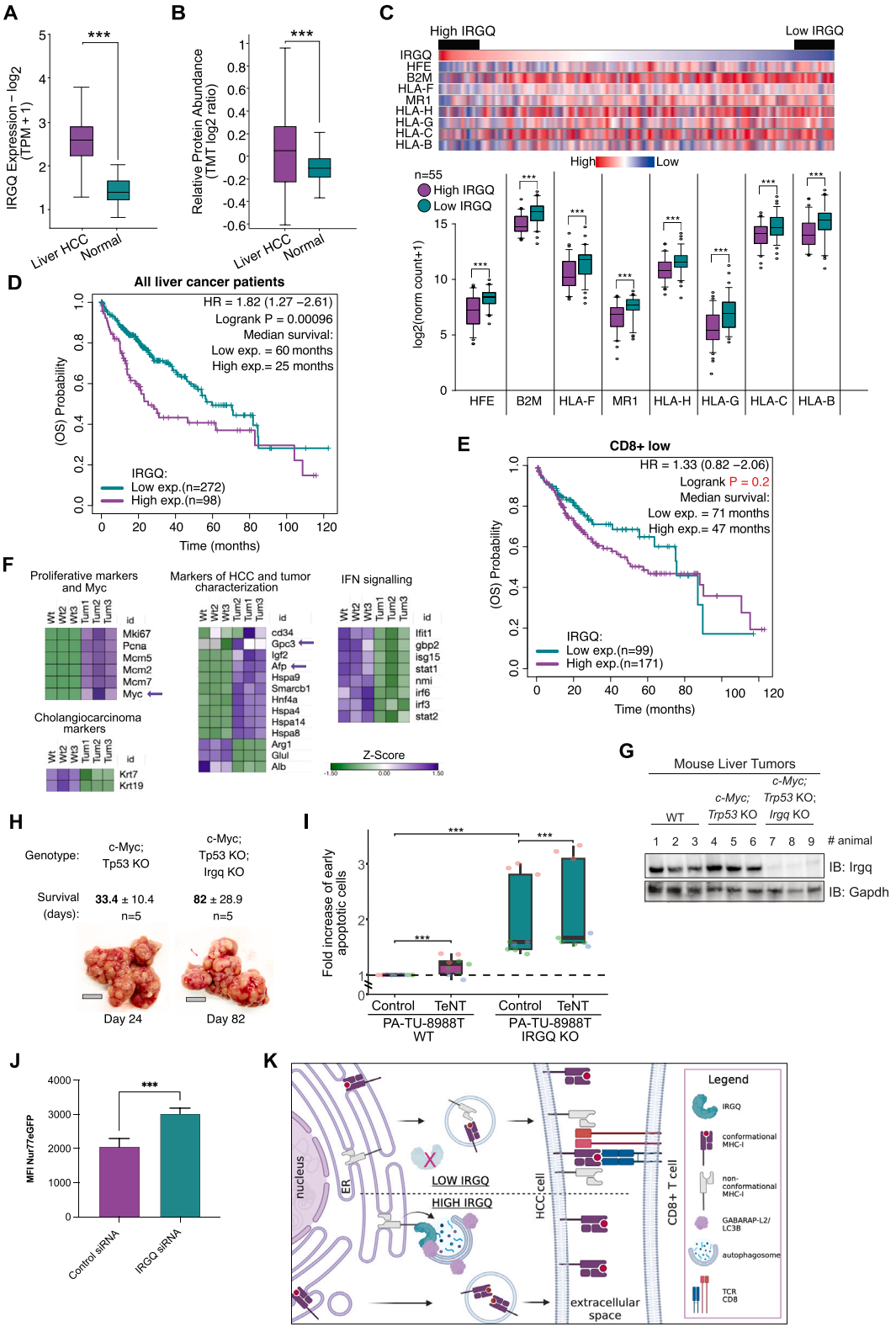

Figure S7. Reduced IRGQ levels are beneficial for HCC patients, related to Figure 6

(A) IRGQ mRNA expression of human liver HCC and adjacent normal tissue samples (data obtained from NIH Center for Cancer Genomics, the Cancer Genome Atlas program [TCGA]). *n* = 36 samples of liver HCC patients; 50 samples of normal unperturbed liver tissue

(legend continued on next page)

(B) Same as in (A) but for IRGQ protein expression.
(C) Clustering of HCC patient data with high or low IRGQ mRNA expression and correlation with mRNA levels of MHC class I-related genes (data obtained from NIH Center for Cancer Genomics, the Cancer Genome Atlas program [TCGA]).
(D) Kaplan-Meier survival plot of liver cancer patients with high or low IRGQ mRNA expression levels (data obtained from NIH Center for Cancer Genomics, the Cancer Genome Atlas program [TCGA]).
(E) Kaplan-Meier survival plot of liver cancer patients with high or low IRGQ mRNA expression levels in tumors that are depleted of CD8+ T cells (data obtained from NIH Center for Cancer Genomics, the Cancer Genome Atlas program [TCGA]).
(F) Heatmap of total proteome analysis of healthy (WT) and HCC (*c-Myc*; *Trp53*Δ) mouse liver tissue.
(G) SDS-PAGE and western blot of lysates from *c-Myc; Trp53⊿* and *c-Myc; Trp53⊿; Irgq⊿* mice livers.
(H) Isolated livers from c-Myc; Trp53Δ and c-Myc; Trp53Δ; IrgqΔ mice at 24 and 82 days post plasmid delivery, respectively.
(I) FACS analysis of early apoptotic PA-TU-8988T WT and IRGQ KO cells upon co-culture with primary human T CD4+ and CD8+ cells post control or tetanus toxoid stimulation. Individual donors are color coded. $n = 3$.
(J) Quantification of Nur77eGFP expression in CD8+ T cells presented as mean fluorescence intensity as measured by FACS. $n = 3$.
(K) Model of tumor immune evasion through IRGQ-directed autophagy.
Data are presented as the box-and-whisker plot. Statistical significance of differences between experimental groups was assessed with Student's t test. Differences with $p < 0.001$ are annotated as ***.